D I S S E R T A T I O N

Extracellular vesicles released from apoptotic cells and their impact on different tissue-derived macrophages

submitted by

Stephanie Leyk

Hamburg, May 2024

for the attainment of the degree *Doctor rerum naturalium*

University of Hamburg

Department of Biology

Faculty of Mathematics, Informatics and Natural Sciences

The present work was performed under the guidance of Lidia Bosurgi, Ph.D. at the Bernhard Nocht Institute for Tropical Medicine (BNITM) and University Medical Center Hamburg-Eppendorf (UKE).

1st reviewer: Prof. Dr. Iris Bruchhaus

2nd reviewer: Prof. Dr. Julia Kehr

Date of the oral defence: 30.08.2024

Eidesstattliche Versicherung - Declaration on oath

Hiermit erkläre ich an Eides statt, dass ich die vorliegende Dissertationsschrift selbst verfasst und keine anderen als die angegebenen Quellen und Hilfsmittel benutzt habe.

I hereby declare, on oath, that I have written the present dissertation by my own and have not used other than the acknowledged resources and aids.

Hamburg, 17.05.2024



Table of contents

List of Abbreviations V
List of Figures IX
List of Tables XI
Abstract XII
Zusammenfassung XIII
1 Introduction 1
1.1 Extracellular vesicles (EVs) 1
1.1.1 Biogenesis 1
1.1.2 Cargo selection 2
1.1.3 Targeting of recipient cells 3
1.2 Apoptosis 5
1.2.1 Extracellular vesicles released during apoptosis 5
1.3 A brief introduction to the immune system 7
1.3.1 Macrophages (Mϕs) 8
1.3.2 Mϕ polarisation 9
1.3.3 Efferocytosis 11
1.3.4 Interaction of Mϕs and EVs 12
1.4 Schistosomiasis 14
1.4.1 *S. mansoni* life cycle 15
1.4.2 The immune response to *S. mansoni* infection 15
1.4.3 EVs in schistosomiasis 17
1.5 Aim 18
1 Material and methods 19
1.1 Materials 19
1.1.1 Cell line 19
1.1.2 Mouse strains 19
1.1.3 Parasites 19
1.1.4 Biological and chemical reagents 19
1.1.5 Buffers, solution, and media 20
1.1.6 Dyes and antibodies 21
1.1.7 Primers 22
1.1.8 Commercial kits 23
1.1.9 Consumable materials 23
1.1.10 Laboratory equipment 24
1.1.11 Software 25

1.2 Methods 26
1.2.1 Cell culture 26
1.2.2 Cell count 26
1.2.3 Bone marrow-derived Mϕs 26
1.2.4 Isolation of thymocytes and induction of apoptosis 27
1.2.5 Determination of apoptosis rates 27
1.2.6 Isolation of EVs from thymocytes 27
1.2.7 NTA 28
1.2.8 Protein concentration 28
1.2.9 TEM 28
1.2.10 CFSE-labelling of EVs 28
1.2.11 EV uptake assay *in vitro* 29
1.2.12 Phagocytosis assay 29
1.2.13 Fibroblast migration assay 29
1.2.14 Flow cytometry 30
1.2.14.1 Staining of EVs for flow cytometry 30
1.2.14.2 Staining of cells for flow cytometry 31
1.2.15 MACSPlex for EV surface epitope detection 31
1.2.16 RNA Isolation 32
1.2.16.1 RNA Isolation from EVs 32
1.2.16.2 RNA Isolation from cells using Trizol 32
1.2.16.3 RNA Isolation from cells using RNeasy Mini Kit 32
1.2.17 cDNA Synthesis 33
1.2.18 Quantitative Real-Time PCR 33
1.2.19 Bulk-RNA Sequencing 34
1.2.20 LEGENDplex™ 35
1.2.21 Nitric oxide assay 35
1.2.22 Mice 35
1.2.23 Organ harvesting 35
1.2.24 Thioglycolate-induced peritonitis 36
1.2.25 *S. mansoni* infection 36
1.2.26 EV transfer in *S-mansoni*-infected mice 36
1.2.27 ALT levels 36
1.2.28 Egg count 37
1.2.29 Histology 37
1.2.30 Isolation of cells from liver 37

1.2.31 Isolation of EVs from liver 37
1.2.32 Statistics 38
2 Results 39
2.1 Isolation of EVs from live and apoptotic thymocytes 39
2.2 Characterisation of EVs from live and apoptotic thymocytes 40
2.2.1 Size and concentration of liveT- and aT-EVs 40
2.2.2 Detection of apoptosis marker proteins by flow cytometry 41
2.2.2.1 Surface phosphatidylserine 41
2.2.2.2 Intravesicular cleaved caspase-3 42
2.2.3 Detection of surface epitopes via MACSPlex and FACS 43
2.3 Characterisation of Mϕs taking up liveT- or aT-EVs 44
2.3.1 Mϕs take up liveT and aT-EVs *in vitro* 45
2.3.2 Characterisation of Mϕs 24 h upon uptake of liveT- or aT-EVs 48
2.3.3 Peritoneal Mϕs take up liveT and aT-EVs *in vivo* 49
2.3.4 Characterisation of pMϕs 24 h after uptake of liveT and aT-EVs *in vivo* 51
2.3.5 Uptake of liveT or aT-EVs does not impact Mϕs phagocytic activity 52
2.3.5.1 Phagocytic capacity of liveT- and aT-EV-treated BMDMs 52
2.3.5.2 Phagocytic capacity of aT-EV-treated large pMϕs 54
2.3.6 BMDMs phenotype is distinct after uptake of liveT- or aT-EVs 56
2.3.7 LiveT-EVs target nitric oxide pathway in Mϕs 57
2.3.8 LiveT- and aT-EV treatment of Mϕs does not influence fibroblast migration 58
2.4 Transfer of liveT or aT-EVs in *S. mansoni*-infected mice modulates disease pathology 60
2.5 Liver-EVs isolated from *S. mansoni*-infected mice 63
2.5.1 Isolation and characterisation of EVs isolated from the livers of *S. mansoni*-infected or naïve mice 63
2.5.2 Characterisation of the cargo composition of naïve and infected EVs 65
2.5.3 BMDMs take up Liver-EVs from naïve mice and *S. mansoni*-infected mice 66
2.5.4 BMDMs upregulate iNOS expression upon uptake of liver-EVs from *S. mansoni*-infected mice 67
3 Discussion 68
3.1 Characterisation of differences between EVs released from live or apoptotic thymocytes 68
3.1.1 Cleaved caspase-3 as a cargo of aT-EVs and its possible functions 68
3.1.2 Surface marker composition of liveT- and aT-EVs 70
3.1.2.1 Technical limitations of surface marker detection on EVs 71
3.2 Modulatory effects of liveT- and aT-EVs on Mϕs 72
3.2.1 Mϕs phagocyte EVs from live and apoptotic thymocytes 72
3.2.2 Impact of EV uptake on Mϕs phagocytic capacity 73

3.2.3 Transcriptomic and functional alterations in Mϕs treated with liveT- or aT-EVs 74
3.2.3.1 Modulation of the nitric oxide pathway in Mϕs 75
3.2.3.2 The influence of EVs on Mϕ cytokine signalling and tissue repair functions 76
3.2.3.3 *SerpinB2* expression and its consequences in schistosomiasis 77
3.3 Impact of liveT- and aT-EV transfer on schistosomiasis pathology 78
3.4 Characterisation of liver-EVs isolated from naïve or *S. mansoni*-infected mice 82
4 Future perspective 84
References XII
List of Publications XXIV
Acknowledgements XXV

List of Abbreviations

%	Percent
°C	Degree Celsius
α-SMA	alpha-smooth muscle actin
µg	Microgram
µL	Microlitre
µm	Micrometre
AF	Alexa Fluor
Ahr	aryl hydrocarbon receptor
ALT	Alanine aminotransaminase
APC	Allophycocyanine
APC-Cy7	Allophycocyanine + cyanine dye 7
APCs	Antigen-presenting cells
ApoEVs	EVs released from apoptotic cells
ARG1	Arginase 1
aT	Apoptotic thymocyte
ATP	Adenosine triphosphate
BCL-2	B-cell lymphoma 2
BCR	B cell receptor
BMDMs	Bone marrow-derived macrophages
BUV	Brilliant™ Ultraviolet
BV	Brilliant™ Violet
Ca^{2+}	Calcium
Car4	Carbonic anhydrase IV
CCL	C-C motif chemokine ligand
CCR2	C-C motif chemokine receptor 2
CD	Cluster of differentiation
CLEC4F	C-Type Lectin Domain Family 4 Member F
CFDA-SE	Carboxyfluorescein diacetate succinimidyl ester
CFSE	Carboxyfluorescein succinimidyl ester
CO_2	Carbon dioxide
Col1	Collagenase 1
CXCL	C-X-C motif chemokine
DAMPs	Damage-associated molecular patterns
DCs	Dendritic cells
DNA	Deoxyribonucleic acid
DPBS	Dulbecco's phosphate-buffered saline
ECM	Extracellular matrix
ELISA	Enzyme-linked Immunosorbent Assay
ESCRT	Endosomal sorting complex required for transport
EVs	Extracellular vesicles
FACS	Fluorescence-activated cell sorting
FasL	Fas ligand

FasR	Fas receptor
FCS	Fetal calf serum
FITC	Fluorescein isothiocyanate
FMR1	Fragile X mental-retardation protein
Fn1	Fibronectin 1
FOXO3	Forkhead box O3
FSC	Forward scatter
GAPDH	Glyceraldehyde 3-phosphate dehydrogenase
Gas6	growth arrest-specific 6
Gata3	GATA-binding protein 3
GTP	Guanosine triphosphate
h	Hours
Hrs	Hepatocyte growth factor–regulated tyrosine kinase substrate
HSCs	Hepatic stellate cells
ICAM	Intercellular adhesion molecules
iNOS	Inducible nitric oxide synthase
IFN-Y	Interferon-gamma
IL	Interleukin
ILVs	Intraluminal vesicles
i.p.	Intra peritoneal
i.v.	Intra venous
ISEV	International Society for Extracellular Vesicles
k	000
KOH	Potassium hydroxide
liveT	Alive thymocyte
FC	Fold change
LPS	Lipopolysaccharides
Ly6C	Lymphocyte antigen 6 complex locus C
Mϕ	Macrophage
MCP-1	Monocyte chemotactic protein-1
MERTK	Mer tyrosine kinase
MFG-E8	Milk fat globule-epidermal growth factor 8
MFI	Mean fluorescent intensity
MHC	Major histocompatibility complex
min	Minutes
miRNA	Micro RNA
mL	Millilitres
MMPs	Matrix metalloproteinases
mRNA	Messenger RNA
MVBs	Multivesicular bodies
MSC	Mesenchymal stroma cells
N_2	Nitrogen
NETs	Neutrophil extracellular traps
NK cells	Natural killer cells
nm	Nanometres

Nmes1	Normal Mucosa of Esophagus-Specific Gene 1
NO	Nitric oxide
Nos2	Nitric oxide synthase 2
nt	Nucleotides
NTA	Nanoparticle tracking analysis
O_2	Oxygen
PAMPs	Pathogen-associated molecular patterns
PBMCs	Peripheral blood mononuclear cells
PBS	Phosphate-buffered saline
PDGF	Platelet-derived growth factor
PE	R-Phycoerythrin
PerCP	Peridinin Chlorophyll Protein Complex
PFA	Paraformaldehyde
pg	Picogram
PI	Propidium Iodide
p.i.	Post infection
pMϕ	Peritoneal macrophages
PROS1	Protein S 1
PRRs	Pathogen recognition receptors
RBCs	Red blood cells
RBP	RNA binding protein
rcf	Relative Centrifugal Force or G-force
RELMα	Resistin-like molecule α
RNA	Ribonucleic acid
ROCK1	Rho-associated kinase 1
RPMI	Roswell Park Memorial Institute
RT	Room temperature
RTK	Receptor tyrosine kinase
RT-qPCR	Quantitative real-time polymerase chain reaction
s.c.	Subcutaneous
S. mansoni	*Schistosoma mansoni*
SEA	Soluble egg antigen
sec	Seconds
SEM	Standard error of the mean
Serpin	Serine protease inhibitors
Sm-TSP-2	*S. mansoni* tetraspanin
Sm14	*S. mansoni* fatty acid binding protein
SSC	Sideward scatter
SOCS	Suppressor of cytokine signalling
SPF	Specific pathogen-free
STAT	Signal transducer and activator of transcription 1
TCR	T cell receptor
TEM	Transmission electron microscopy
TGF	Transforming growth factor
Th1	T helper 1

Th2	T helper 2
TIM4	T cell membrane protein 4
TIMPs	Tissue inhibitors of metalloproteinases
TLR	Toll-like receptor
TNF	Tumour necrosis factor
TNFR1	Tumour necrosis factor receptor 1
UTP	Uridine triphosphate
VEGF	Vascular endothelial growth factor
WHO	World Health Organisation
w/o	Without
YM1	Chitinase-like protein 3

List of Figures

Figure 1: Schematic overview of the biogenesis and uptake of extracellular vesicles. 4
Figure 2: Schematic overview of factors determining Mϕ polarisation. 11
Figure 3: Schematic overview of the immune response during schistosomiasis. 17
Figure 4: Isolation of EVs from live and apoptotic thymocytes. 39
Figure 5: Morphology, size, and concentration of liveT- and aT-EVs. 40
Figure 6: Detection of surface phosphatidylserine on liveT- and aT-EVs by flow cytometry. 41
Figure 7: Detection of intravesicular cleaved caspase-3 by flow cytometry. 42
Figure 8: Detection of surface epitopes on EVs. 43
Figure 9: CFDA-SE labelling of EVs. 45
Figure 10: Flow cytometric analysis of the uptake of liveT- or aT-EVs by Mϕs. 47
Figure 11: Characterisation of Mϕs 24 h upon uptake of liveT- or aT-EVs by flow cytometry. 48
Figure 12: The uptake of liveT-EVs and aT-EVs by pMϕs in a model of thioglycolate-induced peritonitis. 50
Figure 13: Characterisation of pMϕs in a model of thioglycolate-induced peritonitis mice 24 h upon uptake of liveT- or aT-EVs by flow cytometry. 51
Figure 14: Flow cytometric analysis of the phagocytic capacity of liveT- and aT-EV-treated BMDMs. 53
Figure 15: Flow cytometric analysis of the phagocytic capacity of aT-EV-treated large pMϕs in a model of thioglycolate-induced peritonitis. 55
Figure 16: Uptake of live-T- or aT-EVs affect BMDMs transcriptomic signature. 56
Figure 17: Expression levels of selected genes from transcriptomic analysis of liveT- or aT-EVs-treated BMDMs. 57
Figure 18: Detection of iNOS protein expression and NO production by Mϕs treated with liveT- or aT-EVs for 24 h. 58
Figure 19: Supernatants from Mϕs incubated with liveT- or aT-EVs have no influence on fibroblast migration. 59
Figure 20: Transfer of liveT- or aT-EVs in *S. mansoni*-infected mice does not influence immune cell composition in the liver. 60
Figure 21: Phenotypic analysis of hepatic Mϕs from *S. mansoni*-infected mice after transfer of liveT- or aT-EVs. 61
Figure 22: Transfer of liveT- or aT-EVs in *S. mansoni*-infected mice does influence disease pathology. 62
Figure 23: Contribution of liveT- or aT-EVs to liver fibrosis in *S. mansoni*-infected mice. 62
Figure 24: Isolation of EVs isolated from the livers of *S. mansoni*-infected or naïve mice. 63
Figure 25: Morphology, size, and concentration of EVs isolated from the livers of *S. mansoni*-infected or naïve mice. 64

Figure 26: Characterisation of surface epitopes of EVs isolated from the livers of *S. mansoni*-infected or naïve mice. 65

Figure 27: Uptake of CFSE-labelled EVs from the livers of *S. mansoni*-infected or naïve mice by BMDMs analysed by flow cytometry. 66

Figure 28: EVs from *S. mansoni*-infected livers induce iNOS expression in Mϕs..... 67

List of Tables

Table 1: List of eukaryotic cell lines used. 19
Table 2: List of mouse strains used. 19
Table 3: List of biological and chemical reagents used for experiments. 19
Table 4: Recipes for buffers, solutions and media used during experiments. 20
Table 5: List of used antibodies and dyes. 21
Table 6: List of Primer sequences. 22
Table 7: List of used commercial kits. 23
Table 8: List of used consumable materials. 23
Table 9: List of used equipment and devices. 24
Table 10: List of software, programs and databases used for data acquisition and analyses, writing, literature research, and citation. 25
Table 11: List of NTA settings. 28
Table 12: cDNA synthesis Reaction-Mix. 33
Table 13: cDNA synthesis thermocycler settings. 33
Table 14: qPCR Reaction-Mix. 34
Table 15: Rotor-Gene settings. 34

Abstract

One of the universal functions of macrophages (Mϕs) is to sustain tissue homeostasis through the clearance of apoptotic cells. Apoptotic cells have been described to not only release apoptotic bodies but also increased amounts of other types of extracellular vesicles (EVs) packed with their cellular cargo. Via the delivery of bioactive molecules, the release of EVs serves as a potent tool for the cells of origin to facilitate intercellular communication, hence influencing the behaviour and function of the target cell. The aim of this study is to investigate differences between EVs released by live (liveT-EVs) or apoptotic (aT-EVs) thymocytes regarding their morphology and cargo composition and, in turn, their effects on Mϕs behaviour. Flow cytometry analysis revealed that liveT- and aT-EVs differ in the protein cargo composition, as aT-EVs display higher amounts of the surface epitopes CD4 and CD8 and contain more of the intravesicular protein cleaved caspase-3. Transcriptomic analysis of Mϕs suggests that the uptake of aT-EVs targets the nitric oxide pathway in Mϕs. This has been confirmed on mRNA and protein levels via RT-qPCR and flow cytometry, as aT-EV-treated Mϕs show higher expression of iNOS compared to liveT-EV-treated Mϕs. Both, liveT- and aT-EVs, were taken up by Mϕs *in vitro* and *in vivo*, preferentially by phagocytically active Mϕs. Yet, their uptake did not affect the Mϕs ability to engulf apoptotic cells, nor did it alter their tissue-remodelling function, as analysed via a fibroblast wound healing assay. To further investigate their function, liveT- and aT-EVs were transferred to *S. mansoni*-infected mice and analysed for their impact on the disease pathology. At the time point of analysis, the administration of EVs had no major effect on immune cell recruitment to the liver and on parasitic egg burden in the liver. However, ALT levels in the serum, an indicator of liver damage, were significantly lower in mice that received aT-EVs compared to untreated controls. Further experiments are required to determine if the transfer of aT-EVs might impact the progression of liver fibrosis at later time points of the disease. Additionally, EVs were isolated from the livers of *S. mansoni*-infected mice and characterised for their cargo composition and for their capacity to regulate the nitric oxide pathway in Mϕs in comparison to liver-EVs from naïve mice.

Altogether, the presented results demonstrate that aT-EVs have a minor effect on the phenotype, polarisation, and functionality of Mϕs compared to liveT-EVs. Nevertheless, aT-EVs possess distinct characteristics from liveT-EVs, can target important cell signalling pathways, and might influence the disease progression of schistosomiasis. EVs released in the livers of *S. mansoni*-infected mice, similarly to aT-EVs, target the nitric oxide pathway in Mϕs. Further investigations on the cargo composition and target cell interaction are required to fully elucidate the therapeutic potential of EVs derived from apoptotic as well as live cells.

Zusammenfassung

Eine der universellen Funktionen von Makrophagen (Mϕs) ist die Aufrechterhaltung der Homöostase in Geweben durch die Aufnahme apoptotischer Zellen. Es ist bereits bekannt, dass apoptotische Zellen nicht nur Apoptosekörper freisetzen, sondern auch größere Mengen anderer Arten von extrazellulären Vesikeln (EVs), die zelluläre, bioaktive Fracht enthalten. Die Freisetzung von EVs dient den Ursprungszellen als wirksames Instrument zur Erleichterung der interzellulären Kommunikation, da EVs bioaktive Moleküle enthalten, welche somit nach Aufnahme das Verhalten und die Funktion der Zielzelle beeinflussen können. Ziel dieser Studie ist es, die Unterschiede zwischen EVs, die von lebenden (liveT-EVs) oder apoptotischen (aT-EVs) Thymozyten freigesetzt werden, in Bezug auf ihre Morphologie und die Zusammensetzung der Fracht sowie ihre Auswirkungen auf das Verhalten von Mϕs zu untersuchen. Durchflusszytometrische Analysen ergaben, dass sich LiveT- und aT-EVs in der Proteinzusammensetzung unterscheiden, da aT-EVs höhere Mengen der Oberflächenepitope CD4 und CD8 aufweisen und mehr des intravesikulären Proteins gespaltene Caspase-3 enthalten. Transkriptom-Analysen von Mϕs deuten darauf hin, dass die Aufnahme von aT-EVs auf den Stickoxid-Stoffwechselweg in Mϕs abzielt. Dies wurde auf mRNA- und Proteinebene mittels RT-qPCR und Durchflusszytometrie bestätigt, da aT-EV-behandelte Mϕs, im Vergleich zu liveT-EV-behandelten Mϕs, eine höhere Expression von iNOS aufweisen. Sowohl EVs von apoptotischen als auch von lebenden Thymozyten wurden *in vitro* und *in vivo* von Mϕs aufgenommen, bevorzugt von phagozytisch aktiven Mϕs. Ihre Aufnahme beeinträchtigte jedoch weder die Fähigkeit der Mϕs, apoptotische Zellen aufzunehmen, noch ihre Funktion Gewebe zu modellieren, wie mit Hilfe eines Fibroblasten-Wundheilungs-Experiments analysiert wurde. Zur weiteren Untersuchung ihrer Funktion wurden liveT- und aT-EVs in *S. mansoni*-infizierte Mäuse injiziert und auf ihren Einfluss auf die Krankheitspathologie untersucht. Zum Zeitpunkt der Analyse hatte die Verabreichung von EVs keinen wesentlichen Einfluss auf die Rekrutierung von Immunzellen in die Leber und auf die Belastung mit parasitären Eiern in der Leber. Allerdings waren die Alanin-Aminotransferase -Werte im Serum, ein Indikator für Leberschäden, bei Mäusen, die aT-EVs erhalten hatten, deutlich niedriger im Vergleich zu unbehandelten Kontrollen. Weitere Experimente sind erforderlich, um festzustellen, ob der Transfer von aT-EVs das Fortschreiten der Leberfibrose zu späteren Zeitpunkten der Erkrankung beeinflussen könnte. Darüber hinaus wurden EVs aus den Lebern von *S. mansoni*-infizierten Mäusen isoliert und auf ihre Zusammensetzung und ihre Fähigkeit zur Regulierung des Signalwegs für die Stickstoffmonoxid Produktion in Mϕs im Vergleich zu Leber-EVs von naïven Mäusen untersucht.

Zusammenfassend konnte gezeigt werden, dass aT-EVs im Vergleich zu liveT-EVs einen geringen Unterschied im Einfluss auf den Phänotyp, die Polarisierung und die Funktionalität von Mϕs haben.

Dennoch besitzen aT-EVs andere Eigenschaften als liveT-EVs, können in wichtige Zellsignalwege eingreifen und könnten den Krankheitsverlauf der Schistosomiasis beeinflussen. EVs, die in den Lebern von mit *S. mansoni* infizierten Mäusen freigesetzt werden, beeinflussen ähnlich wie aT-EVs den Signalweg für die Stickstoffmonoxid Produktion in Mϕs. Weitere Untersuchungen der Zusammensetzung der EV-Fracht und deren Interaktion mit den Zielzellen sind erforderlich, um das therapeutische Potenzial von EVs, unabhängig davon, ob diese von apoptotischen oder lebenden Zellen stammen, vollständig zu aufzuklären.

1 Introduction

1.1 Extracellular vesicles (EVs)

Extracellular vesicles (EVs) were first described to be released by reticulocytes during maturation *in vitro* in 1987. Johnstone et al. isolated EVs from the culture supernatant via ultracentrifugation and discovered that they contained characteristics and activities similar to pre-mature reticulocytes[1]. Ever since then, EVs have become an uprising field of interest, as research has progressively shown their importance in intercellular communication. With the upcoming advances in EV research, the International Society for Extracellular Vesicles (ISEV) created guidelines aiming for standardisation of definition terms and protocols to raise robustness in EV research[2–4]. According to these guidelines EVs are defined as nanoscale-sized particles delimited by a lipid bilayer that get released by cells and cannot replicate on their own[4].

EVs can be further sub-categorized by their biogenesis pathway. Exosomes are formed from internal compartments of the cell and are actively released via multivesicular bodies (MVB), whereas ectosomes bud directly from the cell surface plasma membrane[5]. However, common isolation techniques do not allow the separation of EVs by their biogenesis pathway so far. Therefore, most EV isolates consist of a pool of EVs. The EV subsets are also often defined by their difference in size, as exosomes are usually the smallest type ranging from 50 – 150 nm and ectosomes are generally larger ranging from 100 – 500 nm in diameter [5]. Additional EV subtypes were discovered and named referring to their cellular sources, such as oncosomes, which get released by tumour cells or apoptotic bodies that form when a cell is undergoing programmed cell death, which are both generated by outward budding and fission of the plasma membrane. Both are known as the largest types of EVs that can even be as large as up to 5 µm in diameter [5].

Commonly used terms to avoid false labelling of EV subsets by their biogenesis are small EVs (<200 nm) and large EVs (>200 nm), as most isolation techniques, such as isolation via differential ultracentrifugation, aim to separate EVs by their difference in size and density and therefore separation at increasing ultracentrifugation speeds. Yet it has to be considered that it does not allow a clear size cut-off and usually leads to the yielding of mixed-size EV populations.

1.1.1 Biogenesis

As briefly mentioned above, the biogenesis of exosomes and ectosomes is determined by two different mechanisms that both involve plasma membrane trafficking processes. The generation of exosomes is initiated within the endosomal pathway, which is involved in the internalisation of extracellular ligands

or cellular components, their recycling, and transport to the plasma membrane or degradation. Herein intraluminal vesicles (ILVs), accumulate during the maturation of early endosomes into late endosomes, also referred to as MVBs[6]. As MVBs are formed during endocytosis, exosomes carry specific protein markers of the endosomal pathway, particularly proteins involved in vesicle formation, such as the tetraspanin CD63 and major histocompatibility complex class II (MHC-II)[7]. The formation and release of exosomes can either take place dependent on the endosomal sorting complex required for transport (ESCRT), which is involved in ILV formation, cargo sorting and membrane fission or, independently of the ESCRT, via tetraspanins and other membrane-associated proteins[8,9]. Exosomes are then released by the fusion of MVBs with the plasma membrane within the secretory pathway[10]. The exact pathways determining if the MVB fuses with the plasma membrane and exosomes are released into the extracellular space or if the MVB fuses with the lysosome and its content gets degraded, remain to be investigated[11]. Ectosomes are secreted by outward budding from the cells' plasma membrane, which requires rearrangement within the plasma membrane and the influx of Ca^{2+}. In response to the activation of cellular processes in a Ca^{2+}-dependent manner, phosphatidylserine is translocated from the inner leaflet of the membrane to the cell surface, resulting in physical bending of the plasma membrane and following restructuring of the actin cytoskeleton. In consequence, this triggers membrane budding causing the formation of ectosomes[12]. Apoptotic bodies are a form of ectosomes only released when a cell undergoes cell death and will be introduced further in detail in the following chapters. In brief, their biogenesis is initiated by caspases activated by the apoptosis pathway. Caspases mediate cleavage of Rho-associated kinase 1 (ROCK1) leading to the formation of membrane blebs and of the membrane channel Pannexin 1 which is involved in the regulation of size as well as nuclear content packaging of apoptotic bodies[13,14].

1.1.2 Cargo selection

As EVs are constantly released by every cell type, their content highly reflects the status of their cells of origin. EV cargos are composed of membrane proteins, cytosolic proteins, nucleic acids, and lipids, and their content varies widely depending on their cellular source and the stimuli and mechanisms of their biogenesis. Though the biogenesis of EVs might be very different and occur at different sites of the cell, they share common sorting machinery for cargo trafficking. Selective packaging of EV cargo is still undergoing extensive research as many questions remain unanswered. But what is understood so far, is that during EV biogenesis cargos are targeted to the site of EV production and further enriched inside the forming vesicle before their release into the extracellular space[15]. Cargo selection of transmembrane proteins takes place during biogenesis via ubiquitination and recognition by ESCRT components in both, exosomes and ectosomes[16]. The incorporation of cytoplasmic cargos into EVs is

so far much less understood. There is increasing evidence that EV cargos, especially RNA contents, are selectively sorted into EVs, as EVs have shown to be enriched in specific RNAs relative to their donor cells[17–19]. Particularly, studies have focussed on revealing the molecular mechanisms mediating targeted incorporation of miRNAs into small EVs. Multiple RNA-binding proteins (RBPs) that bind to specific sequence motifs of miRNAs at the site of EV biogenesis and mediate their incorporation into EVs via interaction with components of the ESCRT pathway have been identified. The RNA binding protein FMR1 has been shown to be actively recruited to the MVB during exosome formation by the cleaved caspase-1 activated Rab7 adaptor protein. At the site of EV biogenesis, FRP1 binds miRNA expressing the sequence AAUGC and interacts with hepatocyte growth factor–regulated tyrosine kinase substrate (Hrs), a member of the ESCRT pathway, resulting in the release of exosomes containing miRNAs with the RBP-binding motif[20,21]. Besides miRNA, mRNA fragments and long non-coding RNAs are also sorted into small EVs through interaction with RBPs[22]. Many proteins and machinery involved in EV biogenesis and selective cargo incorporation have been discovered so far, nevertheless, the underlying molecular mechanisms remain largely unknown.

1.1.3 Targeting of recipient cells

Once released into extracellular space, EVs encounter and target their recipient cells contributing to communication between distant cells. Proteins enriched on the EV surface might determine their target cell specificity, as the EV cargos on the surface are the first being presented to the recipient cell. Subsequently, induction of receptor-ligand interaction allows interference with signalling events of the target cells, either directly downstream of the receptor-ligand interaction on the cells' surface or upon endocytosis[5]. Again, the exact mechanisms determining the specific targeting of effector cells require extensive research. Yet, a few interacting molecules have been identified, such as integrins on the EV surface binding to intercellular adhesion molecules (ICAMs) on the cell surface[23] or to extracellular matrix (ECM) proteins[24]. Lipid-binding proteins can also be involved in target cell docking and are recruited by lipids such as phosphatidylserine on the EV surface[12].

Whereas surface epitopes of the EVs can induce direct signalling events via binding to the target cells, intravesicular cargos require internalisation by the recipient cell in order to be released. It is still not clear to this point if the uptake of EVs is target-specific or if it is unspecific and stochastic, but what is known is that EV internalisation occurs through multiple routes that involve endocytosis[25], phagocytosis by macrophages (Mϕs) or fusion with the plasma membrane[26,27].

Despite the mechanism of their uptake, EVs have been shown to be powerful modulators of signalling pathways in their target cell, thereby impacting their phenotype and function[28]. Especially in several disease settings, EVs seem to play a key role in manipulating the immune system and thereby

influencing the disease outcome[29,30]. From a clinical point of view, EVs are a promising candidate for the development of new methods for drug and vaccination delivery and might serve as biomarkers for several diseases[31,32]. The functional properties of EVs, the underlying molecular mechanisms investigated so far and the potential for future therapeutic applications will be further elucidated in the following chapters. A brief schematic overview of the biogenesis and uptake of extracellular vesicles is depicted in Figure 1.

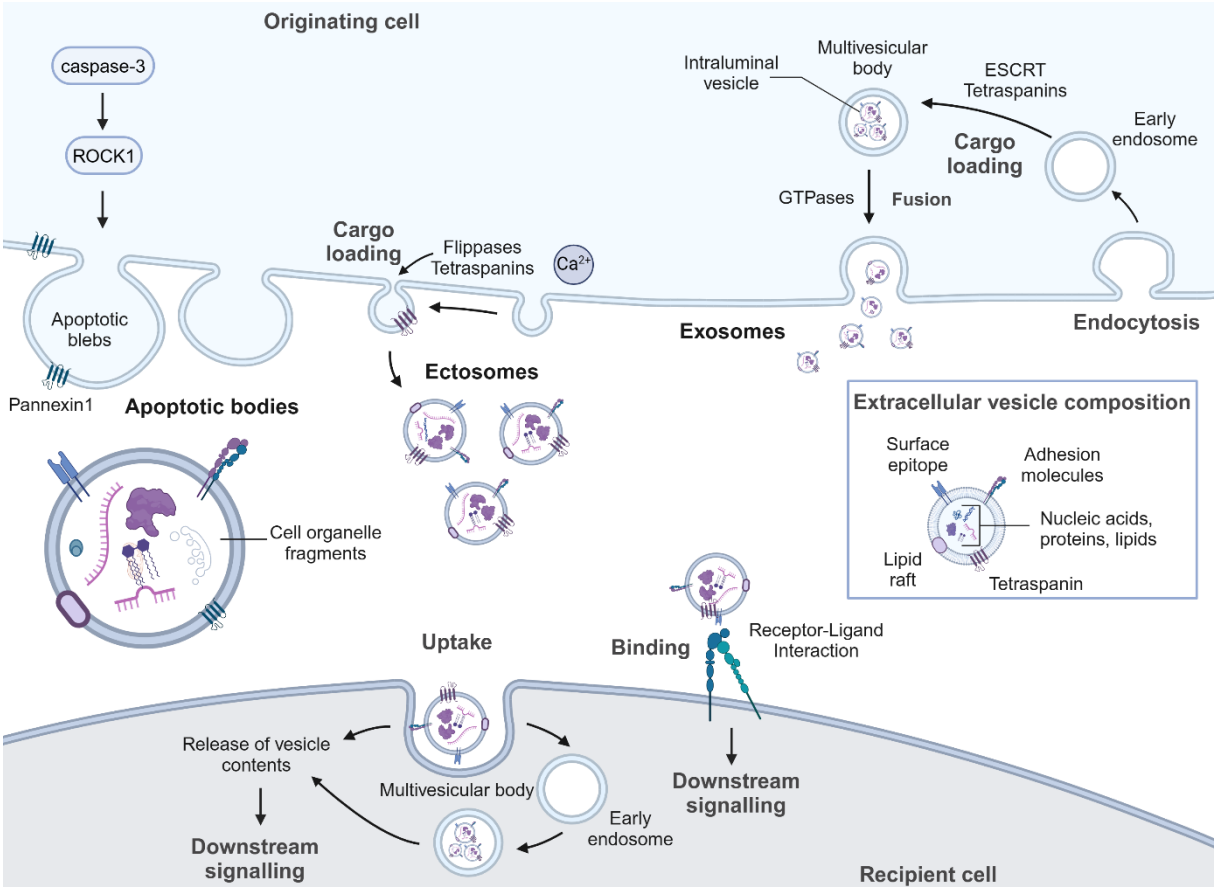


Figure 1: Schematic overview of the biogenesis and uptake of extracellular vesicles. Extracellular vesicles can be secreted via different mechanisms from the originating cells. Exosomes are formed during the endosomal pathway in multivesicular bodies. Their formation and cargo loading involve the ESCRT machinery or tetraspanins together with other membrane-associated proteins. Exosomes get released from multivesicular bodies by GTPase-dependent fusion with the plasma membrane. Ectosomes are formed by direct budding from the plasma membrane in a Ca^{2+}-dependent manner activating physical bending of the plasma membrane through flippases and tetraspanins. Apoptotic bodies are a special form of ectosomes as they only form when a cell undergoes apoptosis. Thereby caspase-3 cleavage of substrates such as ROCK1 and Pannexin 1 activates the formation of apoptotic blebs resulting in the fragmentation of an apoptotic cell into apoptotic bodies. Extracellular vesicles contain bioactive molecules that can interfere with the signalling and function of their recipient cell via receptor-ligand interaction on the cell surface or upon uptake.

1.2 Apoptosis

Apoptosis is a programmed form of cell death that involves the genetically determined elimination of cells. Cells normally undergo apoptosis during development and ageing, which is an essential mechanism for retaining homeostasis in tissues[33,34]. Apoptosis does not only occur under physiological conditions but becomes even more important under pathological conditions, being a defence mechanism as part of the immune response or protection against damaged cells[35]. Apoptosis can be induced by intrinsic or extrinsic pathways, which can be triggered by a wide variety of signals, but not all cells respond to the same stimulus. Induction of the extrinsic pathway is induced by ligand binding to death receptors expressed on the cell surface, for example, Fas ligand (FasL) binding to Fas receptor (FasR) or Tumour necrosis factor α (TNF-α) binding to the TNF receptor 1[36]. Cells also have an intrinsically programmed default death pathway that requires blocking by survival factors such as hormones or growth factors, if these factors are lacking, apoptosis is induced in response. Intracellular stress, irradiation or cytotoxic components can induce, for example, DNA damage, endoplasmatic reticulum stress and growth factor deprivation causing the activation of B-cell lymphoma 2 (BCL-2) proteins[37]. The BCL-2 protein family consists of multiple proteins exhibiting pro- and anti-apoptotic functions and their activation triggers the release of cytochrome c from the mitochondrial intermembrane space resulting in the activation of cleaved caspase-9 and subsequently apoptosis[37]. However, these two pathways might be linked and molecules from one pathway can interfere with the other[38]. Both pathways terminate in the same protease cascade, also named the execution pathway. Caspase-3 is considered the most important of the executioner caspases and is activated by any of the initiator caspases[39]. Cleaved caspase-3 activates endonucleases that degrade DNA and cause chromatin condensation[40]. Hereby, the shrinking of the cells and chromatin condensation characterise the first morphological changes of an early apoptotic cell[41]. Caspase-3 also induces cytoskeletal rearrangement and membrane blebbing resulting in the fragmentation of the cell into apoptotic bodies during late apoptosis[42]. Additionally, caspase-3 is involved in the translocation of phosphatidylserine from the inner leaflet of the membrane to the cell surface[43–45]. Phosphatidylserine exposure allows the detection and clearance of apoptotic cells by Mϕs through a process called efferocytosis, which will be further elaborated in Chapter 1.3.3.

1.2.1 Extracellular vesicles released during apoptosis

Cells undergoing apoptosis dissemble into apoptotic bodies that are per definition extracellular vesicles. They could even be classified as ectosomes as they form by budding of the plasma membrane but because of their generally larger size (roughly 500 – 5000 µm), they are often defined as an individual subtype. The function of apoptotic bodies has long been thought to be limited to the

packaging of cell junk, allowing Mϕs to phagocyte the apoptotic cell fragments and to shield the cell death from recognition of the immune system to prevent inflammation and sustain homeostasis[46–48]. Another long-neglected fact is that apoptotic cells do not only release apoptotic bodies but also smaller types of extracellular vesicles, such as exosomes and ectosomes. Evidence indicates that EV released by apoptotic cells (ApoEVs) have an impact on cellular communication in health and disease, mediated by the diverse cargoes they contain, including DNA, RNA, proteins, and even organelles such as mitochondria and ribosomes. The membrane composition of ApoEVs often reflects the topology of their apoptotic cell of origin regarding their phospholipid, and glycan content as well as their surface proteins. A characteristic that might distinguish ApoEVs from EVs released by live cells might be a specific pattern of galactose and N-acetylgalactosamine[49]. These characteristic patterns have been shown to originate from cleaved caspase-mediated modifications of the glycosylation patterns of the endoplasmatic reticulum in the apoptotic cells and are suggested to contribute to the recognition of effective clearance of ApoEVs by Mϕ and hepatocytes[50]. Additionally, ApoEVs have been shown to contain caspase-cleaved proteins, such as ROCK1 and Pannexin 1 that can be intravesicular or displayed on their plasma membrane[51]. As caspases are involved in EV formation, release, cargo sorting, and processing, as well as EV uptake, it is not surprising that ApoEVs have been reported to contain cleaved caspase-3 itself[52–54].

Emerging evidence indicates that ApoEVs are inheriting the communicative properties of their apoptotic cell of origin in regulating tissue homeostasis[50]. EVs derived from apoptotic mesenchymal stem cells (MSCs), for example, have been shown to engraft in the liver of recipient mice, undergo specialised internalisation by hepatocytes in dependence on galactose and N-acetylgalactosamine displayed on their surface and contribute to liver regeneration and protect against acute hepatic failure. Contrary to this, in certain contexts, ApoEVs have also been suggested to have immunostimulatory and pro-inflammatory functions as they can be enriched in autoantigens[55,56]. Apoptotic bodies isolated from apoptotic lymphoblasts, for example, accumulate autoantigens like histones and DNA that might be relevant for the pathogenesis of auto-immune diseases such as systemic lupus erythematosus. These apoptotic bodies were engulfed by monocyte-derived phagocytes suggesting they might either provide a silent and non-immunogenic clearance of autoantigens or their distribution. Another very interesting study showed that ApoEVs isolated from the murine thymus are able to present a broad variety of chemokines such as CCL2, CCL11, CXCL11, and CCL20 on their surface. The chemokines bind to phosphatidylserine exposed on the EV surface and are able to activate cognate chemokine receptors expressed by phagocytes. Thereby, they are suggested to contribute to the guidance of phagocytes towards apoptotic cells[57]. Most likely the capacity of ApoEVs to activate diverse inflammatory, anti-inflammatory, immunostimulatory, or tolerogenic responses, strongly depends on the context of their origin. Thereby, a lot of questions

remain to be answered in future studies targeting the biogenesis of ApoEVs, their cargo loading, their functional impact on recipient cells, and their potential utility in clinical applications.

1.3 A brief introduction to the immune system

The immune system is the host's defence mechanism against potential pathogens and sterile perturbations, protecting the host organism from disease. The immune system comprehends an innate and adaptive immunity component, with both parts closely cooperating with one another. The recognition and elimination of pathogens require the complex interplay of humoral and cellular components of both parts of the immune system in a tightly regulated manner. Thereby innate immunity provides the first line of defence against pathogens that enter the organism. The humoral part of the innate immune system is the complement system. It consists of various circulating proteins that attack pathogens' cell membranes, promote inflammation, and enhance the ability of immune cells to clear the organism from pathogens. Cells of the innate immune system include phagocytes, granulocytes, innate lymphoid cells, and natural killer cells (NK cells). These cells are able to identify pathogens displaying pathogen-associated molecular patterns (PAMPs) and damage-associated molecular patterns (DAMPs), released by damaged cells, by the expression of pattern recognition receptors (PRRs)[58]. Recognition of such structures results in the recruitment, activation, and differentiation of further immune cells mediated by the release of cytokines, such as IL-1, IL-6, and TNF. Granulocytes (neutrophils, eosinophils, basophils, and mast cells) and NK cells can release toxic substances like free oxygen radicals or perforin and granzymes enabling them to kill pathogens directly[59].

Mϕs, neutrophils, and dendritic cells (DCs) are phagocytes that internalise recognised pathogens via phagocytosis. Phagocytes envelop the pathogen through complex extrusion of the plasma membrane and trap them in an intracellular vesicle called the phagosome. The phagosome subsequently fuses with the lysosome, to form a phagolysosome, where the pathogen is killed through various mechanisms. The lysosome contains acids and digestive enzymes that are capable of destroying pathogens and a respiratory burst can lead to the release of free radicals into the phagolysosome which are toxic to the ingested pathogens[60,61]. However, phagocytosis is not only used to eliminate pathogens but also an important regulator of tissue development and maintenance which will be further highlighted in the following chapters.

Whereas the humoral and cellular components of the innate immune system recognise conserved structures of pathogens, the adaptive immune system, consisting of B and T cells, is characterised by its high specificity, which is mediated by unique and highly variable receptors, the B cell receptors (BCRs) and the T cell receptors (TCRs). T cell development starts when progenitors migrate from the

bone marrow to the thymus. In the thymus, they undergo positive selection for the affinity to bind to MHC molecules. Positively selected naïve T cells leave the thymus entering the lymphatic system, where they circulate until they encounter their cognate antigen presented by an MHC complex. DCs, B cells and Mϕs are termed professional antigen-presenting cells (APCs). Those professional APCs can activate multiple subsets of T cells. Hereby, MHC-II molecules display exogenous antigens, which activate $CD4^+$ helper T cells, whereas endogenous antigens are typically displayed on MHC class I (MHC-I) molecules and activate $CD8^+$ cytotoxic T cells. $CD4^+$ T cells can be subcategorised by their polarisation state in T helper 1 (Th1) and T helper 2 (Th2), which are characterised by different cytokine-production profiles. Th1 cells primarily produce Interferon-gamma (IFN-γ) and generally provide protection against intracellular pathogens, whereas Th2 cells mainly produce IL-4, IL-5, and IL-13, and are crucial for the immune response to helminth parasites and allergens[62]. Successful binding of the highly specific TCR complex to their cognate antigen presented on MHC molecules and binding of the CD4 or CD8 coreceptor to the respective MHC-II or MHC-I molecules induces further maturation of the T cell to effector T cells, memory T cells or regulatory T cells[59].

While T cells recognise antigens in a processed form presented by MHC complexes, B cells recognise antigens in their native form. The BCR expressed by B cells is a membrane-bound antibody molecule. BCRs of one clone of B cells recognise and bind only one specific antigen. The binding of B cells to their specific antigen in addition to signals from a helper T cell causes their differentiation into antibody-producing plasma cells. Antibodies provide the humoral part of the adaptive immune. They bind antigens with a very high specificity and affinity, enabling multiple immunological processes. Coating of the antigen with antibodies leads to neutralisation of pathogens and activation of the complement cascade. It enhances phagocytic activity and induces cell-mediated cytotoxicity, causing the destruction of pathogens and infected cells by Mϕs, eosinophils and NK cells[59].

1.3.1 Macrophages (Mϕs)

Mϕs are a versatile population of cells that is designated by its high functional and transcriptional heterogeneity and plasticity. They do not only play a key role during an immune response but are also essential for the maintenance of tissue homeostasis. Mϕs can be either resident within tissues or circulate through the organism until they are recruited to a site of inflammation. Tissue-resident Mϕs are present in every tissue; thus, their phenotype can be very distinct between tissues. This heterogeneity is driven by multiple factors such as their progenitor cells, development, and the tissue microenvironment. Whereas resident liver Mϕs, also named Kupffer cells, originate from fetal liver Mϕs, Mϕs resident in the brain derive directly from yolk sac progenitors, and small peritoneal Mϕs, in

turn, develop from blood-derived monocytes[63–66]. In the peritoneum, a second developmental and functional distinct Mϕ population, the large peritoneal Mϕs, arises from self-renewal[67].

Even within a tissue, Mϕs have high phenotypic diversity and function. Kupffer cells, for example, exert heterogeneous functions according to their localisation within the tissue. In the peri-portal regions of the liver lobules, Kupffer cells appear larger, highly phagocytic, and show lower responsiveness to inflammatory stimuli. Conversely, in the peri-central regions, they are strongly engaged upon inflammatory stimuli and show high levels of MHC-II and nitric oxide (NO)[68]. Infiltrating Mϕs derive from monocytes that get recruited from the blood to the site of inflammation. Multiple environmental factors can attract monocyte-derived Mϕs such as metabolites released from apoptotic cells, growth factors, pro-inflammatory cytokines, chemokines or microbial products[69,70]. Recruited monocyte-derived Mϕs can rapidly adapt to the tissue environment, support the local immune response, and provide pathogen defence. Depending on the severity of the tissue damage and the niche availability, monocyte-derived Mϕs can engraft in the tissue and support or actually replace tissue resident Mϕs temporarily or even permanently[71].

1.3.2 Mϕ polarisation

A factor highly contributing to Mϕ heterogeneity is their potential to polarise according to factors they encounter in their tissue microenvironment. Various nomenclatures exist that try to classify Mϕs by their polarising factors and marker expression[72]. In this thesis, the broad terms pro-inflammatory and anti-inflammatory Mϕs will be used to describe their polarisation state. Albeit their heterogeneity, Mϕs can be characterised by common features like the expression of the surface markers CD11b, F4/80, and CD64[73]. Other surface markers allow the identification of Mϕs depending on their tissue specificity such as Car4 in the lung, Clec4F in the liver, or CCR2 and Ly6C for infiltrating Mϕs[74,75]. Highlighting their potential and plasticity, studies showed that bone-marrow monocytes, yolk-sac Mϕs, and fetal liver monocytes transferred into the lungs of mice lacking alveolar Mϕs were able to mature into Car4 expressing alveolar Mϕs with almost identical gene expression profiles and functions[76].

Sensing of pro-inflammatory cytokines such as IFN- γ in the environment triggers a number of signalling cascades within the Mϕ, which subsequently initiates the expression of pro-inflammatory signature markers such as inducible nitric oxide synthase (iNOS), MHC-II, CD80, and CD86 and the secretion of secrete pro-inflammatory cytokines, for instance, TNF, IL-1, IL-6, and IL-12, which further contribute to the recruitment and activation of immune cells[77,78] (Figure 2). Particularly, the upregulation of iNOS plays a crucial role in the pro-inflammatory response as it leads to the production of NO and other reactive oxygen species[79]. NO is a cytotoxic bioactive molecule that can directly induce pathogen killing

and mediate a pro-inflammatory immune response, but in consequence, also causes tissue damage. In order to keep the tissue damage limited, excessive amounts of NO lead to the suppression of further pro-inflammatory Mϕ differentiation[80,81].

Following a pro-inflammatory immune response, the anti-inflammatory counterpart is crucial in order to regulate acute inflammation, dampen tissue damage, initiate tissue repair, and restore homeostasis. Sensing of anti-inflammatory cytokines such as IL-10 and IL-4 or IL-13 in symphony with other signals such as phosphatidylserine from apoptotic cells initiates the polarisation of Mϕs towards an anti-inflammatory phenotype[82]. The genetic program driving Mϕ polarisation is still largely unknown. Our group recently identified *Nmes1* as a contributor to the early Mϕ response to IL-4 *in vitro*, controlling the expression of a series of anti-inflammatory potential transcription factors such as *Gata3* and *Ahr*[83].

Anti-inflammatory Mϕs express a variety of markers such as CD206, Arginase 1 (ARG1), resistin-like molecule α (RELMα), and chitinase-like protein 3 (YM1), which are needed for tissue remodelling. In addition, they produce anti-inflammatory cytokines like IL-4 and IL-10, and growth factors such as transforming growth factor β (TGF-β), vascular endothelial growth factor (VEGF), and platelet-derived growth factors (PDGFs)[84–86] (Figure 2). These proteins all contribute to the tissue remodelling function of Mϕs. TGF-β signalling, for example, leads to collagen synthesis and inhibition of NO production and enhances ARG1 expression[87]. ARG1 interferes with the NO synthesis pathway by competing with iNOS for the substrate L-Arginine. ARG1 is involved in the conversion of L-Arginine into the essential amino acid proline, which is involved in collagen production and cell proliferation signalling[88]. Released growth factors such as VEGF and PDGFs contribute to angiogenesis and fibroblast proliferation[89]. In consequence, anti-inflammatory Mϕs enhance cell division and recruitment, tissue integrity, and wound healing.

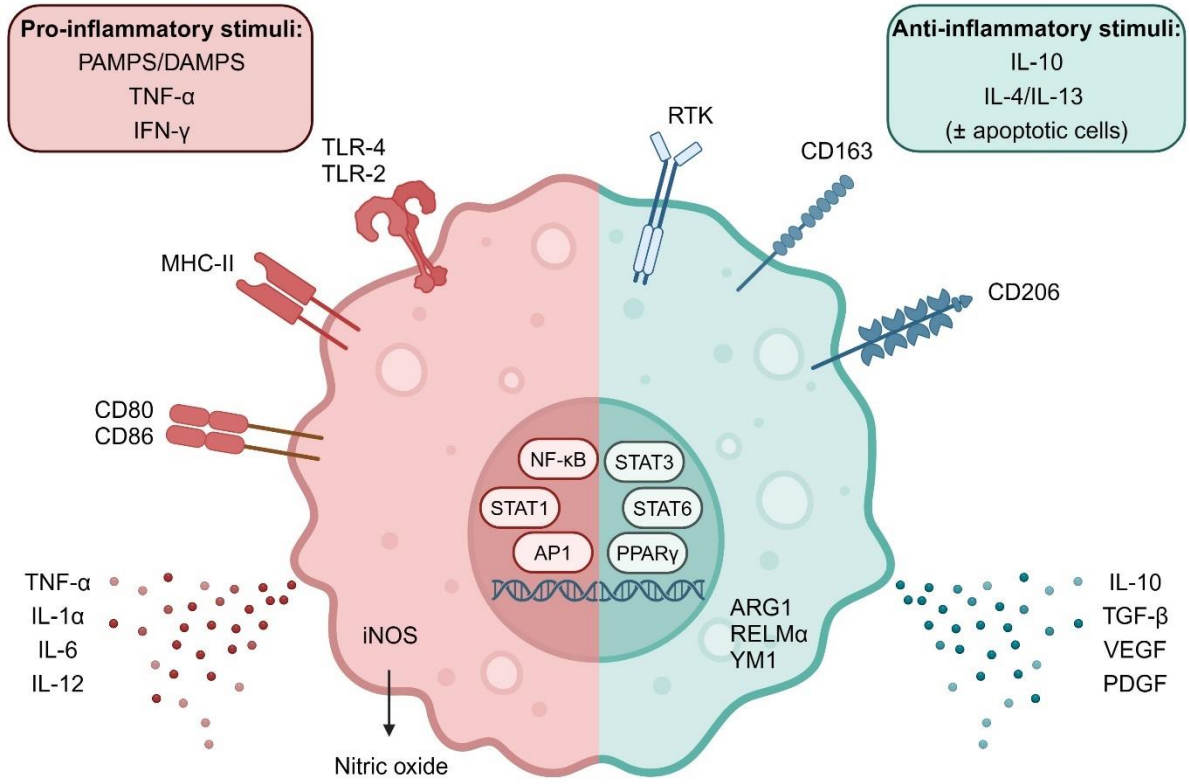


Figure 2: Schematic overview of factors determining Mϕ polarisation. Pro- or anti-inflammatory polarisation of Mϕs is determined by sensing of environmental stimuli. Pro-inflammatory Mϕs typically express the receptors CD80, CD86, TLRs, and MHC-II among others, as well as the protein iNOS producing nitric oxide. Pro-inflammatory activation of a Mϕ results in the activation of multiple signalling pathways and transcription factors and the production of cytokines such as TNF-α, IL-1, IL-6 and/or IL-12. Sensing of IL-10 or apoptotic cells in addition to IL-4 or IL-13 induces the anti-inflammatory polarisation of Mϕs. Anti-inflammatory Mϕs typically express receptors such as RTKs (e.g. MERTK and Axl), CD163 or CD206 and proteins such as ARG1, RELMα and YM1. The activation of anti-inflammatory signalling pathways activates multiple transcription factors resulting in the production of anti-inflammatory cytokines and growth factors, for example, IL-10, TGF-β, VEGF or PDGF.

1.3.3 Efferocytosis

Amongst the factors in a tissue environment that drive Mϕ polarisation, the phagocytosis of apoptotic cells through a process called efferocytosis contributes to the alteration of the Mϕ activation status. Apoptotic cells release soluble factors and present specific markers, known as “find me” and “eat me” signals respectively. Sensing of these molecules by Mϕs is their signal to start the efferocytosis program. “Find me” signals include chemokines, ATP and UTP and attract phagocytes via a chemokine gradient. Once Mϕs are attracted to the apoptotic cells, interaction with the exposed “eat me” signals such as ICAM or phosphatidylserine is initiated[90,91]. Phosphatidylserine, for example, is recognised by phagocytosis receptors on the Mϕs such as TIM4, CD36 or MERTK and AXL and initiates efferocytosis. TIM4 can bind phosphatidylserine directly whereas CD36 requires thrombospondin as a bridging

molecule between the phagocytosing Mϕ and the apoptotic cell[92,93]. In the case of the receptor tyrosine kinases (RTKs) MERTK and Axl, phosphatidylserine binding requires the bridging molecules Protein S (Pros1) and growth arrest-specific 6 (Gas6). Both these molecules bind to phosphatidylserine in a Ca^{2+}-dependent manner, but on the side of the receptor, Gas6 has a higher affinity for Axl than MERTK, whereas Pros1 can bind to MERTK. The binding of these bridging molecules to apoptotic targets triggers downstream activation of the RTKs starting the efferocytosis machinery and simultaneously contributes to the inhibition of inflammation, for example, by the production of anti-inflammatory cytokines and upregulation of suppressor of cytokine signalling (SOCS) gene expression[94–96].

Importantly, our group recently proved that apoptotic cells should not be taken as a homogenous population, but that indeed the original identity of the apoptotic cell type is critical for the guidance of phenotypical and functional alterations in the Mϕs. Depending on the apoptotic cells they encounter, Mϕs preferentially engage different types of phagocytic receptors. Mϕs require these distinct phagocytic receptors to be able to engulf specific types of apoptotic cells. Axl and MERTK, for instance, are required for taking up apoptotic neutrophils, partially T cells, but not apoptotic hepatocytes. Signalling cascades induced by the engagement of these receptors could be a potential mechanism regulating the acquisition of different Mϕ signatures[97]. If and how EVs released by the apoptotic cells also contribute to these properties remains to be answered.

1.3.4 Interaction of Mϕs and EVs

Whereas the phagocytosis of the apoptotic cell corpse has been extensively studied, little is known about the interaction, uptake, and cargo processing of ApoEVs by Mϕs. In line with the facts that certain receptors for the recognition of apoptotic cells such as TIM4 have been shown to equally function as receptors for EVs[98] and that ApoEVs contain cargos representative of the state of their cell of origin, it is likely that they execute functions similar to the ones of phagocytosed apoptotic cells.

So far ApoEVs have been shown to participate in the enhancement of efferocytosis and the polarisation of anti-inflammatory Mϕs[99]. ApoEVs carrying the “find me” signal CX3CL1 have been shown to enhance efferocytosis via induction of milk fat globule-epidermal growth factor 8 (MFG-E8)[100]. MFG-E8 contained in EVs released by MSCs has also been reported to promote cardiac tissue repair in acute myocardial infarction by enhancing Mϕ phagocytosis[101]. MSCs are multipotent progenitors that can be isolated from a variety of tissues including the bone marrow and differentiate into multiple cell types such as adipocytes, osteocytes and chondrocytes. They interact with the innate and adaptive immune system and harbour great potential for tissue regeneration and have therefore been extensively studied for therapeutical applications[102].

ApoEVs can also expose “eat me” signals like phosphatidylserine to be recognised by Mϕs for removal via phagocytic receptors such as CD36[103]. Expression of the “eat me” signal ICAM-3, for example, has been shown to trigger their recognition and engulfment by Mϕs[104].

ApoEVs isolated from human T cells have been reported to contain autoantigens, which in combination with IFN-α triggered an increase in phagocytosis in PBMC-derived monocytes and pro-inflammatory Mϕ polarisation via STAT1 signalling *in vitro*[105]. ApoEVs released by thymocytes were shown to promote TGF-β production of Mϕs and anti-inflammatory polarisation through phosphatidylserine and FOXO3-mediated signalling. Administered *in vivo* in a model of experimental colitis, these ApoEVs suppressed the type 1 immune response, promoted the differentiation of regulatory T cells, and ameliorated the disease[106] In the context of type 2 diabetes, ApoEVs isolated from MSCs have been shown to functionally modulate liver Mϕ in an efferocytosis-dependent manner leading to inhibition of Mϕ accumulation and polarisation towards an anti-inflammation phenotype[107].

ApoEVs from DCs have been shown to carry MHC-II molecules suggesting their potential to directly present antigens and activate $CD4^+$ T cells[108]. Uptake of ApoEVs by APCs might also modulate their antigen-presenting capabilities, as ApoEVs released by lymphoblasts were found to downregulate MHC-II molecules on DCs, hence suppressing immune responses[109] and antigens as ApoEV cargos might be further cross-presented upon phagocytosis by APCs. In addition to antigens, ApoEVs have been shown to carry cytokines and DAMPs that are capable of modulating the immune response. Larger ApoEVs derived from endothelial cells carry IL-1α, which induces monocyte chemotactic protein-1 (MCP-1) and IL-8 secretion by endothelial cells *in vitro*. *In vivo*, injection of ApoEVs derived from endothelial cells into the peritoneal cavity leads to neutrophil infiltration and might thereby contribute to the amplification of the inflammatory response to sterile inflammation[110]. ApoEVs from lymphoblasts have been shown to carry DNA which acts as a DAMP by activating TLR9 signalling in DCs. This, in turn, causes the release of IFN- α, which is involved in immune tolerance and autoimmune diseases[110,111]. However, their direct effect on Mϕs has not yet been investigated.

Studies on the potential of EVs from live cells, also highlight the importance of surface markers for the communication between EVs and Mϕs. EVs from live neutrophils have been shown to induce an anti-inflammatory and immunosuppressive response in human monocyte-derived Mϕs *in vitro*. The suggested underlying mechanism is that phosphatidylserine on the EVs activates the PI3K/Akt signalling pathway in a MERTK-dependent manner resulting in the blockade of NF-κB and thereby down-regulation of pro-inflammatory cytokine production such as TNFα, IL-1β, IL-6, IL-8, IL-10, and IL-12[112], but if EVs from apoptotic neutrophils might have similar effects, remains to be investigated. CD47, a “don’t eat me” signal that protects cells from phagocytosis, has been identified on the surface of EVs from fibroblasts *in vitro*. It was shown to prevent EV phagocytosis by Mϕs and monocytes

thereby increasing their circulation time in the blood, allowing engineered ApoEVs to reach their target with higher efficacy compared to liposomes without CD47[113]. Hence, further identification and deeper characterisation of ApoEV cargos and investigation of the effects they have on target cell signalling and functionality is needed to reveal their role in cellular communication, which in the future perspective may open doors for the development of EVs from dying cells as new therapeutic approaches.

1.4 Schistosomiasis

Schistosomiasis is the second most abundant neglected tropical disease worldwide with an estimated number of 250 million infected people worldwide. It is caused by the infection of a host through contaminated water with the larval forms (*Cercariae*) of the parasitic trematode *Schistosoma spp*. released by freshwater snails. Schistosomiasis is transmitted via contamination of freshwater sources with faeces or urine from infected individuals containing parasite eggs, which hatch in water. Therefore, it is especially prevalent in rural and poor communities in tropical and subtropical areas without adequate sanitation and access to safe drinking water [114].

There are 5 infectious *Schistosoma species* (*S. spp*.), therein *S. mansoni*, *S. japonicum*, *S. mekongi*, and *S. guineensis/S. intercalatum*, which cause intestinal symptoms, and *S. haematobium* causing urogenital schistosomiasis. They differ not only in the symptoms and tissue pathologies developing in the host but also in their geographical distribution. This thesis focuses on infection with *S. mansoni*, which is the most spread species in Africa, the Middle East, the Caribbean, Brazil, Venezuela, and Suriname. Symptoms of intestinal schistosomiasis during the acute phase of the disease can be abdominal pain, diarrhoea, and blood in the stool. If not treated, a chronic onset of the disease can follow, leading to liver fibrosis, failure, and eventually death. The number of deaths caused by schistosomiasis is probably highly underestimated, because of its hidden pathologies. Lacking treatment options is especially threatening for children, as an untreated disease can cause anaemia, stunting, and a reduced ability to learn. Currently, Praziquantel is the main drug of choice for preventive chemotherapy and treatment as it is cheap, has high efficacy against mature parasites, and has mild side effects. However, using praziquantel re-infections are common, because it is less effective against juvenile forms of the parasite. Thereby repeated application of the drug increases the risk of resistance development and reduction of its efficacy [114,115]

As a consequence of schistosomiasis, several million people all over the world suffer from severe morbidity making it a serious threat to health and economics in its endemic areas and require the necessity for the development of new prevention and treatment strategies, therefore the mechanisms by which *Schistosoma* parasites affect the host immune response have to be further investigated.

1.4.1 *S. mansoni* life cycle

The *S. mansoni* life cycle begins when alongside contaminated faeces or urine from a mammalian host, parasite eggs are released into freshwater. In the water eggs hatch into *Miracidia*, which can infect freshwater snails, its intermediate host. In the snail, development, and asexual reproduction of the *Miracidium* into *Cercariae* is initiated. The *Cercariae* are the infective stage of the parasite able to penetrate the skin of the mammalian host, where they develop into *Schistosomulae*. *Schistosomulae* migrate through the bloodstream to the lung where they develop into *Schistosomes*. *Schistosomes* re-enter the vascular system to reach the hepatoportal circulation where the parasite finally maturates into the adult worm[116]. Adult worms can persist in the settle in the mesenteric vessels of the intestine, for up to 10 years, sexually reproduce, and lay up to 300 eggs per day[117], which are distributed via the bloodstream. When eggs are released into a freshwater source within the faeces or urine of an infected mammalian host, the life cycle completes. Eggs, which are not excreted can be swept to organs, such as the liver. Because of their high immunogenicity, they cause the formation of granuloma, which in turn can result in fibrosis[118].

1.4.2 The immune response to *S. mansoni* infection

During the *S. mansoni* life cycle in the mammalian host, immune cells are exposed to various highly antigenic molecules initiating humoral and cellular immune responses. During the acute phase of the disease migrating *Schistosomula* cause a pro-inflammatory type 1 response. Hereby, the release of pro-inflammatory cytokines such as TNF-α, IL-1, and IL-6 causes inflammation and in consequence the symptoms of acute intestinal schistosomiasis described above[119]. The acute phase of the infection ends after around 6 weeks and turns into the chronic stage of the disease when the adult worms start to release eggs. Soluble egg antigen (SEA) from these eggs, triggers a decrease in IFN-γ production, and Th2 cell polarisation, which is accompanied by the release of cytokines such as IL-4, IL-5, IL-10, and IL-13. The Th2-mediated immune response peaks at about 8 weeks post infection (p.i.). Hereby, the switch from a type 1- towards a type 2-dominated immune response is essential for the host's survival. After about 8 weeks of infection, there is a decline in the type 2 response, accompanied by a rising signature of a regulatory T cell response allowing the parasitic worms to continue to produce eggs and to persist for years[120] (Figure 3).

Secretion of alpha-1 from the parasite eggs causes the release of IL-4 and IL-13 by basophils[121,122], which allows initiation of the type 2 polarisation. The IL-4/IL-13 enriched environment is driving the formation of granuloma around tissue-trapped eggs. Granuloma formation on the one hand protects the tissue from excessive damage, on the other hand it is detrimental to the host, as it in consequence

allows the onset of fibrosis. Granuloma formation starts with the accumulation of mononuclear cells, neutrophils and eosinophils forming a microabscess. With the infiltration of Mϕs and epithelioid cells, and the accumulation of fibroblasts around the immune cells, the microabscess matures into a granuloma[123]. In hepatic granuloma, the damage of hepatocytes resulting in the release of DAMPs activates hepatic stellate cells (HSCs) towards myofibroblast differentiation to express alpha-smooth muscle actin (α-SMA) and produce collagen, fibrogenic cytokines, matrix metalloproteinases (MMPs) and tissue inhibitors of metalloproteinases (TIMPs) that contribute to the remodelling of fibrotic tissue[124,125]. In the intestine parasite eggs, trapped within the granuloma, can translocate into the intestinal lumen, and consequently be excreted through the faeces. Conversely, in hepatic granuloma parasitic eggs are kept trapped leading to degeneration and disintegration of the surrounding tissue, which in the long run can cause fibrosis[118].

Hypoxia and toxic substances released by the eggs induce apoptosis to multiple cell types within the granuloma. The SEA specifically induces apoptosis in T cells, B cells and HSCs[121]. IL-13 released by accumulating Th2 cells in the granuloma and the phagocytosis of apoptotic cells strongly contribute to the polarisation of infiltrating Mϕs towards an anti-inflammatory state[126]. Anti-inflammatory Mϕs contribute to collagen synthesis and fibrogenesis via ARG1 providing proline for collagen synthesis and RELMα stimulating myofibroblast differentiation[127,128].

Importantly, in schistosomiasis, the recruitment of monocytes is the major process supporting the expansion of the Mϕ population within the liver, even though both monocyte-derived Mϕs and liver resident Mϕs engaged in the response to infection. Ly6C^{high} monocytes are recruited to the liver in a CCR2-dependent manner where they differentiate into Mϕs, thus restoring a population of CD11c^{high} hepatic Mϕs exerting anti-inflammatory properties[129,130]. In consequence, the polarisation of Mϕs towards an anti-inflammatory phenotype is essential to protect the host from an exaggerated Th1-mediated response, but at the same time is detrimental due to their contribution to the development of fibrosis. Therefore, the development of tools to balance between type 1 and type 2 responses may be necessary to prevent severe pathology.

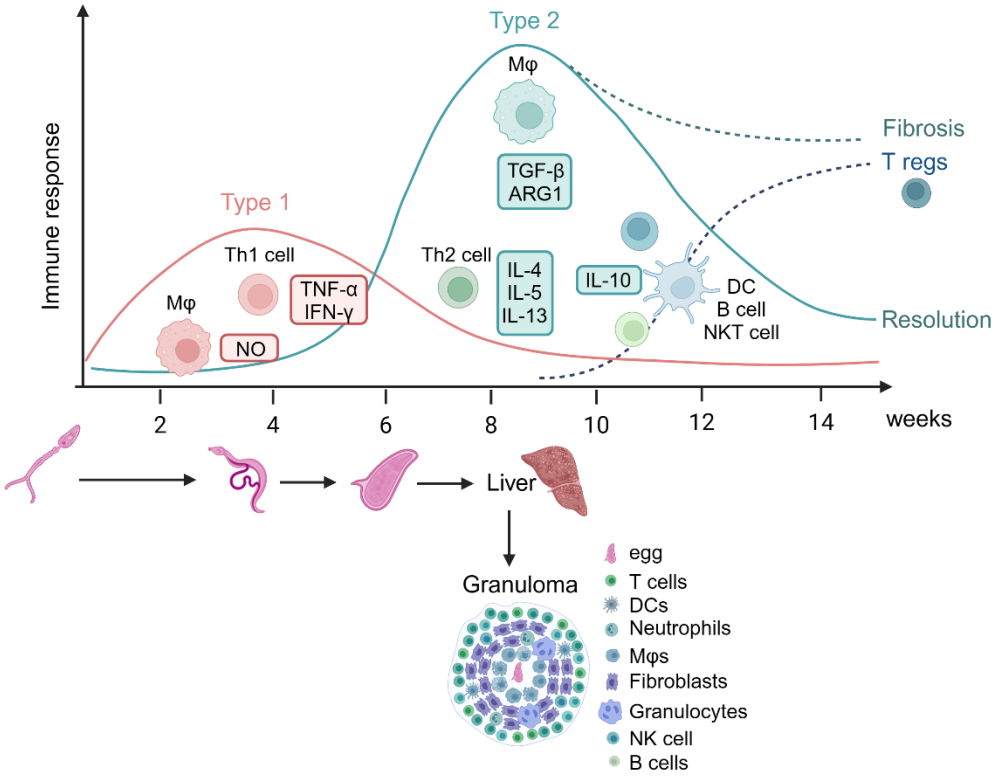


Figure 3: Schematic overview of the immune response during schistosomiasis. During the acute phase of the disease migrating *Schistosomula* trigger a type 1 dominant immune response characterised by NO-producing pro-inflammatory Mϕs and Th1 cells producing TNF-α and IFN- γ. Immunogenic parasite eggs cause a switch toward a type 2 immune response characterised by the development of granuloma and anti-inflammatory Mϕs producing TGF-ß and ARG1 in order to induce tissue remodelling. In untreated disease, a sustained type 2 response results in the accumulation of fibrotic tissue which is accompanied by an increase in the regulatory T cell response that allows parasite persistence.

1.4.3 EVs in schistosomiasis

During the course of schistosomiasis, EVs can be released by the parasite, the eggs and the host contributing to pathogen-host interaction. Circulating EVs in the infected host have been found to contain schistosomal proteins, and microRNA (miRNA) potent to modulate the immune response, for example, as an agonist for eosinophilic tissue repair[131] or as an inducer of T helper cell differentiation via an APC-dependent manner[132]. MiRNAs are short non-coding RNAs that can contribute to the quantitative regulation of gene expression and are of high abundance EVs released during schistosomiasis infection[133,134].

Parasite-derived EVs from adult *S. japonicum* worms have been shown to induce pro-inflammatory Mϕ activation *in vitro* by inducing the expression of iNOS and TNF-α[135]. In particular, a helminth-specific *bantam* miRNA and miRNA-125b have been described to induce Mϕ proliferation and TNF-α

production causing polarisation towards a pro-inflammatory phenotype[136]. EVs released by tissue-trapped eggs in the liver of infected mice have been found to contain miRNA-33, which promotes liver fibrosis via the upregulation of α-SMA and collagen 1 in HSCs[137]. In contrast, miRNA-71a contained in EVs released by *S. japonicum* eggs has been reported to suppress liver fibrosis by targeting semaphorin 4D causing inhibition of TGF-β and IL-13 pathways in HSCs[138,139].

SEA induces EV release from Mϕs containing miRNA-33, which targets SOCS3 signalling in HSC promoting their activation and the development of liver fibrosis[140]. During *S. japonicum* infection, EVs released in the liver of infected mice contain miRNA-142a-3p, which has been shown to induce the formation of neutrophil extracellular traps (NETs) and thereby inhibit the development of the parasite. Even though, the parasite is able to counteract this effect via upregulation of IL-10 production by Mϕs subsequently inhibiting NET formation[141].

Whereas most studies focus on the effect of parasite-derived EVs on host cells, the impact of host-derived EVs, especially of EVs derived from apoptotic cells on the course of infection has been largely neglected. Nevertheless, the findings of these studies highlight the importance of revealing the role of host cell-derived EVs in the pathogenesis of the disease.

1.5 Aim

Extracellular vesicles are important and yet underestimated contributors to cellular communication in homeostatic and pathological conditions. When a cell undergoes apoptotic cell death increased amounts of EVs are released into the environment potentially influencing the surrounding Mϕs.

This study aims to characterise EVs that are released by apoptotic thymocytes (aT-EVs), to identify differences to EVs released by live thymocytes (liveT-EVs), and to investigate their immunomodulatory effects on Mϕs. Therefore, to evaluate the impact of EVs on Mϕ function, transcriptomic and phenotypical changes occurring in Mϕs upon uptake of EVs released from either live or apoptotic thymocytes were evaluated. Lastly, the direct effect of liveT- and aT-EVs on the disease pathology was investigated in the context of infection with the trematode parasite *S. mansoni*.

Additionally, to identify the exact source of the liver EVs, analysis of the surface markers of EVs released in the livers of *S. mansoni*-infected or naïve mice was performed. This analysis may help to dissect the contribution of different EV-secreting cell types on *S. mansoni* pathogenesis and might indicate EVs as potential modulators of the Mϕ response.

Altogether this study aimed to clarify whether and how EVs could be used to specifically target Mϕs guiding their polarisation and function and ultimately impacting the outcome of a disease.

1 Material and methods

1.1 Materials

1.1.1 Cell line

Table 1: List of eukaryotic cell lines used.

Name	Origin
WEHI-164	BNITM, Hamburg (Germany)

1.1.2 Mouse strains

Table 2: List of mouse strains used.

Name	Origin
C57BL/6	BNITM, Hamburg (Germany)

1.1.3 Parasites

S. mansoni Cercariae were purchased from helminGuard (Sülfeld, Germany).

1.1.4 Biological and chemical reagents

Table 3: List of biological and chemical reagents used for experiments.

Chemical	Manufacturer
Aqua bidest. (ddH_2O)	BNITM, Hamburg (Germany)
1 % aqueous uranyl acetate	Electron Microscopy Sciences, Hatfield (USA)
β-Mercaptholethanol	ThermoFisher Scientific, Waltham (USA)
BSA	Sigma Aldrich, St. Louis (USA)
Cannula, Sterican, 2 G, 14 G, 21 G	Braun, Melsungen (Germany)
Chloroform	Carl Roth, Karlsruhe (Germany)
Collagenase IV	Gibco, ThermoFisher Scientific, Waltham (USA)
Cytochalasin D	ThermoFisher Scientific, Waltham (USA)
Disinfectant Incidin liquid	Ecolab, Düsseldorf, Germany
DMEM	PAN-Biotech GmbH, Aidenbach (Germany)
DMSO	Carl Roth, Karlsruhe (Germany)
DNase I	ThermoFisher Scientific, Waltham (USA)
DNase I (RNase-free)	Qiagen, Hilden, (Germany)
DPBS	Capricorn Scientific, Ebsdorfergrund (Germany)
Ethanol	Carl Roth, Karlsruhe (Germany)
FCS	Capricorn Scientific, Ebsdorfergrund (Germany)
Formalin	Carl Roth, Karlsruhe (Germany)

Gentamycin [40 mg/mL]	Capricorn Scientific, Ebsdorfergrund (Germany)
Glutaraldehyde 25 %	Merck, Darmstadt (Germany)
Heparin	Rathiopharm, Ulm, Germany
Isopropanol	Carl Roth, Karlsruhe (Germany)
KOH	Carl Roth, Karlsruhe (Germany)
L-Glutamine	Capricorn Scientific, Ebsdorfergrund (Germany)
LPS [1 mg/mL]	Sigma Aldrich, St. Louis (USA)
Lugol solution	Carl Roth, Karlsruhe, Germany
Megamix-Plus SSC beads	(Biocytex, Marseille, France).
RNAase away	Carl Roth, Karlsruhe (Germany)
RNase-free water	Fresenius, Graz (Austria)
RNAprotect Tissue Reagent	Qiagen, Hilden, (Germany)
Percoll	Sigma Aldrich, St. Louis (USA)
PFA	Carl Roth, Karlsruhe (Germany)
RPMI 1640, w/o: L-Glutamine, w: 2.0 g/L $NaHCO_3$	PAN-Biotech GmbH, Aidenbach (Germany)
Thioglycolate	Merck, Darmstadt (Germany)
Triton-x-100	Merck, Darmstadt (Germany)
Trizol	ThermoFisher Scientific, Waltham (USA)
Trypan Blue	Sigma Aldrich, St. Louis (USA)

1.1.5 Buffers, solution, and media

Table 4: Recipes for buffers, solutions and media used during experiments.

Buffer, solution, media	Recipe
Blocking buffer	0.5 µm anti-CD16/32 in 50 mL DPBS
EV medium	RPMI 1640 5 % FCS 1 % L-Glutamine 0.5 % Gentamycin → EV depleted at 100,000 xg for 16 h at 4 °C → 0.02 µm sterile filtered
EV PBS	DPBS → 0.02 µm sterile filtered
Complete medium for Mϕ differentiation	RPMI 1640 10 % FCS 15 % L929 sup. 1 % L-Glutamine 0.5 % Gentamycin → stored at 4 °C
FACS buffer	2 % FCS in PBS → stored at 4 °C
Fibroblast medium/	RPMI 1640 10 % FCS

Stopping medium	0.05 % Genta 1 % L-Glutamine
Liver digestion medium	DMEM 1mg/mL Collagenase IV 1 % MgCl2 (0.2 M) 0.4 % CaCl2 (0.5 M) 0.5 % DNase I (150 U/mL)
TEM incubating solution	0.5 % BSA in PBS

1.1.6 Dyes and antibodies

Table 5: List of used antibodies and dyes.

Epitope/Antibody	Fluorochrome	Clone	Amount/ Dilution	Manufacturer
a-goat IgG	FITC	CHXGO	1:200	Invitrogen, Carlsbad (USA)
Annexin V	FITC	/	1 µL	Biolegend, San Diego (USA)
a-rabbit IgG	BV510	Poly4064	1:200	Biolegend, San Diego (USA)
Arg1	APC	AlexF5	1:500	Invitrogen, Carlsbad (USA)
B220	PE-Cy5	RA3-6B2	1:300	BD Bioscience, Heidelberg (Germany)
CD3	PE BUV395	17A2 145-2C11	1 µL 1:200	Biolegend, San Diego (USA) BD Bioscience, Heidelberg (Germany)
CD4	PE	RM4	1 µL	Biolegend, San Diego (USA)
CD8	PE	53-6.7	1 µL	Biolegend, San Diego (USA)
CD9	PE-Dazzle	MZB	1 µL	Biolegend, San Diego (USA)
CD11b	PE APC-Cy7	M1/70	1 µL 1:400	Biolegend, San Diego (USA)
CD11c	PE	N418	1 µL	Biolegend, San Diego (USA)
CD36	PE-Cy7	HM346	1:500	Biolegend, San Diego (USA)
CD44	PE	1M7	1 µL	Biolegend, San Diego (USA)
CD45	APC	30-F11	1 µL/ 1:500	Biolegend, San Diego (USA)
CD49b	PE	Dx5	1 µL	Biolegend, San Diego (USA)
CD64	BV605	X54-5/7.1	1:300	Biolegend, San Diego (USA)
CD80	PE-Dazzle594	16-10AI	1:600	Biolegend, San Diego (USA)
CD86	Pacific Blue	GL-1	1:300	Biolegend, San Diego (USA)
CD163	BV421 APC-Fire810	S150491	1:200 1:200	Biolegend, San Diego (USA)
CD206	PerCP-Cy5.5	CO68C2	1:600	Biolegend, San Diego (USA)
Cleaved sapase-3	AF647	D3E9	1 µL	Cell Signaling Technology, Danvers (USA)
F4/80	AF700	BM8	1:400	Biolegend, San Diego (USA)
iNOS	eFluor450	LXNFT	1:250	Invitrogen, Carlsbad (USA)

Ly6C	PerCP-Cy5.5	HK1.4	1:300	Biolegend, San Diego (USA)
Ly6G	BV421	1A8	1:500	Biolegend, San Diego (USA)
MERTK	PE	12310C42	1:300	Biolegend, San Diego (USA)
MHC-I	PE BV510	SF1-1.1.1	1 µL	eBioscience, Frankfurt am Main (Germany)
MHC-II	PE PerCP	M51114.15.2	1 µL	eBioscience, Frankfurt am Main (Germany)
Proprium Iodide Solution	/	/	0.5 µL	Biolegend, San Diego (USA)
RELMα	/	K0118	1:200	Peprotech, Hamburg (Germany)
SiglecF	BV421	S17007L	1:300	Biolegend, San Diego (USA)
TIM4	AF647	RMT4-54	1:600	Biolegend, San Diego (USA)
a-mCh13L3 (Ym1)	/	ECF-L	1:200	R&D Systems, Minneapolis (USA)

1.1.7 Primers

All primers were designed using Primer Blast (NCBI) and purchased at Eurofins Genomics (Luxemburg, Luxemburg).

Table 6: List of Primer sequences.

Gene	Sequence (5' → 3')
mCol1	Fwd: GGTATGCTTGATCTGTATCTG Rev: AGTCCAGTTCTTCATTGCATT
mFn1	Fwd: GATGTCCGAACAGCTATTTACCA Rev: CCTTGCGACTTCAGCCACT
mGapdh	Fwd: TCCCACTCTTCCACCTTCGA Rev: AGTTGGGATAGGGCCTCTCTT
mNos2	Fwd: ACCCACATCTGGCAGAATGAG Rev: AGCCATGACCTTTCGCATTAG
mSerpinb2	Fwd: ACCCAGAGAACTTCAGTGGCTG Rev: GAGAGAGGAGAAGGCTGAATGG
mSocs2	Fwd: GGTTGCCGGAGGAACAGTC Rev: GAGCCTCTTTTAATTTCTCTTTGGC
mSocs5	Fwd: GACGGCTTAGTATCGAAGAA Rev: GCTTATACAATGGGTTGACC
mTimp1	Fwd: GCATCTCTGGCATCTGGCATC Rev: GCGGTTCTGGGACTTGTGGGC

1.1.8 Commercial kits

Table 7: List of used commercial kits.

Kit	Manufacturer
Reflotron GPT (ALT)	Roche, Basel (Switzerland)
Apoptosis detection Kit	Biolegend, San Diego (USA)
BD Perm/Wash™ Perm/Wash Buffer	BD Bioscience, Heidelberg (Germany)
iScript™ cDNA Synthesis Kit	Bio-Rad, Feldkirchen (Germany)
Vybrant™ CFDA SE Cell Tracer Kit	ThermoFisher Scientific, Waltham (USA)
eBioscience™ Foxp3 / Transcription Factor Fixation/Permeabilization Concentrate and Diluent	Invitrogen, ThermoFisher Scientific, Waltham (USA)
eBioscience™ Cell Proliferation Dye eFluor™ 450	ThermoFisher Scientific, Waltham (USA)
LEGENDplex™ MU Th1/Th2 Panel (8-plex) w/ FP V03	Biolegend, San Diego (USA)
MACSPlex EV Kit IO, mouse	Miltenyi Biotec, Bergisch Gladbach (Germany)
miRNeasy Mini Kit (50)	Qiagen, Venlo (Netherlands)
Nitric Oxide Assay Kit	ThermoFisher Scientific, Waltham (USA)
RNeasy Mini Kit	Qiagen, Venlo (Netherlands)
Maxima SYBR Green/ROX qPCR Master Mix	ThermoFisher Scientific, Waltham (USA)
Qubit™ Protein Assay Kit	Invitrogen, ThermoFisher Scientific, Waltham (USA)

1.1.9 Consumable materials

Table 8: List of used consumable materials.

Material	Manufacturer
Compensation beads	Invitrogen, Carlsbad (USA)
Disposable gloves	Kimtech, Koblenz-Reinhafen (Germany)
Disposable pipettes (5 mL, 10 mL, 25 mL)	Braun, Melsungen (Germany)
FACS tubes	Sarstedt, Nümbrecht (Germany)
Falcon™ conical centrifuge tubes 15 mL, 50 mL	ThermoFisher Scientific, Waltham (USA)
Filtropur 0.2 um	Sarstedt, Nümbrecht (Germany)
Glass bottles	Schott AG, Mainz (Germany)
Glass pipettes (2 mL, 5 mL, 10 mL, 20 mL)	Brand GmbH, Wertheim (Germany)
Glass slides	Engelbrecht, Edermünde (Germany)
Microlon® 96 well microplate, PS, F-bottom, clear, high binding	Greiner Bio-One, Kremsmünster (Austria)
Millipore Stericup™ sterile vacuum filter	Merck, Darmstadt (Germany)
Neubauer counting chamber	Marienfeld, Lauda-Königshofen (Germany)
Nunc CryoTube™ vials	ThermoFisher Scientific, Waltham (USA)

Omnifix, Omnican Syringes	Braun, Melsungen (Germany)
Petri dish 92x16 mm with cams	Sarstedt, Nümbrecht (Germany)
Pipette tips	Sarstedt, Nümbrecht (Germany)
Pluristrainer	pluriSelect Life Science, Leipzig (Germany)
Polyallomer centrifuge tubes (14 x 95 mm and 25 x 89 mm)	Beckman Coulter, Krefeld (Germany)
Reaction tubes 0.5 mL, 1.5 mL, 5 mL, 15 mL, 50 mL	Sarstedt, Nümbrecht (Germany)
Safe-Lock Tube PCR clean (RNA-free) 0.5 mL, 1.5 mL, 2 mL	Eppendorf, Hamburg (Germany)
Syringe 20 mL, 10 mL, 5, mL, 2, mL	Braun, Melsungen (Germany)
Syringe sterile filter 0.2 µm	Merck, Darmstadt (Germany)
TC Plate 24 well, standard, F	Sarstedt, Nümbrecht (Germany)
Tissue culture coverslips 13 mm	Sarstedt, Nümbrecht (Germany)

1.1.10 Laboratory equipment

Table 9: List of used equipment and devices.

Device	**Manufacturer**
Bioanalyzer System Agilent 2100	Agilent Technologies, Santa Clara (USA)
Centrifuge 5417R/5415R/5810R	Eppendorf, Hamburg (Germany)
CO_2 Incubator Hera Cell 150	ThermoFisher Scientific, Waltham (USA)
CO_2 Incubator Function Line BB16	Heraeus Instruments, Hanau (Germany)
Cytek Aurora™	Cytek Biosciences, Fremont (USA)
FACSAria™ III	BD Bioscience, Heidelberg (Germany)
Flow cytometer Accuri™ C6	BD Bioscience, Heidelberg (Germany)
Flow cytometer LSR II	BD Bioscience, Heidelberg (Germany)
Freezers -20 °C/-80 °C	Liebherr, Bieberach (Germany)
Microbiological Safety Cabinet B-[MaxPro]^3-130	Berner International GmbH, Elmshorn (Germany)
Labculture® Class II Biological Safety Cabinet	ESCO, Singapore (Singapore)
Mr. Frosty™ freezing device	Zefa Laborservice, Harthausen (Germany)
MRX Microplate Reader ELISA	Dynatech Laboratories, Berlin (Germany)
Optical microscope	Helmut Hund, Wetzlar (Germany)
EVOS FL Auto Imaging system	ThermoFisher Scientific, Waltham (USA)
Fluorescence Microscope BZ9000	Keyence, Neu-Isenburg (Germany)
Multichannel pipettes	Eppendorf, Hamburg (Germany)
Nanodrop2000	ThermoFisher Scientific, Waltham (USA)
Nanosight LM14C	Malvern panalytical, Amesbury (UK)
Optima XE-90 Ultracentrifuge	Beckman Coulter, Krefeld (Germany)
Pipettes	Gilson, Middleton (USA) Eppendorf, Hamburg (Germany)
Pipetus	Hirschmann Laborgeräte, Eberstadt (Germany)

Pipetboy	Integra Biosciences, Biebertal (Germany)
Tissue Homogenizer KIMBLE® PELLET PESTLE®	DWK Life Scieces, Wertheim (Germany)
Reflotron® plus	Roche, Basel (Switzerland)
Refrigerators (4 °C)	Liebherr, Biberach (Germany)
Tecnai™ Spirit Transmission electron microscope	FEI company, Hillsboro (USA)
Vortexer V-1 plus	Kisker Biotech, Steinfurt (Germany)
Vortexer VF2	IKA®, Staufen (Germany)
Water bath Lauda alpha ET6	Lauda, Lauda-Königshofen (Germany)

1.1.11 Software

Table 10: List of software, programs and databases used for data acquisition and analyses, writing, literature research, and citation.

Software, program, database	Source
Agilent 2100 Expert Software	Agilent Technologies, Santa Clara (USA)
BD FACSDiva™ 6.2	BD Biosciences, Heidelberg (Germany)
LEGENDplex™ Data Analysis Software Suite	Biolegend, San Diego (USA)
BioRender	Biorender AG, Münchwilen Thurgau (Germany)
FlowJo V10	BD Biosciences, Heidelberg (Germany)
GaphPad prism 9.5.1.	GraphPad Software Inc, San Diego (USA)
ImageJ	Schneider, C. A., Rasband, W. S., & Eliceiri, K. W. (2012). NIH Image to ImageJ: 25 years of image analysis. Nature Methods, 9(7), 671–675.
Inkscape 1.2.2	Open Source Scalable Vector Graphics Editor
Mendeley 1.19.4	Mendeley, London (UK)
Microsoft Office	Microsoft Corporation, Redmon (USA)
PubMed	National Center for Biotechnology Information, U.S. National Library of Medicine, Bathesda (USA)

1.2 Methods

1.2.1 Cell culture

Cells were cultured at 37 °C and 5 % CO_2. All cell cultures and *in vitro* experiments were handled under sterile conditions.

1.2.2 Cell count

For cell count determination cells were diluted with Trypan Blue solution, a dye allowing live/dead discrimination by entering dead cells with porous membranes. 10 µL of the cell dilution were added to a Neubauer counting chamber. Living cells in four large squares were counted under the transmission light microscope. For counting of apoptotic cells, cells were counted in PBS instead of Trypan Blue. The concentration of the cell suspension was calculated using the following formula:

$$\frac{Cells}{mL} = \frac{Total\ cell\ count}{4}\ x\ 10^4\ x\ dilution\ factor$$

1.2.3 Bone marrow-derived Mϕs

Bone marrow was isolated from the femur and tibia of the mice by cutting one bone end and placing bones with the open end facing down into a 0.5 mL tube with a pinched hole placed in a 1.5 mL tube followed by centrifugation at 16,000 xg for 2 min. The isolated bone marrow was resuspended in 200 µL RPMI, filtered through a 40 µm cell strainer and washed with 10 mL RPMI. Cells were pelleted at 300 xg for 5 min and seeded into a petri dish in 10 mL complete medium for Mϕ differentiation. Bone marrow-derived Mϕs (BMDMs) were differentiated over a time course of seven days. On day 3, 5 mL medium were removed, and centrifuged at 300 xg for 5 min. The pelleted cells were resuspended in 5 mL fresh complete medium for Mϕ differentiation and transferred back to the petri dish. On day 5, cells were detached on ice with ice-cold PBS and extensive pipetting. Detached cells were washed at 300 xg for 5 min and 4 °C and resuspended in 20 mL fresh complete medium for Mϕ differentiation and evenly split into two petri dishes. On day 7 differentiated BMDMs were harvested, counted, and 0.33 x 10^6 cells per well were seeded into a 24-well plate in 500 – 1000 µL fresh complete medium for Mϕ differentiation to perform *in vitro* experiments.

1.2.4 Isolation of thymocytes and induction of apoptosis

Thymuses were isolated from naïve mice and mashed through a 40 µm cell strainer using a syringe plunger and PBS to generate a single-cell suspension. Cells were pelleted at 300 xg for 5 min and 4 °C, resuspended in 10 mL apoptosis medium and plated in a petri dish. Apoptosis medium contains only 5 % FCS, leading to starvation of the thymocytes causing induction of apoptosis over time. Thymocytes were cultivated at 37 °C and 5 % CO_2. After 1 – 3 h cells and supernatant were transferred to a 15 mL falcon and centrifuged at 300 xg for 5 min. The supernatant was saved for EV Isolation from live thymocytes, an aliquot (~10 µL) of the cells was taken for detection of apoptosis rate and the remaining cells were resuspended in 10 mL fresh apoptosis medium, transferred back into the petri dish and further cultivated at 37 °C and 5 % CO_2. The procedure was repeated after 24 h to obtain supernatant from apoptotic thymocytes for EV isolation and/or cells for apoptosis detection and *in vitro* experiments.

1.2.5 Determination of apoptosis rates

10 µL of cell suspension were transferred into a FACS tube containing 100 µL of Annexin V binding buffer. 1 µL Annexin V was added to stain the Phosphatidylserine on the surface of the apoptotic cells. After 15 min incubation at RT in the dark, 100 µL Annexin V binding buffer and 0.5 µL PI were added and samples were immediately measured at the LSR II.

1.2.6 Isolation of EVs from thymocytes

Supernatant from live or apoptotic thymocytes was generated as described in 1.2.5. Extracellular vesicles were isolated from the supernatant by differential centrifugation. Therefore, the supernatant was first cleared from cells and debris by centrifugation at 2 x 300 xg for 5 min and 2 x 2000 xg for 20 min, transferring the supernatant into a new 15 mL Falcon tube after each step. All centrifugation steps were performed at 4 °C. Afterward supernatant was transferred into ultracentrifugation tubes and ultracentrifuged at 16,000 xg for 45 min. The pellet containing larger EVs was resuspended in EV-PBS and washed repeatedly at 16,000 xg. The supernatant was transferred into a fresh UZ tube and centrifuged at 100,000 xg for 1 h. The pellet containing smaller EVs was resuspended in EV-PBS and washed again at 100,000 xg. Larger EV and smaller EV pellets were resuspended in various amounts of EV-PBS or other reagents depending on the following experimental uses.

1.2.7 NTA

EV size and concentration was measured with the Nanosight LM14C equipped with a CCD camera (Malvern panalytical) by nanoparticle tracking analysis (NTA). Initially, 500 µL of EV suspension were injected into the chamber and each sample was measured 5 times for a recording time of 30 sec. Between every measurement, 100 µL of fresh EV suspension were injected. During the measurement particles are illuminated by a laser beam and NTA technology allows quantification of the particle size distribution by the resulting light scattering and Brownian motion Settings were adjusted as stated in Table 11.

Table 11: List of NTA settings.

Parameter	Setting
Camera level	12
Screen Gain	10.00
Temperature control	25 °C

Raw data is processed by the NTA 3.0 software resulting in calculated averaged size and concentration of the EVs from the recorded video clips and plots the summary in a PDF file.

1.2.8 Protein concentration

Qubit™ protein assay kit (Invitrogen) was applied according to the manufacturer's instructions. In brief, the working solution was reconstituted by diluting 1 µL protein reagent in 199 µL protein buffer. 190 µL working solution were added to 10 µL of sample or standard in a Qubit tube, vortexed and protein concentration was measured with the Qubit 4 fluorometer.

1.2.9 TEM

A 50 µL aliquot of freshly isolated EVs was fixed with 5 % glutaraldehyde. Further preparation of the samples and visualisation of the EVs by transmission electron microscopy (TEM) was performed by Katharina Höhn (BNITM Hamburg, Germany). Grids were observed under a Tecnai Spirit electron microscope operating at 80 kV and images were recorded with a digital CCD camera.

1.2.10 CFSE-labelling of EVs

Vybrant™ CFDA SE Cell Tracer Kit (ThermoFisher Scientific) was applied to label EVs. The manufacturer's instructions were optimized for application in EV research as follow. 0.33 µL CFDA-SE (10 mM) were diluted in 1000 µL EV-PBS. 1 mL EV suspension was added to the CFSE mixture, vortexed

and incubated at 37 °C in the dark for 2 h. 10 mL EV medium were added and EVs were pelleted at 16,000 or 100,000 xg, respectively.

1.2.11 EV uptake assay *in vitro*

BMDMs were plated in 24-well plates on d7 as described in 1.2.5. EVs were given in a concentration 5 – 10 µg of determined protein concentration (1.2.8.) per well or 1000 EVs per Mϕ (0.33 x 10^9 per well) if samples were measured by NTA before the experiment. Determined amounts of EV were added to the seeded BMDMs and co-cultured for 1 – 24 h depending on the experiment. To block the uptake of EVs Mϕs were treated with Cytochalasin D (10 µg/mL) 1 h prior to co-incubation with EVs. Before harvesting every well was washed 3 x with PBS. Then the cells were harvested depending on the following processing of the cells. For flow cytometry cells were detached on ice using cold PBS, and washed at 300 xg for 5 min at 4 °C. For RNA Isolation cells were directly in the plate lysed in Trizol or Buffer RLT as reported in 1.2.14.

1.2.12 Phagocytosis assay

To study the influence of T-EVs on the phagocytic capacity on Mϕs, BMDMs were seeded in 24-well plates as described in 1.2.5 and co-cultured with EVs as described in 1.2.11. In the meantime, apoptotic thymocytes were labelled with eBioscience™ Cell Proliferation Dye eFluor™ 450. Therefore, 1 µL of dye in 1 mL PBS was added to 1 mL of aTs and incubated for 15 min at 37 °C in the dark. Subsequently, 5 mL of Stopping medium containing 10 % FCS were added and incubated on ice for 5 min. The stained cells were washed with 5 mL media at 300 xg for 5 min at 4 °C. Washing steps were repeated 2 times. After 1 h of co-incubation with T-EVs 1.65 x 10^6 apoptotic thymocytes were added to the Mϕs. After 45 min Mϕs were harvested for flow cytometric analysis of the uptake rates described in 1.2.13.

1.2.13 Fibroblast migration assay

To perform a fibroblast migration assay, WEHI-164 cells were harvested, counted, and 0.2 x 10^6 cells per well were seeded into a 24-well plate in 1000 µL fibroblast medium. When cells were settled, the medium was removed and using a 200 µL pipette tip (Sartstedt) two scratches were made disrupting the fibroblast monolayer from left to right in the upper and lower half of each well. The wells were gently washed with PBS to remove the detached fibroblasts from the scratches. 200 µL of supernatant collected from the EV uptake assay (1.2.11) were added and each well was photographed with the EVOS FL Auto Imaging system (ThermoFisher Scientific). All photographed positions were saved and after 24 h incubation at 37 °C and 5 % CO_2, pictures were taken again. To determine the effect of the

supernatants from differently treated Mϕs, the calculation of the gap closure was performed using ImageJ. In brief, picking three positions per scratch, the diameter of the scratch separating the fibroblasts was measured in the pictures taken at 0 h and 24 h of cultivation. The average diameter for each time point was calculated and gap closure was calculated using the following formula:

$$gap\ closure\ [\%] = 1 - \frac{average\ (24\ h)}{average\ (0\ h)}\ x\ 100$$

1.2.14 Flow cytometry

Flow cytometry is a useful tool to detect single particles and characterise them by the way they scatter light. The measurement of forward scatter (FSC) allows discrimination of the cells by size, while the measurement of side scatter (SSC) provides information about the internal complexity, also referred to as granularity, of a cell. Antigens on the particle's surface or inside can be detected using flow cytometry by prior intra- or extracellular staining with fluorochrome-labelled antibodies against the epitopes of interest. Flow cytometry was applied to measure and analyse physical characteristics, namely size, granularity, and antigen expression of cells and EVs. To investigate the presence of specific antigens on the surface and inside cells and EVs, they were stained with fluorochrome-labelled antibodies (listed in Table 5). During sample acquisition, suspended particles are transported through a fluidic system to the laser intercept, where they pass through laser beams. Light scattering and fluorescence emission of single particles are recorded, providing information about the size, granularity, and antigen expression of the measured particles. Samples were acquired at LSR II or Cytek Aurora™. Data acquisition was performed in BD FACSDiva™ 6.2 of Spectoflow, respectively, and the acquired data was analysed using FlowJo V10.

1.2.14.1 Staining of EVs for flow cytometry

For surface staining of EVs, 1 µL Antibody (listed in Table 5) was diluted in 50 µL EV PBS and added to 50 µL of EV samples and incubated for 1 h at RT in the dark. For staining with Annexin V, EVs were diluted in 0.2 µm filtered Annexin V binding buffer (Biolegend, San Diego, USA).

For intravesicular staining, EVs were permebilised in 0.1 % BD Perm/Wash™ Perm/Wash Buffer (BD Bioscience, Heidelberg, Germany). After incubation for 40 min at RT in the dark, 50 µL of cleaved caspase-3 antibody diluted in 0.1 % BD Perm/Wash™ were added and incubated for 1.5 h at RT protected from light. After incubation 200 µL of the according buffer were added to each sample and samples were divided into two FACS tubes each. One was measured directly at the Cytek Aurora™, with the settings described above, whereas the other one was incubated with 0.1 % Triton-x100 as a detergent control and measured after 30 min of incubation.

1.2.14.2 Staining of cells for flow cytometry

Harvested cells, were transferred to a 96-well round bottom plate in 200 µL blocking buffer and incubated for 15 min at 4 °C. Afterwards cells were washed with FACS buffer 2 times at 800 xg for 3 min at 4 °C. A mix of Fluorochrome-labelled antibodies against surface epitopes (listed in Table 5) was prepared diluting the antibodies in previously titrated concentrations in 25 µL FACS buffer per sample. Pellets were dissolved in 25 µL of the master mix each and incubated for 45 min at 4 °C protected from light. Cells were washed twice with 150 µL FACS buffer at 800 xg for 3 min at 4 °C to remove unbound antibodies. For flow cytometric analysis the cells were suspended in 200 µL FACS buffer and acquired at Cytek Aurora™ or LSR II.

If intracellular epitopes were analysed, cells were fixed and permeabilised after extracellular staining. 100 µL of 1 % paraformaldehyde (PFA) were added to the wells and incubated for at least 20 min at 4 °C in the dark for fixation. Afterwards, 100 µL permeabilisation buffer (BD Bioscience) were added and incubated for 15 min at RT. Cells were washed twice with 150 µL perm buffer at 800 xg for 3 min at 4 °C. The intracellular antibodies were diluted in permeabilisation buffer in previously titrated concentrations and 25 µL of the intracellular master mix each and incubated for 45 min at 4 °C protected from light. Samples were washed twice before acquisition at Cytek Aurora™ or LSR II.

Cells isolated from the liver were fixed and permeabilised using the Foxp3 staining Kit (eBioscience) instead of PFA and permeabilisation buffer (BD Bioscience) according to the manufacturer's instructions.

1.2.15 MACSPlex for EV surface epitope detection

MACSPlex, which is a bead-based multiplex assay (Miltenyi Biotec) allowing the simultaneous detection of 37 surface epitopes (+2 Isotype controls) by flow cytometry. According to the manufacturer's instructions, 20 µg EVs or buffer control were resuspended in 200 µL MACSPlex buffer in 1.5 mL reaction tubes and 15 µL capture beads were added. After incubation overnight at RT on an orbital shaker protected from light, 500 µL MACSPlex buffer were added to each sample. Samples were washed at 3000 xg for 5 min at RT. The supernatant was aspirated and a mastermix of 5 µL per detection reagent was added to each sample and mixed by pipetting up and down. Samples were incubated for 1 h at RT on an orbital shaker protected from light. Samples were washed again with 500 µL MACplex buff, the pellet was resuspended in 500 µL MACSPlex buffer, and incubated for 15 min at RT on an orbital shaker protected from light. After a final step of centrifugation samples were resuspended in 200 µL MACplex buffer. Samples were acquired at the Accuri C6 and analysed using FlowJo V10.

1.2.16 RNA Isolation

1.2.16.1 RNA Isolation from EVs

For the isolation of miRNA from the EV samples, the miRNeasy Mini Kit (Qiagen) was used according to the manufacturer's instructions, which enables the purification of total RNA, including small RNA from 18 nt upwards. Briefly, EVs were resuspended in 700 µL QIAzol Lysis Reagent transferred to 1.5 mL reaction tubes and frozen at -80 °C until further processing. After thawing, 200 µL chloroform were added to each reaction tube. The reaction tubes were shaken for 30 sec, left at RT for 2 min and spun at 12,000 xg for 15 min at 4 °C. The upper aqueous phases were pooled into a new 15 mL reaction tube and the 1.5-fold volume of 100 % ethanol was added and mixed by inverting the reaction tube. 650 µL of the sample were loaded on a RNeasy Mini column and spun at 10,000 xg for 25 sec. The flow-through was discarded and the procedure was repeated until no sample remained. 700 µL of Buffer RWT were added to the column, spun at 10,000 xg for 25 sec and the flow through was discarded. Twice, 500 µL Buffer RPE were added to the column, and spun at 10,000 xg for 25 sec. The flow-through was discarded, and the column was spun to dry at 10,000 xg for 1 min. The column was transferred into a 1.5 mL reaction tube and 20 µL RNase-free water were placed directly on the membrane, incubated for 2 min at RT, and the miRNA was eluted at 10,000 xg for 1 min. The elution step was repeated once, and the final RNA content was measured by Nanodrop2000 (ThermoFisher Scientific). The miRNA samples were stored at -80 °C until further processing.

1.2.16.2 RNA Isolation from cells using Trizol

To obtain RNA from tissue stored in RNAprotect Tissue Reagent (Qiagen), a section of tissue was transferred into 200 µL TRIzol in a 1.5 mL Tube. Using a tissue homogeniser (KIMBLE® PELLET PESTLE®), the tissue was disrupted and 800 µL TRIzol were added and incubated for 5 min at RT. Afterwards, 200 µL chloroform were added, mixed for 15 sec and incubated for 3 min at RT. The samples were centrifuged at 12000 xg for 15 min at 4 °C. The aqueous phase (~500 µL) of the supernatant was carefully transferred into a new tube containing 500 µL isopropanol and incubated at RT for 10 min. The samples were centrifuged at 12000 xg for 15 min at 4 °C, the supernatant was discarded and 500 µL of 80 % EtOH were added. After mixing, the suspension was centrifuged for 5 min at 7500 xg at 4 °C, the supernatant was discarded, and the RNA was air-dried. The RNA was dissolved in 150 µL RNase-free water and the concentration and purity were measured via Nanodrop.

1.2.16.3 RNA Isolation from cells using RNeasy Mini Kit

RNA for sequencing and subsequent experiments was isolated using the RNeasy mini Kit (Qiagen) by following the manufacturer's instructions. In brief, cells were lysed by adding 350 µL RLT buffer

containing 3.5 µL β-Mercaptoethanol, loaded on QIAshredder column (Qiagen), and spun for 2 min at 15,000 xg. Samples were stored at -20 °C until further processing. 350 µL 70 % EtOH were added to the sample and loaded to the RNeasy mini column, spun at 10000 xg for 21 sec and the flow through was discarded. The column was washed with 700 µL of Buffer RW1, followed by DNase I digestion on the column for 15 min at RT. Again, buffer RW1 was added for washing, followed by two washing steps with 500 µL Buffer RPE for 2 min at 10000 xg. The column was transferred into a 1.5 mL reaction tube and 28 µL RNase-free water were placed directly on the membrane, incubated for 2 min at RT, and the RNA was eluted at 10,000 xg for 1 min. The RNA concentration and purity were measured by Nanodrop2000 (ThermoFisher Scientific). The RNA samples were stored at -80 °C until further processing.

1.2.17 cDNA Synthesis

cDNA Synthesis was performed using the iScript cDNA synthesis Kit (BioRad) as follows:

Table 12: cDNA synthesis Reaction-Mix.

Component	Amount
iScript Reverse Transcriptase	1 µL
5x iScript Reaction Mix	4 µL
RNA template	400 ng
RNase-free water	Ad to 20 µL

Table 13: cDNA synthesis thermocycler settings.

Step	Temperature	Time
Priming	25 °C	5 min
Reverse transcription	46 °C	20 min
RT inactivation	95 °C	1 min

1.2.18 Quantitative Real-Time PCR

Quantitative Real-Time polymerase chain reaction (RT-qPCR) was performed using the Maxima SYBR Green qPCR Master Mix (2X) (ThermoFisher Scientific). Hereby, SYBR Green intercalating in the amplified PCR product during the reaction is measured by the Rotor-Gene 6000. All reactions were performed in a final volume of 12 µL per reaction including 40 ng cDNA. Data were analysed using the Rotor-Gene 6000 Series Software 1.7. The primers that were used are listed in Table 6.

Table 14: qPCR Reaction-Mix.

Component	Amount
SYBR green Master Mix	6 µL
Nuclease-free water	4.7 µL
Primers	0.15 µL
RNA template	1 µL (40 ng)

Table 15: Rotor-Gene settings.

Step	Temperature	Time	Cycles
UDG pre-treatment	50 °C	2 min	
Initial denaturation	95 °C	10 min	
Denaturation	95 °C	15 sec	40 x
Annealing	60 °C	30 sec	
Extension	72 °C	30 sec	

1.2.19 Bulk-RNA Sequencing

RNA isolated from BMDMs treated with liveT-EVs or aT-EVs for 24 h was sent to BGI (BGI TECH SOLUTIONS, Hongkong) where RNA sequencing was performed. Library preparation and transcriptome sequencing were performed using 100 bases/paired-end reads on BGI's DNBSEQ Technology Platform. The mRNA sequencing with subsequent filtering (removal of adapters, low-quality reads, N reads and polyX) and quality control was performed on DNBSEQ Technology by BGI. The reads for each sample were aligned to the mouse genome (GRCm39) using STAR aligner (version 2.7.10b). The obtained sequencing data was kindly analysed by Christoph Kilian (UKE Hamburg) as follows: Only genes with at least $10^{1.5}$ raw counts in half of all samples were considered for analysis. Calculation of the fold change of each gene between liveT- and aT-EVs was performed using DESeq2 (version 1.40.2). The top 15 genes with the highest log2FC and 15 genes with the lowest log2FC were defined as the top differentially expressed (DE) genes. The row-scaled values of these genes were sorted by hierarchical clustering and plotted using the pheatmap package (version 1.0.12). To determine, which processes and pathways be targeted, all DE genes with log2FC > 0.5 as upregulated in liveT-EVs and log2FC < -0.5 as upregulated in aT-EVs were grouped. These genes were used to perform an overexpression analysis using the enrich KEGG method by the package clusterProfiler (version 4.8.3). The gene symbols were converted to Entrez IDs by org.Mm.es.db (version 3.17.0). The parents of each term were queried using KEGGREST (version 1.40.1). Further, 60 Biological Process 2023 were calculated by the enrichR method by enrichR package.

1.2.20 LEGENDplex™

To measure cytokine concentrations in the supernatants of the EV uptake assay *in vitro* the MU Th1/Th2 Panel (8-plex) w/ FP V03 LEGENDplex™ (BioLegend) was performed according to the manufacturer's instructions. The kit contains beads that are coated with antibodies against the cytokines of interest. These beads differ in size and intensity of the bound fluorochrome depending on their cytokine specificity in order to allow their separation by flow cytometry. The corresponding cytokines contained in the samples bind to the beads and the beads are detected by a second antibody linked to biotin, which is further detected by a streptavidin-bound PE. The concentration of the cytokines is then calculated from the fluorescence intensity using a standard curve for reference. The LEGENDplex™ was measured at the Accuri C6 and analysed with the LEGENDplex™ software Version 2023-02-15.

1.2.21 Nitric oxide assay

The nitric oxide assay Kit (Thermo Fischer Scientific) was applied according to the manufacturer's instructions to determine the nitrate concentration in the supernatants of the EV uptake assay. In brief, 25 µL of supernatant are transferred to a 96-well plate and diluted 1:3 with Assay buffer. The enzyme nitrate reductase is added to convert nitrate to nitrite and samples are incubated for 30 min at 37 °C. Griess solutions I and II are added allowing the detection of Nitrite as a coloured azo dye product of the Griess reaction at 540 nm (+/- 20 nm). Absorbance was read at 560 nm at the MRX Microplate Reader. Cytokine concentrations were calculated from a standard curve, generated from the absorbance reading of the standard's serial dilutions.

1.2.22 Mice

All animal experiments were approved by the Office for Consumer Protection of the city of Hamburg (N105/2021 and 2021_T001). Mice were bred and kept in an SPF facility at the BNITM.

1.2.23 Organ harvesting

The mice were sacrificed by application of CO_2/O_2. To ensure sufficient anaesthesia, cornea and foot reflexes were checked twice and death was ensured by cervical dislocation. The harvested organs were collected and stored in PBS/2 % FCS, in RNAprotect Tissue Reagent (Qiagen) for RNA analysis or Formalin for histology.

1.2.24 Thioglycolate-induced peritonitis

To induce inflammation in the peritoneum, mice were injected with 2 times 250 µL 4 % Thioglycolate (on the left and right side of the peritoneum). 24 h or 48 h after Thioglycolate injection, depending on the experiment, 1 x 10^9 CFSE-labelled T-EVs in 200 µL EV PBS were injected into the peritoneum. To investigate the impact of T-EVs on the phagocytic capacity of peritoneal Mϕs, 3 x 10^6 eFluo450-labelled aTs in 200 µL PBS were injected per mouse 3 h later. At the end of the experiment, mice were sacrificed with CO_2/O_2 following cervical dislocation and peritoneal cells were isolated. To this end, 5 mL PBS/2 % FCS was injected into the intact peritoneum and the peritoneum was massaged for 60 sec to detach the Mϕs. Without puncturing the organs, the fluid was reobtained with a syringe. Cells were pelleted at 300 xg for 5 min at 4 °C, lysis of red blood cells was performed, and cells were washed with PBS/2 % FCS and further processed for flow cytometric analysis.

1.2.25 *S. mansoni* infection

S. mansoni Cercariae (helminGuard) were counted in a 48-well plate with a grid under the microscope. Therefore, an aliquot of *Cercariae* was immobilised by adding 1 mL Lugol solution. 20 – 35 *S. mansoni* cercariae (1: 1.2 male to female ratio) diluted in 200 µL ddH2O were injected s.c. in 6–10-week-old C57BL/6 mice. After sacrificing the mice at week 8 p.i. the liver and blood were collected as described above. A piece of the right renal fossa loop of the liver was stored in RNAprotect Tissue Reagent (Qiagen, Hilden, Germany). For histological staining, liver samples (right loop) were fixed in formaldehyde overnight and subsequently stored in PBS until further processing.

1.2.26 EV transfer in *S-mansoni*-infected mice

Live-T-EVs and aT-EVs were isolated as described above. 5 x 10^9 EVs in 200 µL EV PBS were injected i.v. in the lateral tail vein of *S. mansoni*-infected mice at week 6 and 7 p.i. Control mice were injected with 200 µL EV PBS. Mice were sacrificed at week 8 p.i. and liver and blood were harvested for further investigations.

1.2.27 ALT levels

Blood from *S. mansoni*-infected mice was collected in tubes containing 20 µL heparin, centrifuged and the serum stored at −20 °C. The levels of alanine aminotransaminase (ALT) in the serum were then quantified via Reflotron (Roche, Basel, Switzerland). Measurements were performed at 25°C, using 32 µL of serum per mouse.

1.2.28 Egg count

To determine the egg count in the livers of *S. mansoni*-infected mice, a piece of the left loop of the liver was weighed and incubated in 2 % KOH for 8 h at 37 °C in a 24-well plate with a grid. The tissue was further disrupted by pipetting up and down from time to time. When tissue was completely dissolved the eggs were counted on a bright field microscope using 4 x magnification and eggs per gram liver were calculated.

1.2.29 Histology

Liver tissue was fixed in 37 % Formalin for 24 h followed by storage in PBS. Samples were processed, embedded, sectioned, and stained for Picrosirius Red at the Core Facility Mouse Pathology (University Medical Center Hamburg Eppendorf) following routine methods.

1.2.30 Isolation of cells from liver

After sacrificing and cervical dislocation of the mice, livers were perfused by inserting Venofix 27 G (Braun) in the *vena cava* and rinsing with 20 mL PBS through an attached syringe. The liver was collected and stored in 2 mL PBS/2 % FCS on ice. The gallbladder was removed, and the liver minced into small pieces in a petri dish. Liver pieces were transferred into a 50 mL Falcon containing 10 mL digestion media and the suspension was incubated for 45 min at 37 °C while shaking. The digested suspension was mashed through a 70 µm cell strainer using a syringe plunger and PBS/2 % FCS to obtain a single-cell suspension. The liver cell suspensions were washed at least twice at 300 xg 5 min at 4 °C and washed with 20 mL of RPMI. To obtain non-parenchymal cells the suspension was centrifuged at 50 xg for 4 min, the supernatant transferred into a new falcon, washed, and resuspended in 6 mL 37 % Percoll. After centrifugation for 10 min at 400 xg (deceleration 1/ acceleration 9), a red blood cell lysis of the pellet was performed. After washing with PBS/2 % FCS, the cells were further processed for flow cytometric analysis.

1.2.31 Isolation of EVs from liver

Similarly to the isolation of cells from the liver (1.2.29), livers were perfused using EV PBS, collected, and mashed through a 70 µm cell strainer. Digestion media was filtered through a 0.2 µm syringe filter before adding mashed cells. After digestion digested cell suspension was centrifuged at 3000 xg for 5 min. The supernatant containing EVs was kept and cleared from debris by further washing steps for 5 min at 3000 xg, 20 min at 2000 xg, and 45 min at 16,000 xg, repeating every washing step at least twice. The cleared supernatant from the last 16,000 xg washing step was transferred to a fresh

ultracentrifugation tube and EVs were pelleted at 100,000 xg for 1 h. The pellet was resuspended in EV PBS and washed at 100,000 xg for 1 h. The EV pellet was resuspended in various amounts of EV-PBS or other reagents depending on the following experimental uses.

1.2.32 Statistics

Statistical analysis and comparison were performed using Prism 9 (GraphPad). Detailed information on the statistical analyses is supplied in the figure legends. If two groups were compared within one graph, without interest in its relation to another sample, a Mann-Whitney U test was performed. If multiple comparisons were performed within one graph Multiple Mann Whitney tests were applied. Wilcoxon test was applied for comparison of paired and not normally distributed samples. A P-value ≤ 0.05 was considered statistically significant (*P ≤ 0.05, **P < 0.01, ***P < 0.001, ****P < 0.0001). Data points without specific labels or labelled ns are indicative of non-statistically significant results. Data are shown as mean ± SEM. Unless stated in the legend, each data point indicates one independent sample.

2 Results

2.1 Isolation of EVs from live and apoptotic thymocytes

Thymocytes were isolated from murine thymuses and cultured in EV-depleted media for either 2 h to retrieve live thymocytes (liveT) or for 24 h to induce apoptosis in the thymocytes (aT) (Figure 4A). After cultivation, the cells were harvested and stained for the cell death markers Annexin V (AV), and Propidium Iodide (PI) to determine the apoptosis rate by flow cytometry (Figure 4B). Hereby, the AV is binding to phosphatidylserine translocated to the cell surface during early apoptosis and PI is a fluorescent dye binding to DNA and therefore staining late apoptotic and necrotic cells, as the dye can pass into the nucleus. The supernatant was further processed for EV isolation by differential centrifugation as depicted in Figure 4A. In the first centrifugation steps, the remaining cells and debris were washed out from the supernatant, followed by ultracentrifugation at 16,000 xg or 100,000 xg to pellet two separate fractions of EVs containing larger EVs (16k) or smaller EVs (100k), respectively.

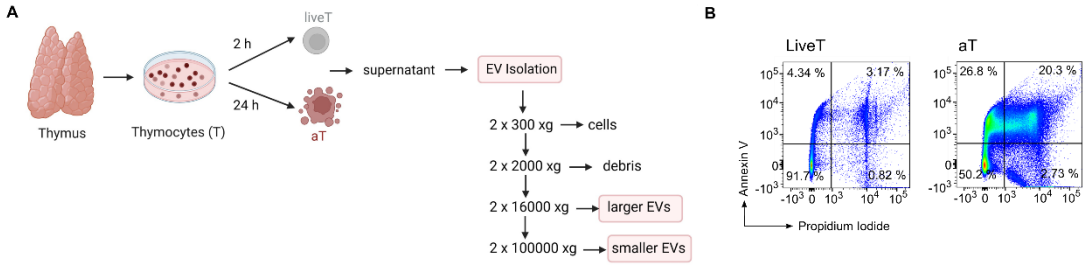


Figure 4: Isolation of EVs from live and apoptotic thymocytes. (A) Schematic overview of the isolation protocol to retrieve EVs from live (liveT) and apoptotic thymocytes (aT). **(B)** Representative dot plots of liveT and aT stained for the cell death markers Annexin V and Propidium Iodide in order to determine the apoptosis rate via flow cytometry.

Apoptosis rates of live and apoptotic thymocytes were ascertained by flow cytometry via staining for AV and PI (Figure 4B). Here, the representative dot plots show that 91.7 % of live thymocytes are negative for AV and PI and thereby considered non-apoptotic, whereas 26.8 % of apoptotic thymocytes are early apoptotic (AV^+) and 20.3 % are late apoptotic (AV^+PI^+) indicating clearly that induction of apoptosis occurred in the apoptotic thymocytes, but also highlighting that the cells of origin for EV isolation consist of a very heterogenous population in terms of their cell death characteristics.

2.2 Characterisation of EVs from live and apoptotic thymocytes

2.2.1 Size and concentration of liveT- and aT-EVs

EV fractions isolated from live and apoptotic thymocytes were visualised by transmission electron microscopy (TEM) allowing a first insight into morphology, size, relative concentration, and purification of the samples. For the in-depth quantification of the size distribution and concentration of the EV fractions Nanoparticle Tracking Analysis (NTA) was performed.

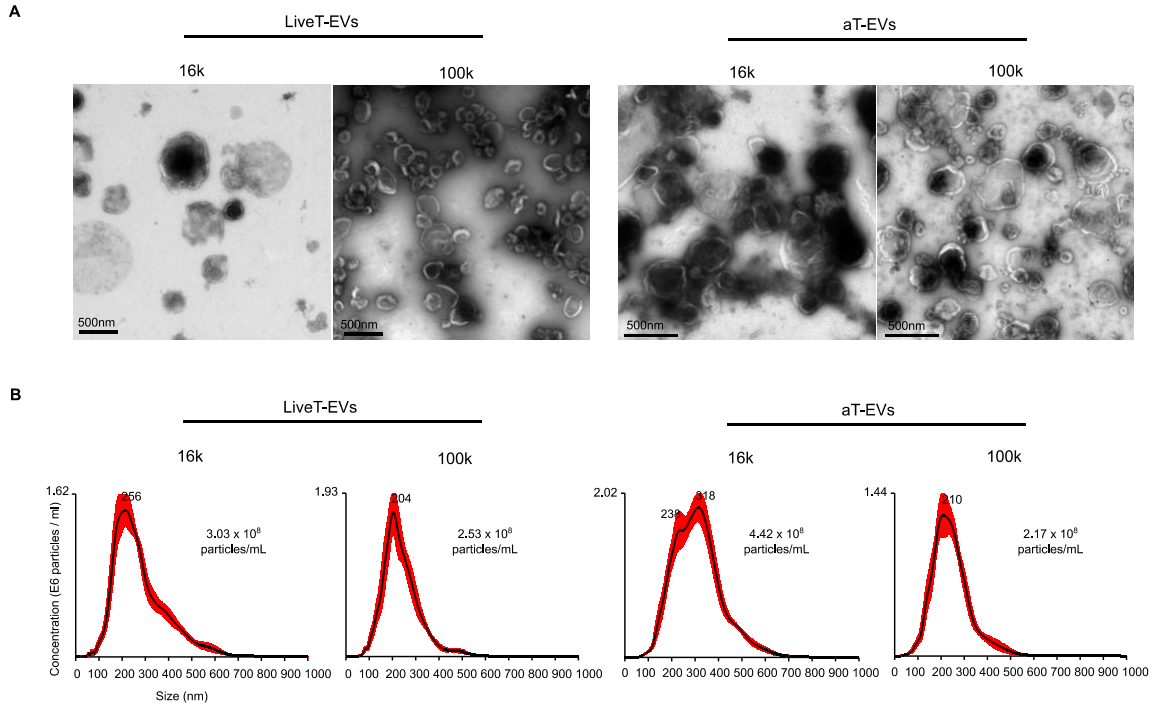


Figure 5: Morphology, size, and concentration of liveT- and aT-EVs. (A) Transmission electron microscopy images of liveT- and aT-EVs fractions. Hereby, 16k and 100k refer to the ultracentrifugation speeds applied to pellet larger EVs (16k) and smaller EVs (100k) respectively. EV samples were observed under a Tecnai Spirit electron microscope operating at 80 kV and images were recorded with a digital CCD camera (performed by Katharina Höhn, BNITM Hamburg). **(B)** Nanoparticle Tracking Analysis was performed using the Nanosight 3000 (Malvern Panalytical) to measure the size distribution and concentration of the EV samples. Representative graphs show the averaged size and concentration calculated from 5 x 30-second measurements per sample. Red error bars indicate +/- 1 standard error of the mean.

Representative TEM pictures indicate that EV fractions pelleted at 16k from live and apoptotic thymocytes contain a much broader variety of particle sizes and exclusively particles larger than 500 nm in diameter, compared to fractions pelleted at 100k. Furthermore, higher numbers of EVs are abundant in the 16k aT-EVs, than in the liveT-EVs (Figure 5A). These observations were confirmed by calculation of size distribution and concentrations by NTA measurements showing that 16k live-T-EVs

are ranging in size between 100 and 700 nm with a peak at 256 nm, whereas 100k live-T-EVs are between 80 and 550 nm in diameter with a peak at 204 nm. The size distribution of the 100k aT-EV fraction is very similar to the 100k live-T-EV fraction only differing by 6 nm in size average. The particle concentration in these samples is also comparably equivalent being 2.53 x 10^8 particles/mL in the 100k liveT-EVs and 2.17 x 10^8 in the 100k aT-EVs. Yet, major differences occur when comparing the 16k fractions. The aT-EVs size peaks twice at 238 and 318 nm, thereby they are generally larger than the live-T-EVs peaking at 256 nm. The overall concentration of 16k aT-EVs of 4.42 x 10^8 particles/mL is almost 1.5 times higher compared to the 16k liveT-EVs.

2.2.2 Detection of apoptosis marker proteins by flow cytometry

The abundance of the apoptosis marker proteins phosphatidylserine and cleaved caspase-3 in the liveT- and aT-EV fractions was analysed using flow cytometry. For the detection of phosphatidylserine on the surface, EVs or buffer controls were extravesicularly stained with AV.

2.2.2.1 Surface phosphatidylserine

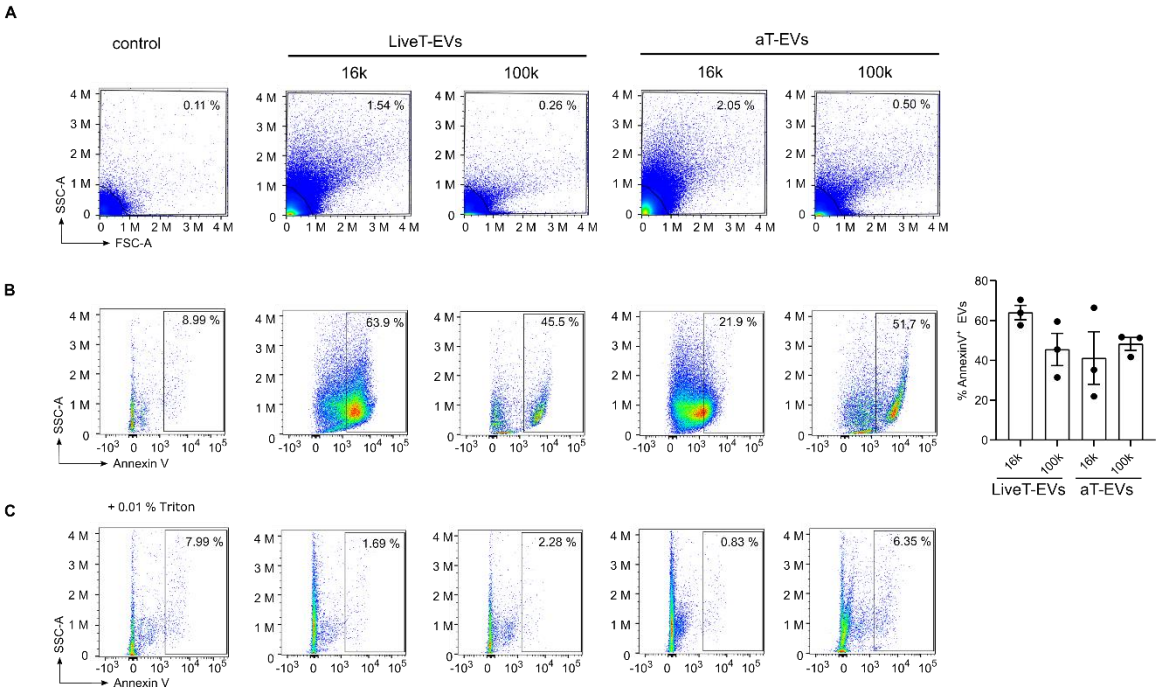


Figure 6: Detection of surface phosphatidylserine on liveT- and aT-EVs by flow cytometry. (A) Representative dot plots showing gating strategy for EV selection based on FSC/SCC characteristics. Buffer control (Annexin V binding buffer, Biolegend) is used as control. **(B)** EVs were further assessed for Annexin V^+ events. Bar graph reports the quantification of Annexin V^+ EVs from three independent experiments. Mann-Whitney U-test (mean ± SEM). **(C)** Representative dot plots of corresponding samples from (A) and (B) treated with 0.01 % Triton-x-100 serving as detergent control.

All events exceeding the buffer control in size (FSC) and granularity (SSC) are considered in the gating strategy for EVs (Figure 6A). Further gating on AV$^+$ EVs shows the abundance of phosphatidylserine in all isolated EV fractions, independently of their size and cells of origin and in line with the fact the phosphatidylserine is considered a bona fide marker of EVs[142] (Figure 6B). Adding Triton-x-100 to the extracellular vesicles leads to disruption of their plasma membrane and as a result, the labelled phosphatidylserine on the EV surface can no longer be detected by flow cytometry (Figure 6C).

Cleaved caspase-3 is the activated form of the enzyme caspase-3, which is responsible for the proteolytic cleavage of many key proteins in the apoptosis signalling cascade and therefore only present in cells undergoing apoptosis. To analyse if cleaved caspase-3 would be present inside EVs released from apoptotic thymocytes, EV fractions were intravascularly stained and measured by flow cytometry (Figure 7).

2.2.2.2 Intravesicular cleaved caspase-3

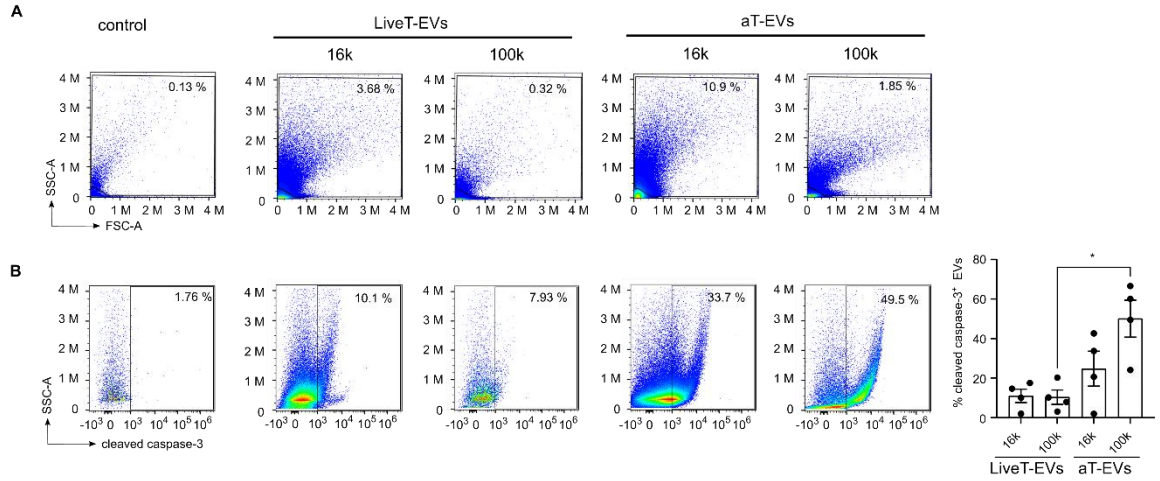


Figure 7: Detection of intravesicular cleaved caspase-3 by flow cytometry. (A) Representative dot plots showing gating strategy for EV selection based on FSC/SCC characteristics. Buffer control (0.1 % perm buffer, BD Bioscience) is used as control. **(B)** EVs were assessed for cleaved caspase-3$^+$ events. Bar graph reports the frequency of cleaved caspase 3$^+$ EVs from four individual experiments. Mann-Whitney U-test, *P ≤ 0.05 (mean ± SEM).

EV gates were set according to the buffer control (Figure 7A) and further gating on cleaved caspase-3$^+$ EVs shows that the frequency of cleaved caspase3 is significantly higher in small EVs isolated from apoptotic than in EVs isolated from live thymocytes. A tendency toward more cleaved caspase-3 can also be observed in the larger EV fraction from aT-EVs compared to liveT-EVs (Figure 7B). These data suggest that cleaved caspase-3, but not phosphatidylserine staining, selectively labels EVs originating from apoptotic instead of live thymocytes.

2.2.3 Detection of surface epitopes via MACSPlex and FACS

Proteins on the EV surface can be related to the originating cell and may also play a role in vesicle function. The surface protein composition of the T-EVs was analysed using MACSPlex (Miltenyi Biotec), which is a bead-based multiplex assay allowing the simultaneous detection of 37 surface epitopes (+2 Isotype controls) by flow cytometry (Figure 8A). Additionally, T-EVs were stained for selected markers with fluorochrome-conjugated antibodies directly for verification of the MACSPlex data (Figure 8B). For the following experiments 16k and 100k EV fractions were analysed as pooled EVs.

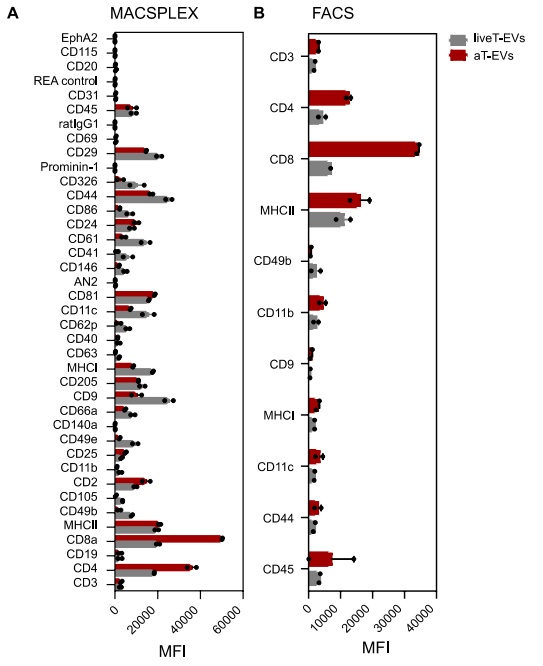


Figure 8: Detection of surface epitopes on EVs. (A) Bar graph presenting the MFI of various surface epitopes in liveT- and aT-EVs, as measured by MACSPlex at the Accuri™ C6 (BD Bioscience). **(B)** MFI of selected surface markers from (A) labelled with fluorochrome-conjugated antibodies and measured by flow cytometry at the Cytek Aurora™. (mean ± SEM).

LiveT-EVs and aT-EVs express multiple of the tested surface epitopes detected by MACSPlex, as presented in Figure 8A. Therein are classical EV markers such as the tetraspanins CD9 and CD81. Both EVs show high expression of the T helper cell marker CD4 and the cytotoxic T cell marker CD8, whereby these markers appear with a higher MFI in the aT-EVs compared to the liveT-EVs. The leukocyte marker CD45, is also present on both types of EVs, as well as the T cell activation marker CD44 and the cytotoxic T cell activation marker CD29. Epitopes that play an important role in the T cell development in the thymus such as CD11c, MHC-I and MHC-II are highly abundant on both, liveT- and aT-EVs. The cell adhesion molecules CD2, CD41, CD61, and CD146 could also be detected on both T-EV samples, but with a higher MFI in the liveT-EVs. Most markers, like CD3, MHC-II, or CD45, show a similar MFI

comparing liveT- and aT-EVs. Especially, T cell activation markers such as CD29, CD44 and CD49b, but also other epitopes like CD9 and MHC-I, the live-T-EVs have an MFI compared to the aT-EVs.

As the MACSPlex is a bead-based assay, the detected MFI levels represent the whole EV population bound to the epitope-specific beads. This allows amplification of the fluorescent signal and detection of epitopes that are only abundant in low amounts per surface area but has the disadvantage that it is not distinguishable if an increasing MFI is caused by EVs expressing higher numbers of the tested markers or by higher numbers of EVs bound to the beads. To obtain more detailed information on the surface epitope abundance on individual liveT- and aT-EVs, single stained samples were measured by flow cytometry. Staining surface epitopes directly with fluorochrome-conjugated antibodies allows the detection of single EVs and not only the bead-bound bulk population. Hereby, major findings from the MACSPlex analysis could be confirmed. The most abundant epitopes on both EVs are CD4, CD8 and MHC-II, with a tendency towards higher abundance on aT-EVs compared to liveT-EVs (Figure 8B). Surface expression of T cell markers, CD3, CD49b and CD44 could also be confirmed, as well as detection of CD11b, CD11c, CD45 and MHC-I. However, their expression levels were almost equal comparing the liveT- and the aT-EVs. CD9 which appeared highly abundant in the MACSPlex, could only be detected in low amounts by flow cytometry.

2.3 Characterisation of Mϕs taking up liveT- or aT-EVs

To be able to track the uptake of EVs by flow cytometry, EVs were labelled with the fluorescent dye CFSE. Specifically, CFDA-SE was used to dye the EVs, as it is a non-fluorescent membrane permeable molecule only becoming fluorescent CFSE through hydrolysis of its diacetic groups once it reaches the cytosol where esterases are present.

2.3.1 Mϕs take up liveT and aT-EVs *in vitro*

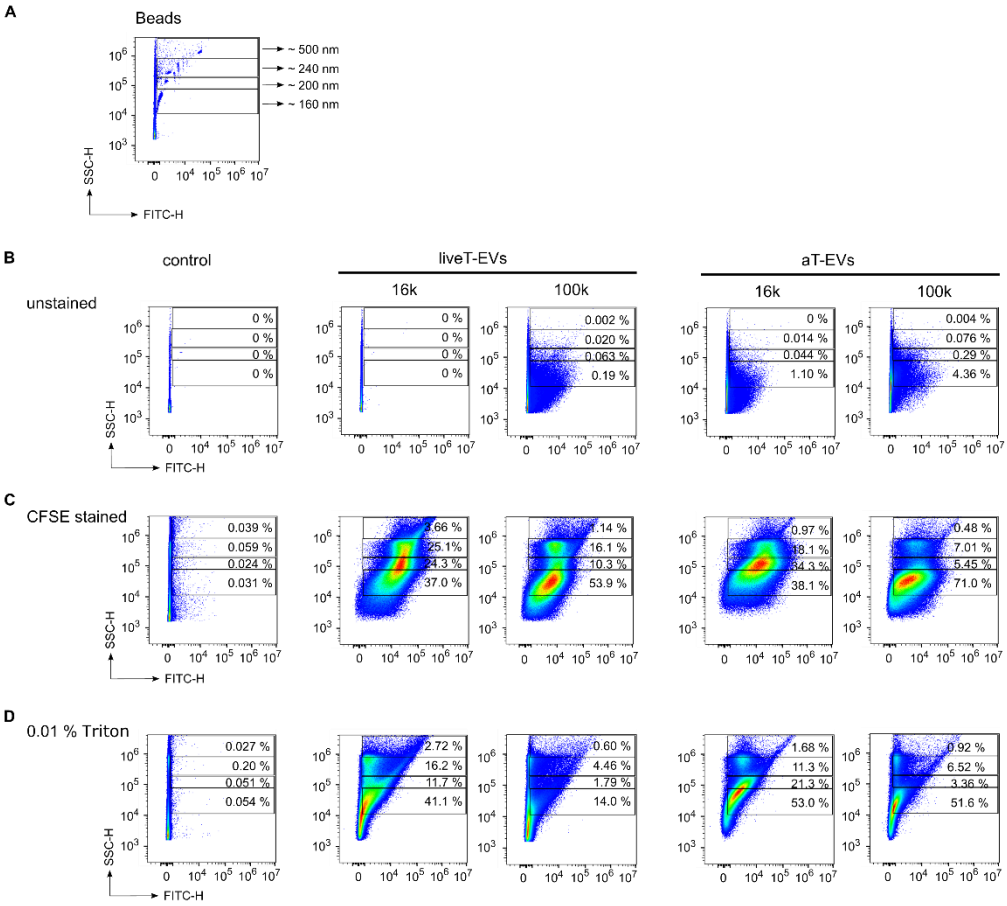


Figure 9: CFDA-SE labelling of EVs. Fluorescent labelling of liveT- and aT-EVs with CFDA-SE (Thermofisher Scientific). **(A)** Instrument setup according to Megamix-Plus SSC beads (Biocytex). Gates were set on size-specific bead populations, fluorescent in the FITC channel. Analysis was performed excluding background noise and $FITC^-$ events. **(B)** Dot plots show recorded events from buffer control liveT-EV and aT-EV samples according to their size (SSC-H) and CFSE signal (FITC-H). EV gates were set according to the bead control, as reported in (A). $FITC^+$ events were quantified. **(C)** EVs from (B) were labelled with CFDA-SE and their percentage quantified by flow cytometry, by gating according to A. **(D)** Representative dot plots of corresponding samples from (C) treated with 0.01 % Triton-x-100 as detergent control.

A mix of fluorescent beads (Megamix-Plus SSC, Biocytex) of varied defined diameters was used to set up the flow cytometer for the measurement of CFSE-labelled EVs. The beads are labelled with Fluorescein isothiocyanate (FITC), which appears to have an overlapping fluorescence spectrum to CFSE and therefore both colours are detected in the same channels at the Cytek Aurora™. Four gates were set according to the diameter of the beads at around 160 nm, 200 nm, 240 nm, and 500 nm (Figure 9A). Setting up the instrument using the beads allows a rough estimation of the measured EVs. Firstly, the unstained buffer control and unstained 16k and 100k fractions of live-T-EVs were measured

and gates were set on the different size populations according to the beads measured beforehand (Figure 9B). No $CFSE^+$ events were detected in the buffer control and the 16k liveT-EVs. Very low percentages of $CFSE^+$ events were present in the 100k liveT-EV and the 16k and 100k aT-EV samples. As no CFSE was detected in the first EV sample, it seems likely that these $CFSE^+$ events in the unlabelled samples are caused by contamination of the instrument with some fluorescent particles of the stained samples (Figure 9C) that were measured in between. Nevertheless, the frequency of the detected $CFSE^+$ events in the unlabelled samples is only minor. The same samples as in Figure 6B were labelled with CFSE and measured under the same conditions. In the buffer control, almost no $CFSE^+$ events were detected, whereas high frequencies of all EV samples showed to be $CFSE^+$. In total, around 90 % of all detected EVs are labelled with CFSE (Figure 9C). Comparing the 16k and 100k fractions, the 100k fraction consists of mainly smaller EVs (160 nm), whereas the 16k fraction contains more larger EVs (>200nm), confirming the observations from the NTA (Figure 5B). Again, Triton-x-100 was added to the extracellular vesicles leading to disruption of their plasma membrane. Albeit the frequency of $CFSE^+$ EVs was not completely diminished, the mean fluorescence intensity was reduced (Figure 9D). Taken together, EVs were successfully labelled with CFSE and detected by flow cytometry. To next assess if Mϕs would uptake T-EVs, BMDMs were co-incubated with the CFSE-labelled EVs, and their uptake was tracked via flow cytometry. Therefore, BMDMs were harvested after co-incubation and labelled with fluorescently labelled antibodies against the Mϕ identification markers CD11b and F4/80, as reported in the gating strategy in Figure 10A.

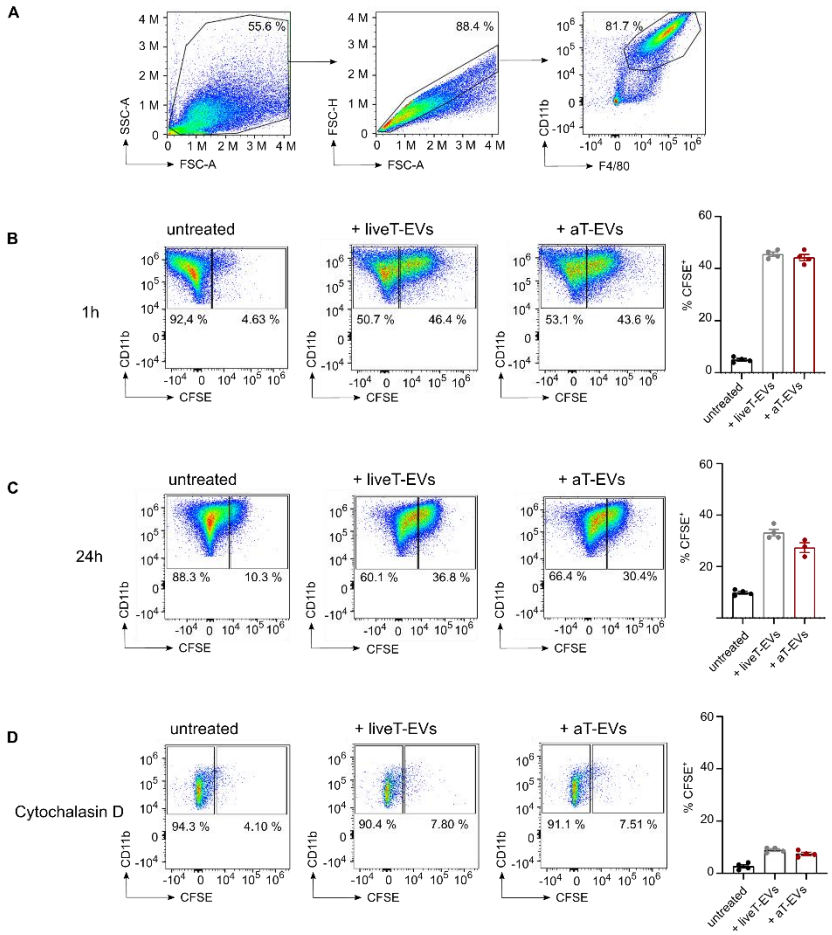


Figure 10: Flow cytometric analysis of the uptake of liveT- or aT-EVs by Mϕs. (A) Gating strategy for selection of CD11b$^+$F4/80$^+$ Mϕs differentiated from the bone marrow. **(B)** Representative dot plots showing the frequency of CD11b$^+$F4/80$^+$ Mϕs reflecting the Mϕs taking up CFSE-labelled EVs upon 1 h and **(C)** 24 h of co-culture. Untreated sample refers to Mϕs treated with control buffer. Quantification of the uptake rate of three individual samples is depicted on the right. **(D)** Mϕs were treated with Cytochalasin D (10 µg/mL) 1 h prior to co-incubation with EVs. Representative dot plots and uptake rates show Mϕs upon 1 h of co-incubation. Mann-Whitney U-test (mean ± SEM).

After 1 h of co-incubation with liveT- or aT-EVs, roughly 45 % of CD11b$^+$F4/80$^+$ Mϕs were CFSE$^+$, meaning they had taken up the labelled EVs (Figure 10B). A minor proportion of Mϕs occurs to be autofluorescent for CFSE, as detected in the control Mϕs that did not receive EVs. After 24 h of co-incubation, CFSE can still be detected in the Mϕs that have taken up EVs, but the percentage of CFSE$^+$ Mϕs decreases to 35 % in the live-T-EV-treated and to 30 % in the aT-EV-treated, suggesting a degradation of the dye by the Mϕs over time (Figure 10C). Treatment with Cytochalasin D inhibits the cytoskeleton rearrangement of the Mϕs and therefore blocks the ingestion processes. After Cytochalasin D treatment only 7 % CFSE$^+$ Mϕs are detected, only 3 % more than in the autofluorescence control (Figure 10D). This indicates that the uptake of EVs by Mϕs is dependent on

the cytoskeleton rearrangement and that the CFSE$^+$ events were actually the result of EV uptake and not binding to the Mϕ surface.

2.3.2 Characterisation of Mϕs 24 h upon uptake of liveT- or aT-EVs

To assess differences between Mϕs that would or would not uptake EVs, Mϕs were labelled for a variety of Mϕ characterisation markers after incubation with live-T or aT-EVs for 24 h.

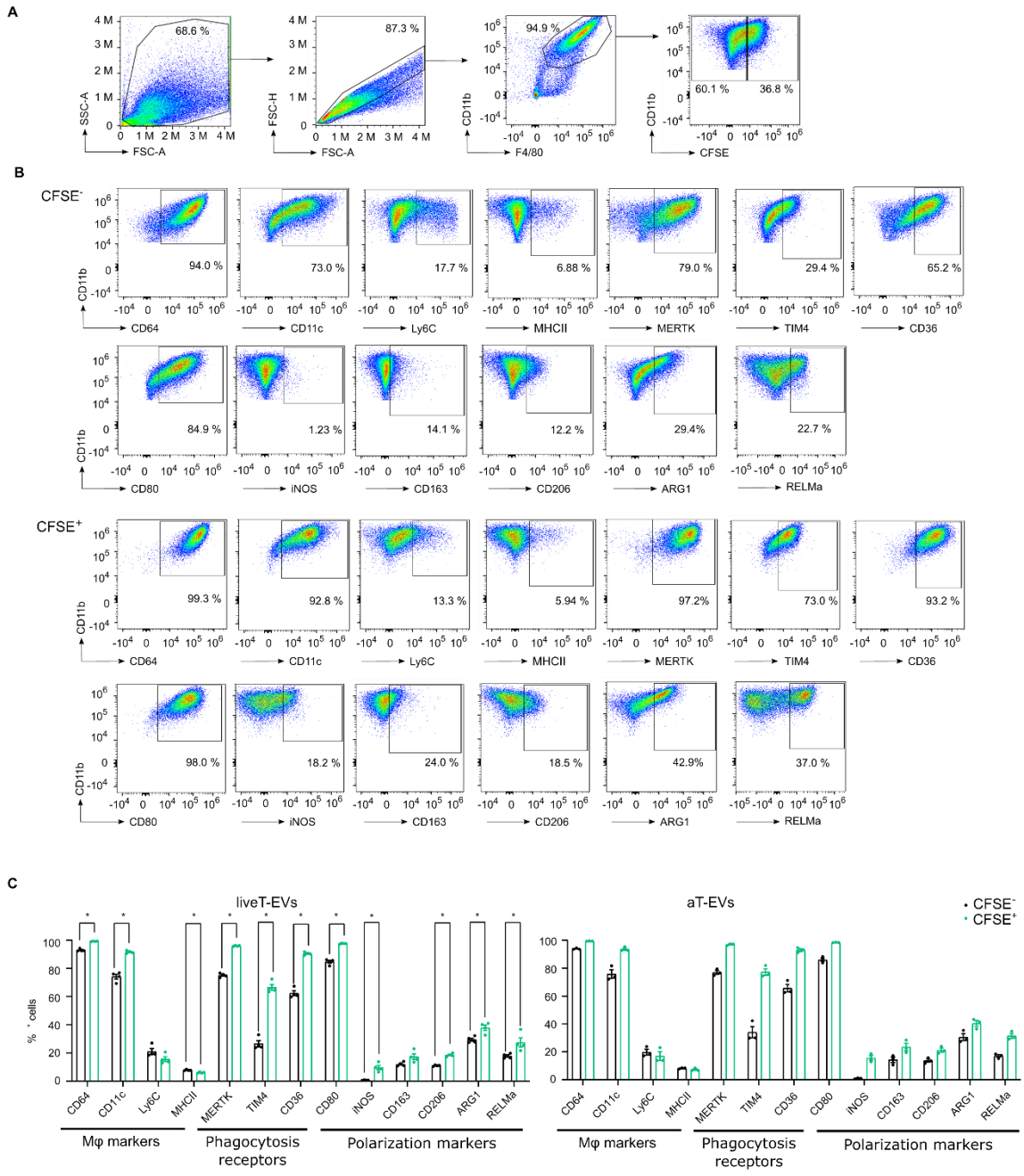


Figure 11: Characterisation of Mϕs 24 h upon uptake of liveT- or aT-EVs by flow cytometry. (A) Gating strategy for flow cytometric analysis of CD11b$^+$F4/80$^+$ Mϕs that have taken up (CFSE$^+$) or not taken up (CFSE$^-$) CFDA-SE-labelled T-EVs. **(B)** Representative dot plots indicating CFSE$^-$ and CFSE$^+$ Mϕs expressing

different Mϕ polarisation and identity markers. **(C)** Bar graphs showing the frequency of $CFSE^-$ and $CFSE^+$ Mϕs expressing the markers as in (B). Flow cytometry analysis on Mϕs has been performed upon their incubation with either liveT-EVs (left) or aT-EVs (right) for 24 h. Multiple Mann-Whitney tests, *P ≤ 0.05 (mean ± SEM).

Firstly, by gating on $CFSE^+$ or $CFSE^-$ $CD11b^+F4/80^+$ Mϕs, Mϕs that have taken or not taken up EV were distinguished (Figure 11A). Second, analysis of different polarisation markers in the two distinct Mϕ populations ($CFSE^+$ or $CFSE^–$), allows their phenotypical profiling (Figure 11B).

Mϕs that take up liveT-EVs show higher expression of Mϕ markers CD64 and CD11c, a tendency toward lower Ly6C expression and significantly lower expression of MHC-II (Figure 11C). Strikingly, Mϕs that take up liveT-EVs are highly positive for the phagocytosis receptors MERTK, TIM4 and CD36. The levels of various Mϕ polarisation markers are also elevated in Mϕs that have taken up liveT-EVs compared to Mϕs that have not. This includes markers for pro-inflammatory Mϕs (CD80, iNOS), as well as anti-inflammatory Mϕs (CD206, ARG1, RELMα). Interestingly when comparing Mϕs that have or have not taken up aT-EVs, the signature of the Mϕs for the tested markers looks similar, though these observations are not statistically significant.

2.3.3 Peritoneal Mϕs take up liveT and aT-EVs *in vivo*

BMDMs are a commonly used model for *in vitro* studies. However, by themselves, they cannot recapitulate the more complex settings that take place *in vivo* where key factors like cell-cell communication, cytokine levels and immune cell infiltration all contribute to tissue maintenance and resolution of inflammation. Therefore, to study the interaction of EVs and Mϕs and their impact on the resolution of inflammation *in vivo,* a second model was used, the thioglycolate-induced peritonitis.

Injection of thioglycolate (TG) into the peritoneum of mice, leads to induction of inflammation and resulting infiltration of immune cells to the peritoneum. Thereby, peritoneal Mϕs (pMϕs) phagocytosing dying cells in the peritoneal cavity, play a key role in the resolution of inflammation[143]. To analyse the uptake of EVs in this setting, CFSE-labelled T-EVs were injected i.p. 48 h after TG and the peritoneal lavage was collected and analysed by flow cytometry (Figure 12A).

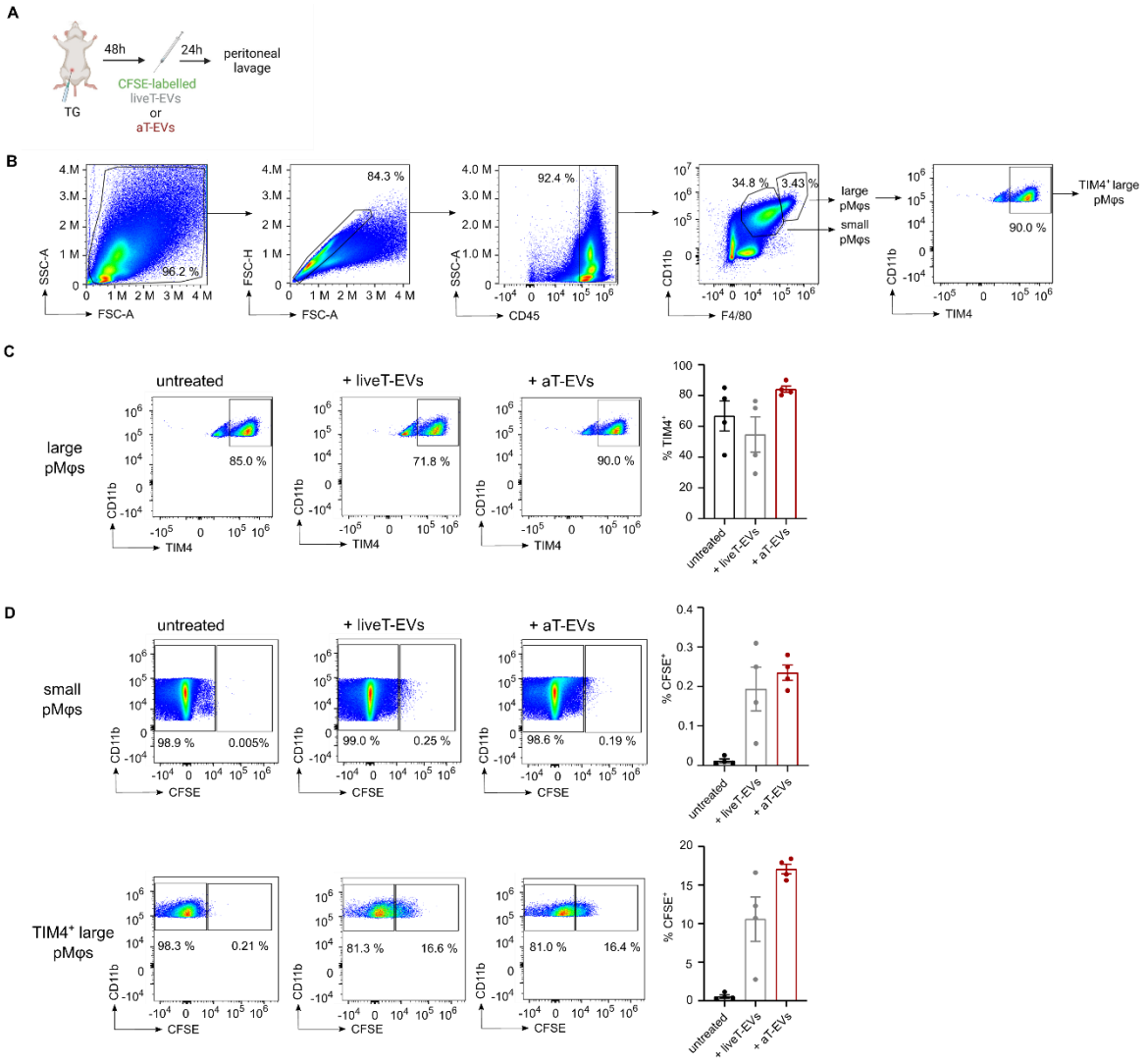


Figure 12: The uptake of liveT-EVs and aT-EVs by pMφs in a model of thioglycolate-induced peritonitis. (A) Schematic overview of the experimental setup for the flow cytometric analysis of the uptake of T-EVs by pMφs. **(B)** Representative dot plots reporting the gating strategy for selection of Mφs from peritoneal lavage. Mφs are discriminated as small pMφs ($CD11b^{+}F4/80^{+}$) and $TIM4^{+}$ large pMφs ($CD11b^{hi}F4/80^{hi}TIM4^{+}$). **(C)** Representative dot plots and bar graph showing the frequency of $TIM4^{+}$ large pMφs isolated from the peritoneal cavity of mice treated with thioglycolate. **(D)** Representative dot plots and the corresponding quantification of the frequency of small and $TIM4^{+}$ large pMφs which have taken up liveT-EVs, aT-EVs. The untreated sample refers to pMφs isolated from mice treated with PBS control. Mann-Whitney U-test (mean ± SEM).

In the peritoneum two major populations of pMφs are present: the small and the large pMφs. They can be distinguished by their CD11b and F4/80 expression levels as indicated in the gating strategy (Figure 12B). Additionally, large pMφs expressing TIM4 are considered resident pMφs. Interestingly, 24 h upon injection of aT-EVs, in tendency higher frequency of $TIM4^{+}$ large pMφs are found in the peritoneal lavage compared to untreated or live-T-EV-treated mice (Figure 12C). Small pMφs do not uptake T-EVs, whereas $TIM4^{+}$ large pMφs do (Figure 12D).

2.3.4 Characterisation of pMϕs 24 h after uptake of liveT and aT-EVs *in vivo*

As TIM4$^+$ large pMϕs have been shown to take up liveT- and aT-EVs, we next intended to identify differences between pMϕs that would or would not uptake EVs. Therefore, TIM4$^+$ large pMϕs were analysed for the expression of a variety of Mϕ characterisation markers by flow cytometry 24 h after injection of live-T or aT-EVs in TG-treated mice, similarly to the BMDMs described in 2.3.2.

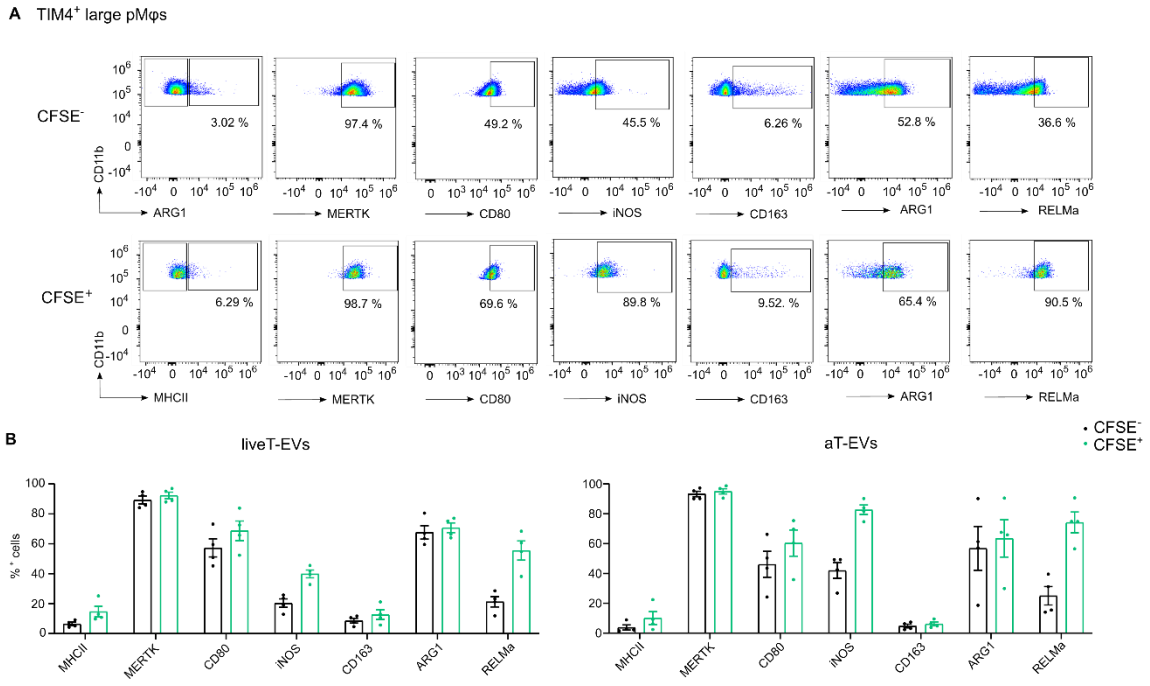


Figure 13: Characterisation of pMϕs in a model of thioglycolate-induced peritonitis mice 24 h upon uptake of liveT- or aT-EVs by flow cytometry. (A) Representative dot plots showing gating on CFSE$^+$ or CFSE$^-$ TIM4$^+$ large pMϕs expressing different polarisation and identity markers. **(B)** Bar graphs showing the frequency of CFSE$^+$ or CFSE$^-$ TIM4$^+$ large pMϕs expressing the markers as reported in (A) 24 h after injection of liveT-EVs (left) or aT-EVs (right). Multiple Mann-Whitney tests (mean ± SEM).

TIM4$^+$ large pMϕs were gated as shown in Figure 12A and the frequency of marker$^+$ pMϕs was calculated from the CFSE$^+$ or CFSE$^-$ population (Figure 13A). TIM4$^+$ large pMϕs that take up liveT-EVs and are therefore CFSE$^+$ show no difference in expression of Mϕ markers MHC-II and MERTK, a tendency towards higher expression of the pro-inflammatory polarisation markers CD80 and iNOS and the anti-inflammatory polarisation markers ARG1 and RELMα compared to CFSE$^-$ pMϕs (Figure 13B). The expression pattern of pMϕs that take up aT-EVs looks comparatively similar compared to the Mϕs treated with liveT-EVs, but the iNOS expression in the CFSE$^-$ and the CFSE$^+$ populations is overall double as high.

2.3.5 Uptake of liveT or aT-EVs does not impact Mϕs phagocytic activity

When characterising Mϕs that would uptake T-EVs in 2.3.2. and 2.3.4., high expression of phagocytosis receptors was observed. Therefore, the influence of the uptake of liveT- or aT-EVs on the phagocytic capacity of the Mϕs *in vitro* and *in vivo* was investigated next.

2.3.5.1 Phagocytic capacity of liveT- and aT-EV-treated BMDMs

To investigate the influence of EVs on Mϕ phagocytic capacity, BMDMs were co-incubated with live-T- or aT-EVs 1 h prior to the addition of apoptotic thymocytes, which are here used as target cells to be phagocytosed (Figure 14A). In order to track the initial capacity of Mϕs to take up EVs, EVs were labelled with CFSE and apoptotic thymocytes (aTs) were labelled with eFluor-450 before the incubation with the BMDMs.

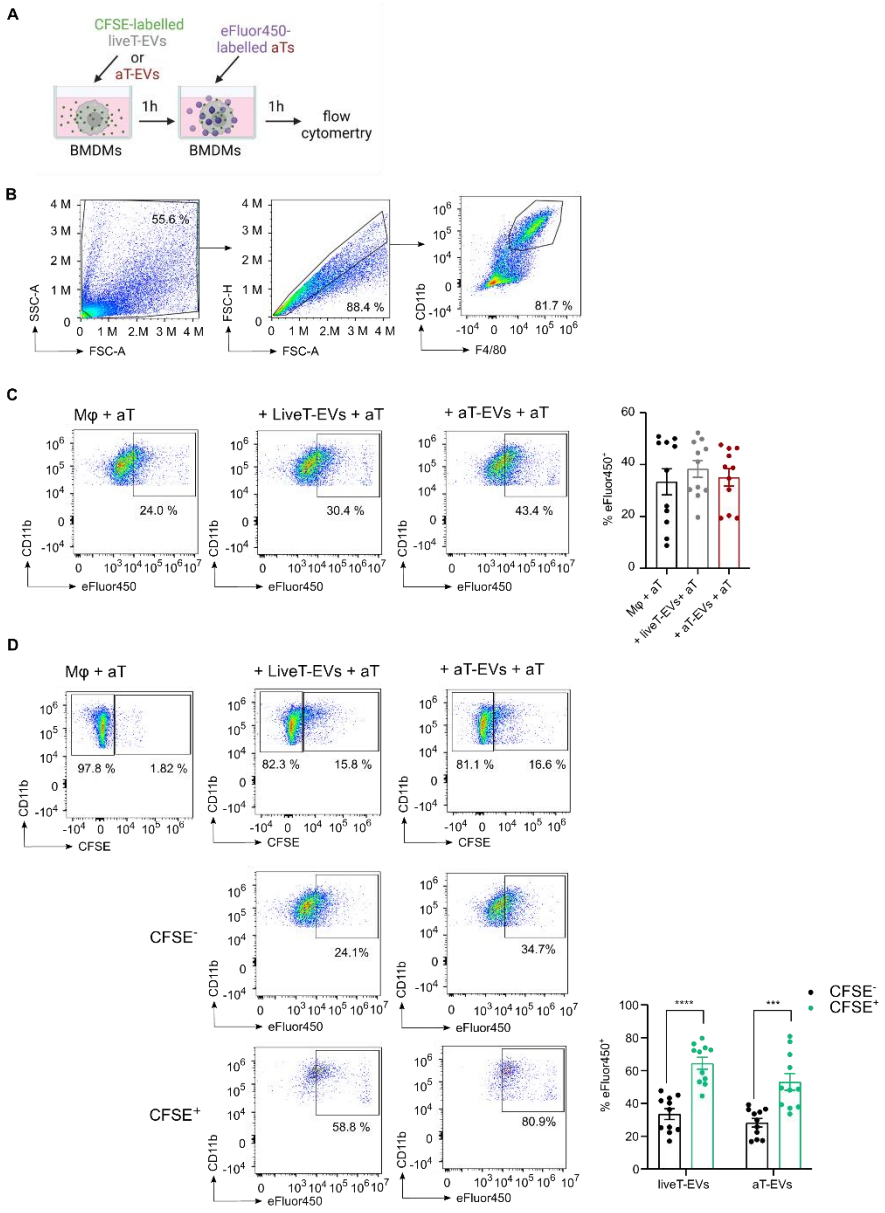


Figure 14: Flow cytometric analysis of the phagocytic capacity of liveT- and aT-EV-treated BMDMs. **(A)** Schematic overview of the experimental setup to investigate how the pre-treatment of Mφs with liveT- and aT-EVs (CFSE-labelled) impact their capacity to phagocytose apoptotic thymocytes (aT; eFluor450-labelled) **(B)** Gating strategy for the identification of $CD11b^{+}F4/80^{+}$ Mφs. **(C)** Representative dot plots and quantification of the frequency of Mφs labelled with the aT dye (eFluor450), reflecting their capacity to phagocytose the apoptotic thymocytes. Experiments were performed as described in (A). **(D)** Representative dot plots and corresponding quantification of the frequency of Mφs taking up the eFluor-450-labelled apoptotic thymocytes. Mφs are discriminated as $CFSE^{+}$ or $CFSE^{-}$ based on their response to the pre-treatment with CFSE-labelled liveT- and aT-EVs. Multiple Mann-Whitney tests, ****P ≤ 0.0001 ***P ≤ 0.001 (mean ± SEM).

Firstly, to assess their phagocytic capacity, a gating strategy was set to identify $CD11b^{+}F4/80^{+}$ Mφs (Figure 14B). To calculate the frequency of Mφs that had taken up apoptotic thymocytes, gates were

further set on eFluor450$^+$ events. No difference appears in the frequency of Mϕs taking up apoptotic thymocytes when they were previously treated with liveT-EVs or aT-EVs or a PBS control (Figure 14C). As the CD11b$^+$F4/80$^+$ Mϕ population consist of a heterogenous population of Mϕs that have not and that have taken up live-T or aT-EVs, an additional gating distinguishing CFSE$^-$ and CFSE$^+$ Mϕs was added. Comparing CFSE$^-$ and CFSE$^+$ Mϕs shows that the frequency of eFluor450$^+$ Mϕs is almost double as high (but not statistically significant), in the CFSE$^+$ compared to the CFSE$^-$ Mϕs, independently of the fact whether they have taken up liveT- or aT-EVs (Figure 14D). Taking these findings together, the uptake of EVs does not seem to have an influence on the Mϕs phagocytic capacity per se, but Mϕs that have previously taken up these EVs are significantly more prone to uptake apoptotic thymocytes subsequently, independently of the source of EVs being live or apoptotic thymocytes.

2.3.5.2 Phagocytic capacity of aT-EV-treated large pMϕs

To investigate the influence of aT-EVs on the phagocytic capacity of pMϕs *in vivo*, CFSE-labelled EVs were injected in TG-treated mice 3 h prior to injection of eFluor-450 labelled apoptotic thymocytes (aTs). The peritoneal lavage was collected 1 h later and peritoneal cells were analysed by flow cytometry (Figure 15A).

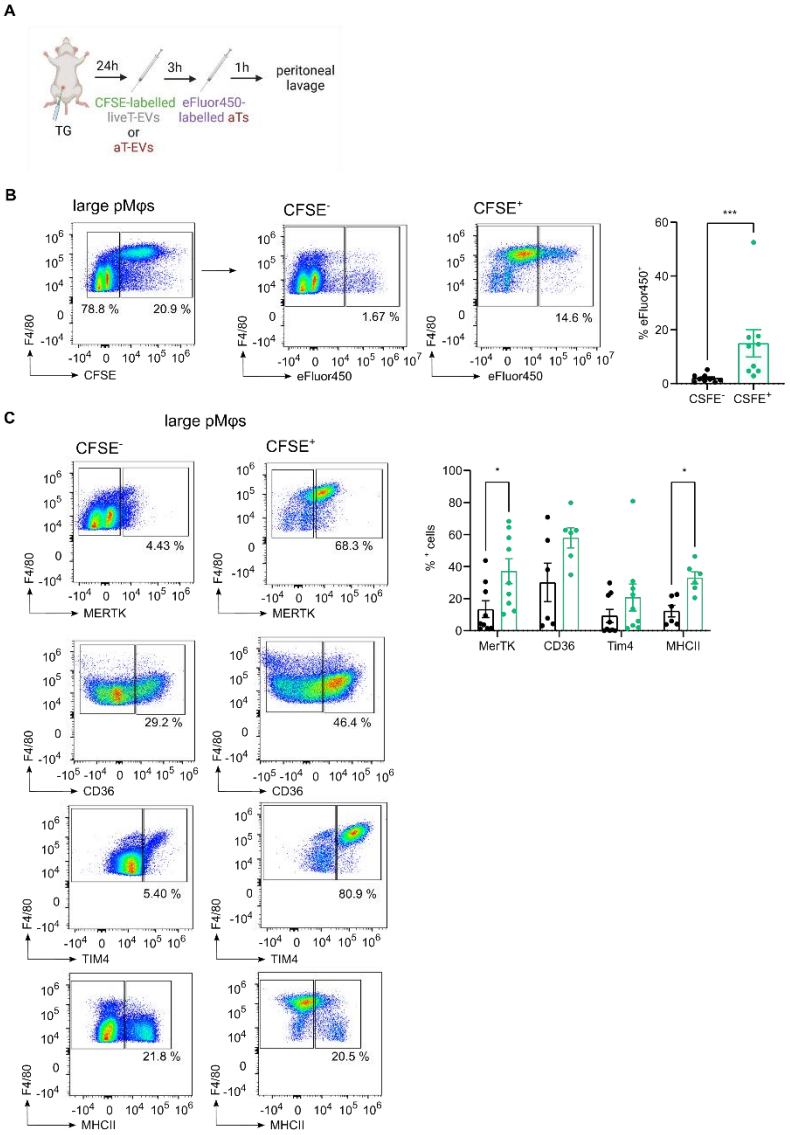


Figure 15: Flow cytometric analysis of the phagocytic capacity of aT-EV-treated large pMφs in a model of thioglycolate-induced peritonitis. (A) Schematic overview of the experimental setup to investigate how the pre-treatment of pMφs with aT-EVs (CFSE-labelled) impacts their capacity to phagocytose apoptotic thymocytes (aTs; eFluor450-labelled). **(B)** Representative dot plots and quantification of the frequency of large pMφs labelled with the aT dye (eFluor450), reflecting their capacity to phagocytose the apoptotic thymocytes. Large pMφs are discriminated as $CFSE^+$ or $CFSE^-$ based on their response to the pre-treatment with CFSE-labelled aT-EVs. Mann-Whitney U test, ***P ≤ 0.001 (mean ± SEM). **(C)** Representative dot plots and corresponding quantification of the frequency of pMφs expressing the phagocytosis receptors MERTK, CD36 and TIM and the antigen presentation molecule MHC-II in the $CFSE^+$ or $CFSE^-$ large pMφs. Multiple Mann-Whitney tests, *P ≤ 0.05 (mean ± SEM).

The frequency of pMφs taking up apoptotic thymocytes was analysed by gating on large pMφs that are either $CFSE^-$ or $CFSE^+$. Similar to what has been observed *in vitro* (Figure 14D), pMφs that have previously taken up aT-EVs showed a drastic increase in phagocytosis of apoptotic thymocytes

compared to pMϕs that have not (Figure 15B). $CFSE^-$ or $CFSE^+$ large pMϕs were also analysed for differences in expression of the phagocytic receptors MERTK, CD36 and TIM4 and the antigen-presenting molecule MHC-II. The frequency of pMϕs expressing MERTK and MHC-II was significantly higher in the $CFSE^+$ large pMϕs and in tendency higher for CD36 and TIM4 compared to $CFSE^-$ large pMϕs (Figure 15C).

2.3.6 BMDMs phenotype is distinct after uptake of liveT- or aT-EVs.

To evaluate the transcriptomic changes that are induced in Mϕs upon uptake of liveT- or aT-EVs, mRNA was isolated and bulk-RNA sequencing was performed after 24 h of co-incubation of Mϕs with either liveT-EVs or aT-EVs.

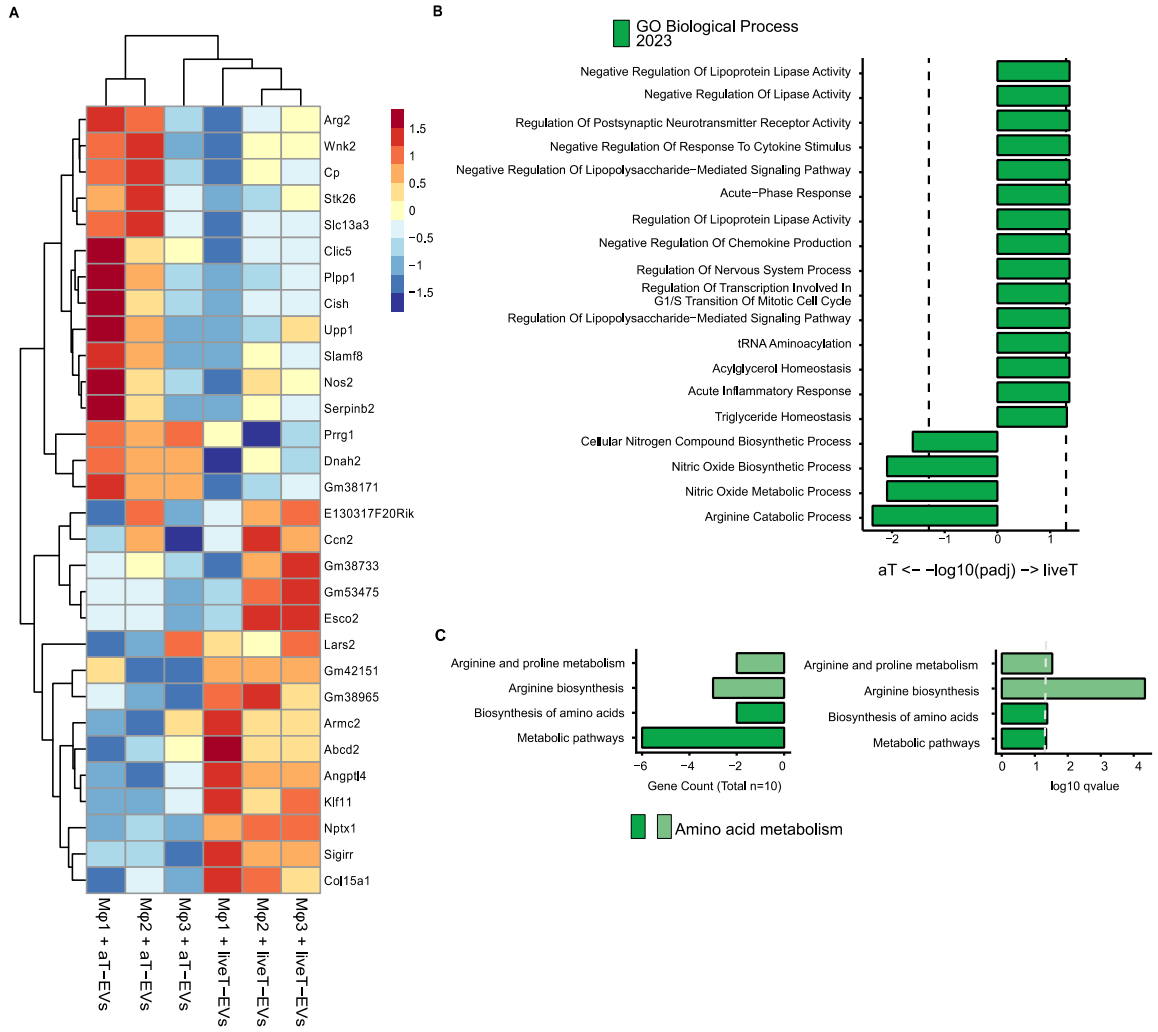


Figure 16: Uptake of live-T- or aT-EVs affect BMDMs transcriptomic signature. (A) Heat map visualizing the 30 genes (15 highest expressed after liveT-EV-treatment; 15 highest expressed after aT-EV-treatment) with the highest log2 fold change (log2FC) from bulk-RNA-Sequencing analysis of three individual Mϕ samples treated with live-T or aT-EVs for 24 h (filtered for log2 fold change ≥0.5). **(B)** GO

term analysis of the genes depicted in (A). **(C)** KEGG pathway analysis of genes depicted in (A). (Left) The number of genes involved in the result pathways and (Right) the corresponding log10 q value.

The 15 highest expressed genes in aT-EV-treated BMDMs and the 15 highest expressed genes in liveT-EVs-treated BMDMs are depicted in the heatmap in Figure 16A. Examples of upregulated genes upon uptake of aT-EVs are *Nos2*, the gene encoding for nitric oxide synthase, *Cish*, a member of the Suppressor of cytokine signalling (SOCS) family and *Serpinb2*, encoding for the plasminogen activator inhibitor type-2.

GO term analysis was performed from the list of highest expressed genes (Figure 16B). Interestingly, all GO terms upregulated after uptake of aT-EVs are involved in Nitric oxide processes. KEGG pathways analysis reveals the most upregulated pathways in liveT-EV-treated BMDMs are associated with the metabolism and biosynthesis of amino acids, especially arginine and proline (Figure 16C).

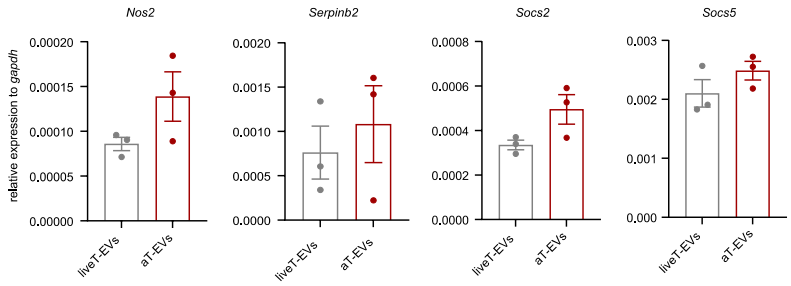


Figure 17: Expression levels of selected genes from transcriptomic analysis of liveT- or aT-EVs-treated BMDMs. Graphs reporting gene expression of *Nos2, Serpinb2*, *Socs2* and *Socs5* relative to *gapdh* as detected by RT-qPCR. Mann-Whitney U-test (mean ± SEM).

The expression of selected genes upregulated in the bulk sequencing analysis of aT-EV-treated BMDMs compared to liveT-EVs-treated BMDMs was validated in the sequencing samples by RT-qPCR (Figure 17). Thereby expression of *Nos2*, *Serpinb2*, *Socs2* and *Socs5* (related to *Cish*) were not significant, but in tendency higher in BMDMs treated with aT-EVs compared to liveT-EVs.

2.3.7 LiveT-EVs target nitric oxide pathway in Mϕs

As *Nos2*, the gene encoding for nitric oxide synthase, was one of the highly expressed genes in the transcriptomic analysis of aT-EVs-treated BMDMs, protein expression of iNOS and subsequent nitric oxide (NO) production were analysed in Mϕs next.

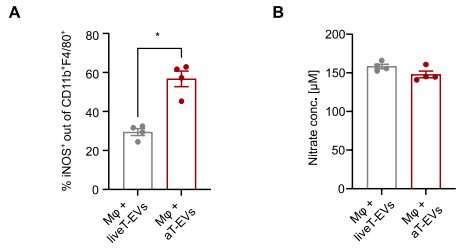


Figure 18: Detection of iNOS protein expression and NO production by Mϕs treated with liveT- or aT-EVs for 24 h. (A) Flow cytometric analysis of iNOS expression in $CD11b^{+}F4/80^{+}$ Mϕs. **(B)** Nitrate concentration in the supernatant of liveT-EV and aT-EV-treated Mϕs measured by Nitric oxide assay (ThermoFisher Scientific). Mann-Whitney U test, *P ≤ 0.05 (mean ± SEM).

The frequency of BMDMs expressing iNOS is double as high in BMDMs co-incubated with aT-EVs compared to Mϕs treated with liveT-EVs as measured by flow cytometry (Figure 18A). However, here the higher expression of iNOS did not result in the detection of higher amounts of nitrate in the supernatant of the respective BMDMs, as measured by Nitric Oxide Assay (ThermoFisher Scientific) (Figure 18B).

These data indicate that EVs from liveT- and aT-EVs seem to have only minor, but still distinct effects on the Mϕ phenotype and transcriptomic signature, especially regarding nitric oxide-related pathways. Based on these results, we wanted to investigate if these alterations might have an impact on the function of the Mϕs.

2.3.8 LiveT- and aT-EV treatment of Mϕs does not influence fibroblast migration

To examine to what extent the uptake of liveT- and aT-EVs affects the Mϕs function, the supernatants from experiments where Mos were co-cultured with liveT- or aT-EVs were harvested after 24 h, analysed for their cytokine content and subsequently for their impact on fibroblast migration capacity. A schematic overview of the experimental setup is depicted in Figure 19A.

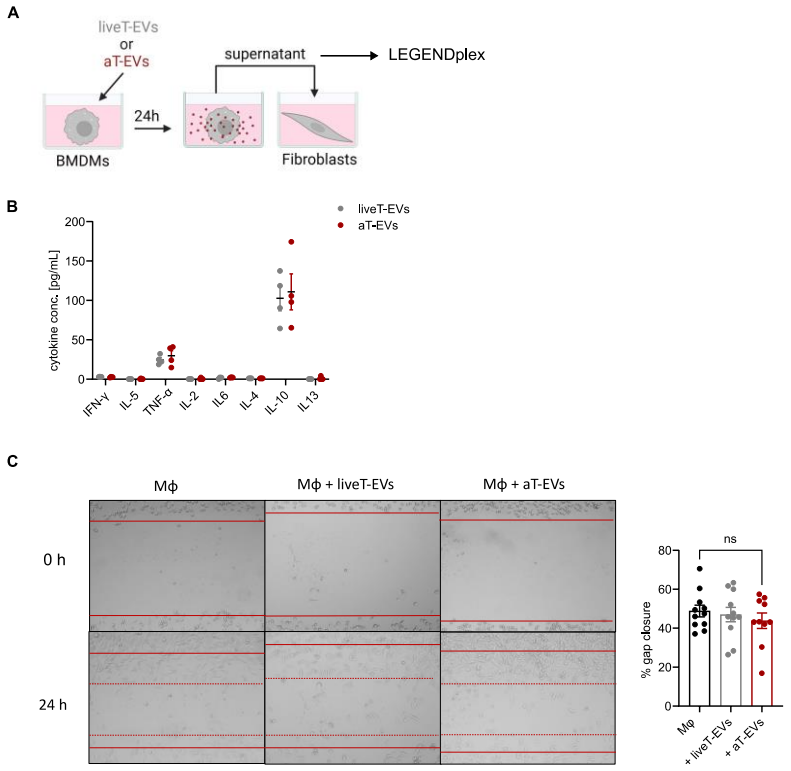


Figure 19: Supernatants from Mϕs incubated with liveT- or aT-EVs have no influence on fibroblast migration. (A) Schematic overview of the experimental setup established to investigate the impact of soluble mediators released by Mϕs incubated with liveT- or aT-EVs on fibroblast migration. **(B)** Cytokine levels in the supernatants of Mϕs treated with live-T- or aT-EVs, measured by LEGENDplex (Biolegend). **(C)** Representative images show the migration of fibroblasts upon incubation with the Mϕs treated as in (A). Solid lines indicate the original gap width at 0 h post supernatant transfer, whereas dotted lines indicate the gap 24 h later. The percentage of gap closure after 24 h was calculated using ImageJ and is presented in the graph to the right. Mann-Whitney U test, nsP > 0.05 (mean ± SEM).

The levels of cytokines released during the 24 h co-incubation time into the supernatant were determined via LEGENDplex (Biolegend) (Figure 19B). Thereby most of the selected cytokines measured were only present in very low concentrations, except TNF-α and IL-10. However, no differences can be detected comparing cytokine concentrations between supernatants of liveT- and aT-EV-treated Mϕs.

Nevertheless, the supernatants were transferred to fibroblasts to perform a fibroblast migration assay in order to determine the impact of the supernatant contents on fibroblast migration capacity (Figure 19C). Therefore, a scratch was made, disrupting the fibroblast monolayer and its width was measured at 0 h after supernatant transfer. After 24 h of incubation, the gap width was measured again. To draw conclusions from the gap width to the fibroblast migration capacity, the gap closure in % was calculated for every sample. No significant difference in the effects of supernatants from untreated Mϕ, liveT-EV-

or aT-EV-treated Mϕs were observed thus indicating that the EV uptake does not influence the Mϕ wound healing capacity.

2.4 Transfer of liveT or aT-EVs in *S. mansoni*-infected mice modulates disease pathology

To further investigate if liveT-EVs and aT-EVs have the capacity to induce functional changes in their target cells and to what extent that might impact schistosomiasis disease pathology, adoptive transfer of liveT-EVs, aT-EVs or a PBS control has been performed at week 6 and 7 p.i. in *S. mansoni*-infected mice (Figure 20A). At week 8 p.i. livers and blood of the infected mice were analysed for various indicators regarding tissue pathology and phenotypic changes in the immune cell composition.

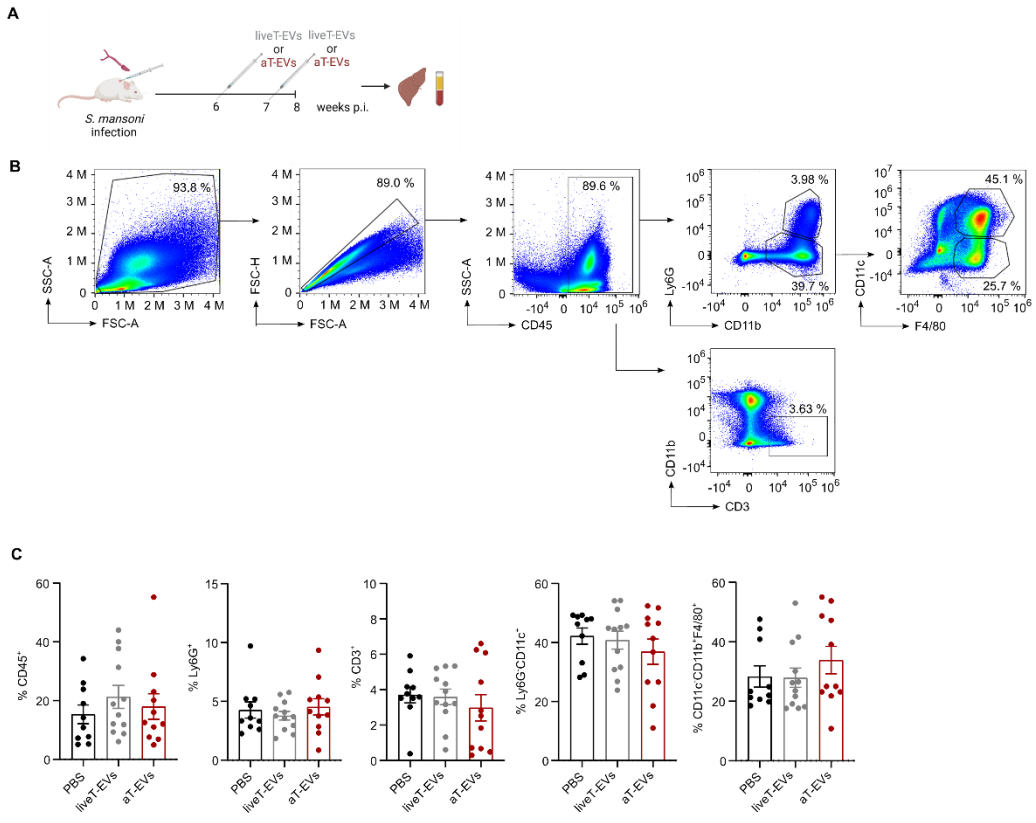


Figure 20: Transfer of liveT- or aT-EVs in *S. mansoni*-infected mice does not influence immune cell composition in the liver. (A) Schematic overview of the experimental setup for the adoptive transfer of T-EVs in *S. mansoni*-infected mice. **(B)** Gating strategy used to identify different immune cell populations in the livers of infected mice. **(C)** Graphs reporting the frequency of different immune cell populations in the liver of S. mansoni-infected mice treated either with PBS, as control, or with liveT- and aT-EV, as reported in (A). Mann-Whitney U test, *P ≤ 0.05 (mean ± SEM).

To define the characteristics of the immune cells, present in the liver of *S. mansoni*-infected mice, hepatic cells were isolated and analysed via flow cytometry. Leukocytes ($CD45^+$), neutrophils ($Ly6G^+$), T cells ($CD3^+$), dendritic cells ($CD11c^+$) and Mϕs ($CD11b^+F4/80^+$) were distinguished via specific gating strategy (Figure 20B). The frequency of the respective immune cell populations comparing mice that

received PBS, liveT-EV or aT-EV transfer is depicted in Figure 20C. Hereby, no significant changes could be detected, even though there might be a tendency towards a higher frequency of CD11b$^+$F4/80$^+$ Mϕs in the liver of mice that received aT-EVs.

Subsequently, phenotypical characterisation of CD11b$^+$F4/80$^+$ Mϕs was performed via flow cytometry.

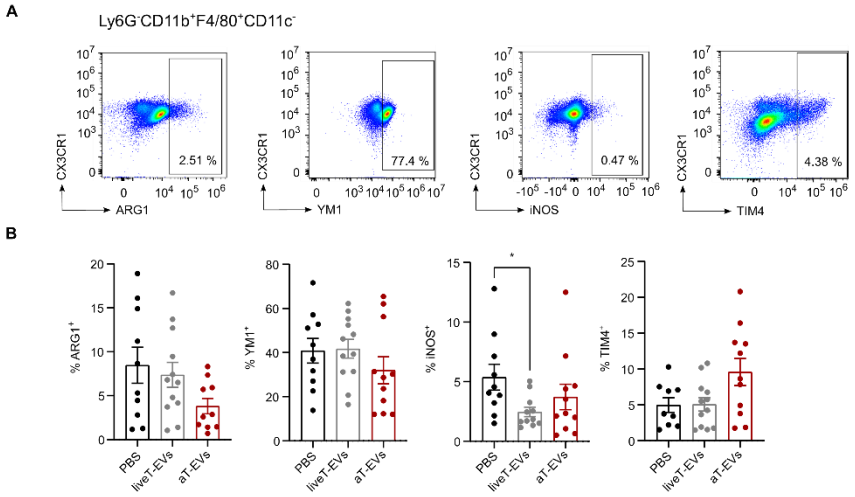


Figure 21: Phenotypic analysis of hepatic Mϕs from *S. mansoni*-infected mice after transfer of liveT- or aT-EVs. *S. mansoni*-infected mice were treated with liveT- or aT-EVs or PBS, as control, at weeks 6 and 7 p.i and liver cells were isolated and stained for flow cytometry 8 weeks p.i. **(A)** Representative dot plots showing the gating strategy for the analysis of various Mϕ markers in the liver of *S. mansoni*-infected mice. **(B)** Bar graphs presenting the quantification of liver Mϕ markers comparing PBS controls to liveT- and aT-EV-treated mice. Mann-Whitney U test, *P ≤ 0.05 (mean ± SEM).

The frequency of ARG1$^+$, YM1$^+$, iNOS$^+$ or TIM$^+$ Mϕs in the previously selected CD11b$^+$F4/80$^+$ population (Figure 21A) was analysed. The frequency of Mϕs expressing ARG1 and YM1 was not significantly different in *S. mansoni*-infected mice that received PBS, liveT-EV or aT-EV transfer (Figure 21B). Interestingly, the frequency of Mϕs expressing iNOS is significantly lower in mice treated with liveT-EVs compared to PBS, whereas aT-EV-treated mice have similar iNOS levels as PBS-treated mice. Furthermore, mice treated with aT-EVs show a trend towards higher expression of the phagocytosis receptor TIM4.

To draw conclusions on the impact of the transfer of liveT or aT-EVs on the disease pathology, parasite eggs were counted in the livers of *S. mansoni*-infected mice and alanine aminotransferase (ALT) levels were measured from their serum (Figure 22).

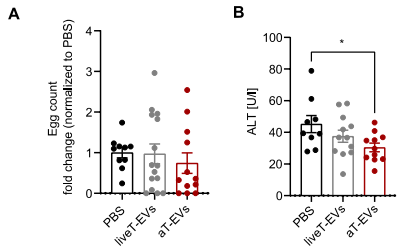


Figure 22: Transfer of liveT- or aT-EVs in *S. mansoni*-infected mice does influence disease pathology. *S. mansoni*-infected mice were treated with liveT- or aT-EVs or PBS, as control, at week 6 and 7 p.i and liver and blood were taken 8 weeks p.i. **(A)** Egg counts from the livers of infected mice treated with PBS, liveT- or aT-EVs (left). Values shown are normalized to the PBS controls. **(B)** ALT levels measured from the blood (serum) of infected mice. Mann-Whitney U test, *P ≤ 0.05 (mean ± SEM).

The egg numbers counted from liver tissue in the liveT-EV and aT-EV-treated mice were normalized to the average of eggs counted in the PBS control to compensate for the high standard deviation occurring naturally in the egg counts of infected mice (Figure 22A). Still, no significant impact of the transfer on the egg burden in the infected mice was detectable. ALT levels, which are an indicator for liver damage, were measured from the serum of infected mice and are detectably lower in mice after aT-EV transfer, compared to mice from the PBS control group. These data suggest that the transfer of aT-EVs might reduce liver pathogenesis in *S. mansoni*-infected mice but does not show an impact on the clearance of eggs from the respective livers.

Liver fibrosis is one of the most pathological consequences of chronic *S. mansoni* infection. Even though mice were sacrificed at week 8 p.i., where the onset of chronic disease is just starting, liver tissues from infected mice were analysed for liver fibrosis indicators.

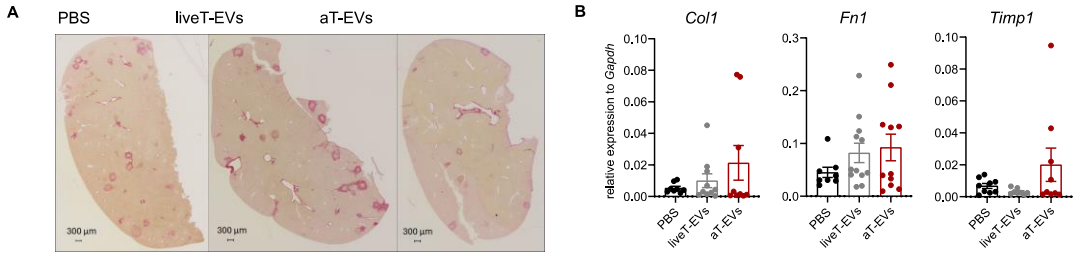


Figure 23: Contribution of liveT- or aT-EVs to liver fibrosis in *S. mansoni*-infected mice. *S. mansoni*-infected mice were treated with liveT- or aT-EVs or PBS, as control, at week 6 and 7 p.i and liver tissue was isolated 8 weeks p.i. **(A)** Representative images of Picrosirius-Red staining of liver tissue. **(B)** mRNA from indicated genes detected in the liver tissue of infected mice by RT-qPCR. Mann-Whitney U test, (mean ± SEM)

Livers of infected mice were histologically stained with Picrosirius Red as an indicator for collagen deposition (Figure 23A). Accumulation of collagen can particularly be observed in the areas of granuloma that have been formed around the trapped eggs. The intensity of the Picrosirius Red seems

higher in the liver of liveT-EV-treated mice, compared to the PBS and aT-EV-treated mice, which might point toward these mice accumulating more collagen deposition.

To investigate if the transfer of liveT- or aT-EVs has an impact on the expression of genes associated to the signalling pathways involved in the development of fibrosis, RT-qPCR was performed from the RNA isolated from the total liver tissue (Figure 23B). Comparing infected mice treated with PBS, liveT- or aT-EVs no significant changes in the expression of *Col1*, *Fn1* or *Timp1* could be detected. This indicates that the reduced liver damage as detected by decreased ALT levels observed upon aT-EV transfer is not linked to fibrosis (Figure 23).

2.5 Liver-EVs isolated from *S. mansoni*-infected mice

Apoptotic thymocytes release different EVs compared to live thymocytes, but their effect on Mϕs phenotype and behaviour seems to be only minor. In order to further understand the role of EVs released by dying cells, a second approach was applied and EVs were isolated from the total livers of *S. mansoni*-infected or naïve mice.

2.5.1 Isolation and characterisation of EVs isolated from the livers of *S. mansoni*-infected or naïve mice

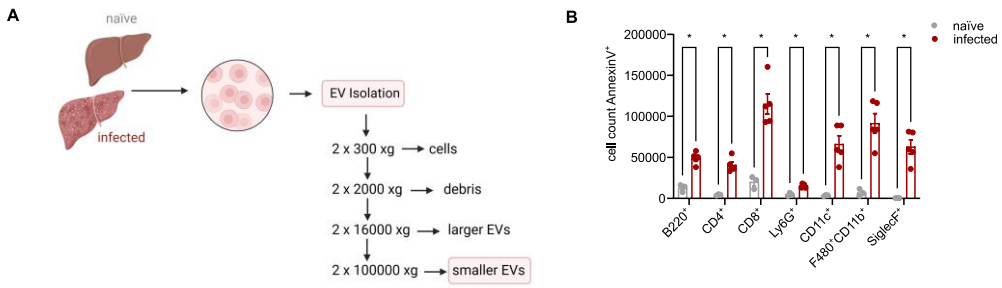


Figure 24: Isolation of EVs isolated from the livers of *S. mansoni*-infected or naïve mice. (A) Schematic overview of the method for the isolation of EVs from the livers of *S. mansoni*-infected or naïve mice. **(B)** Bar graph presenting the cell counts of Annexin V^+ cells within different cell populations in the livers of naïve vs. infected mice. Multiple Mann-Whitney tests, *P ≤ 0.05 (mean ± SEM).

For the isolation of EVs from the livers of naïve and *S. mansoni*-infected mice, liver cells were isolated, brought into suspension and liver-EVs retrieved from cell suspension by differential centrifugation as indicated in Figure 24A. Additionally, liver cells were counted, stained with fluorochrome-conjugated antibodies for their characterisation, and AV staining was performed to determine apoptosis by flow cytometry. The AV^+ cell counts of each population of interest were calculated and are depicted in Figure 24B. The immune cell subsets distinguished by flow cytometry are. AV staining is significantly higher in B cells ($B220^+$), T helper and Cytotoxic T cells ($CD4^+$ or $CD8^+$), Neutrophils ($Ly6G^+$), DCs

(CD11c$^+$), Mϕs (CD11b$^+$F4/80$^+$) and Eosinophils (SiglecF$^+$) isolated from the liver of *S. mansoni*-infected compared to naïve mice. Hence, this suggests that the EVs isolated from the liver are most likely a mixture of EVs released from different cell subsets. Additionally, EVs isolated from *S. mansoni*-infected mice are most likely enriched EVs originating from apoptotic cells compared to EVs isolated from naïve mice.

For the analysis of EV morphology, concentration, and size distribution TEM and NTA were performed (Figure 25).

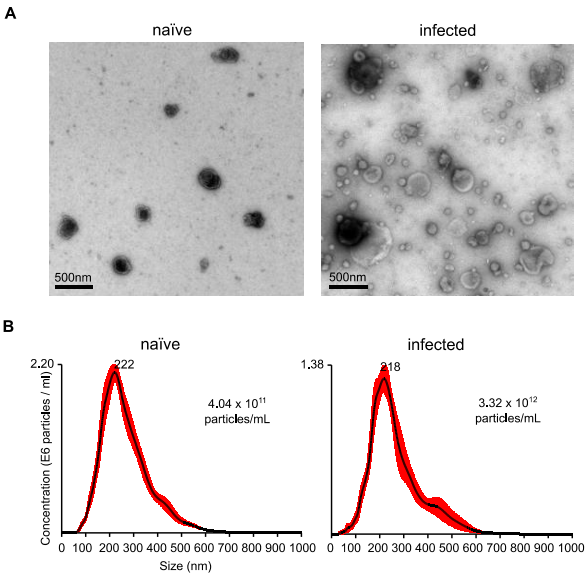


Figure 25: Morphology, size, and concentration of EVs isolated from the livers of *S. mansoni*-infected or naïve mice. (A) Transmission Electron microscopy (TEM) images of EVs isolated from the liver of naïve and *S. mansoni*-infected mice. EV samples were observed under a Tecnai Spirit electron microscope operating at 80 kV and images were recorded with a digital CCD camera (performed by Katharina Höhn, BNITM Hamburg). **(B)** EV samples for Nanoparticle Tracking Analysis were measured using the Nanosight 3000 (Malvern panalytical). Representative graphs show the averaged size and concentration calculated from 5 x 30 sec measurements per sample. Red error bars indicate +/- 1 standard error of the mean.

Immense differences in the morphology of EVs isolated from the livers of naïve or *S. mansoni*-infected mice can be seen in the pictures taken by TEM (Figure 25A). Naïve EVs are a very homogenous population in size (ranging around 200 nm) and their concentration seems much lower compared to the EVs originating from the infected livers. Samples from infected mice contain a broad variety of EVs in different sizes, ranging from 100 to 500 nm. These observations from the TEM pictures can be confirmed via NTA calculating the averaged size distribution and concentration (Figure 25B). The concentration of EVs isolated from a single infected liver is 10 times higher compared to EVs from a naïve liver. Additionally, these show a broader variety in size. In the infected EVs, very small EVs from 50 nm onwards are present, whereas the smallest diameter detected in naïve EVs starts around 80 nm.

The peak of infected EVs is smaller compared to naïve EVs, even though they are also enriched in a large EV population ranging from 400 – 600 nm.

2.5.2 Characterisation of the cargo composition of naïve and infected EVs

As the EVs isolated from naïve or *S. mansoni*-infected show tremendous differences in their morphology, they were further investigated for differences in their surface epitope composition by MACSPlex and flow cytometry.

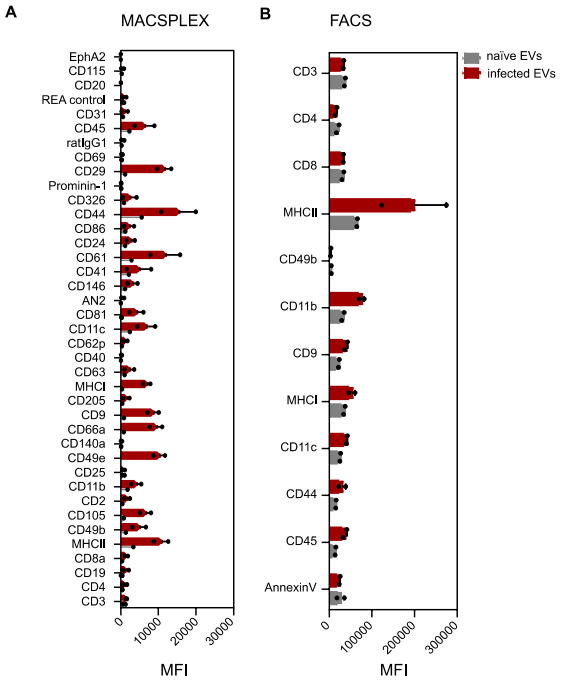


Figure 26: Characterisation of surface epitopes of EVs isolated from the livers of *S. mansoni*-infected or naïve mice. (A) Bar graph presenting the MFI of various surface epitopes in EVs isolated from the liver of naïve and infected mice measured by MACSPlex. **(B)** MFI of selected surface markers from (A) labelled with fluorochrome-conjugated antibodies and measured by flow cytometry. (mean ± SEM).

EVs from the livers of *S. mansoni*-infected mice express multiple of the tested surface epitopes detected by MACSPlex, whilst expression of these markers on EVs from naïve mice seems to be lower or non-detectable (Figure 26A). MHC-I, MHC-II, CD9, CD11b, CD11c, CD29, CD44 and CD45, are amongst the highest expressed markers on infected EVs, similarly to what was observed in aT-EVs, as detected via MACSPlex (Figure 8A). The expression of markers of interest was also confirmed via flow cytometric analysis (Figure 26B). Interestingly, by individual analysis of the single EV marker expression by flow cytometry, most of the tested markers were not differentially expressed between naïve and infected EVs. This again highlights a caveat of the MACSPlex assay, which was already elaborated in chapter 1.2.3., that it allows the detection of a heterogenous bead-bound-EV population but cannot distinguish between individual EVs. Nevertheless, MHC-II and to a minor extent also CD11b are

enriched on the infected EVs. Phosphatidylserine, identified as a reliable EV marker as previously shown (Figure 6), exhibited no differential expression in EVs isolated from both naïve and infected samples, as determined by Annexin V (AV) staining.

2.5.3 BMDMs take up Liver-EVs from naïve mice and *S. mansoni*-infected mice

Liver-EVs were labelled with CFDA-SE to track the uptake of naïve and infected EVs by BMDMs via flow cytometry.

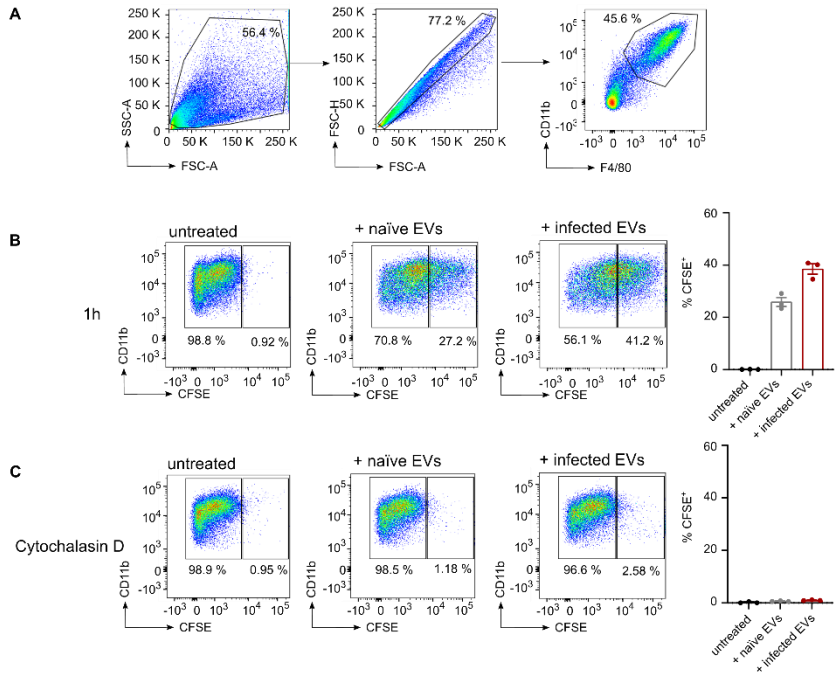


Figure 27: Uptake of CFSE-labelled EVs from the livers of *S. mansoni*-infected or naïve mice by BMDMs analysed by flow cytometry. (A) Gating strategy for the analysis of $CD11b^{+}F4/80^{+}$ Mϕs differentiated from the bone marrow. **(B)** Representative dot plots and corresponding quantification reporting the frequency of BMDMs which have taken up CFSE-labelled Liver-EVs originating from naïve or infected mice after 1 h of co-culture. Untreated refers to BMDMs treated with control buffer. Quantification was performed on three independent samples. **(C)** Mϕs were treated with Cytochalasin D (10 µg/mL) 1 h prior to co-incubation with liver-EVs. Representative dot plots and uptake rates show the frequency of Mϕs which have taken up CFSE-labelled EVS upon 1 h of co-incubation. Mann-Whitney U test (mean ± SEM).

For the identification of $CD11b^{+}F4/80^{+}$ Mϕs, the gating strategy presented in Figure 27A was followed. 40 % of $CD11b^{+}F4/80^{+}$ Mϕs showed uptake of EVs from infected mice, whereas only about 30 % of Mϕs took up EVs originated from the naïve livers (Figure 27B). Blocking the cytoskeleton rearrangement capacity of Mϕs 1 h prior to co-incubation with EVs, inhibits the uptake of both liver-

EVs almost completely (Figure 27D), thus confirming that CFSE$^+$ Mϕs represent a population of cells actively taking up the EVs, rather than simply binding them on the cell surface.

2.5.4 BMDMs upregulate iNOS expression upon uptake of liver-EVs from *S. mansoni*-infected mice

To analyse the effects of the uptake of liver-EVs by Mϕs, BMDMs were harvested after 48 h of co-incubation with the EVs and analysed for changes in protein expression via flow cytometry.

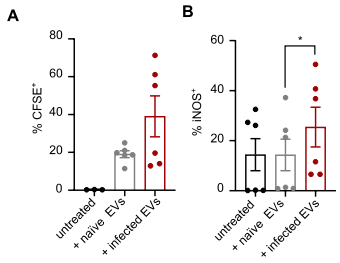


Figure 28: EVs from *S. mansoni*-infected livers induce iNOS expression in Mϕs. (A) Frequency of CFSE$^+$ CD11b$^+$F4/80$^+$ Mϕs after 48 h of co-incubation with CFSE-labelled liver-EVs. **(B)** Frequency of iNOS-expressing Mϕs after 48 h of co-incubation with Liver-EVs. Wilcoxon test, *P ≤ 0.05 (mean ± SEM).

Although the frequency of CFSE$^+$-Mϕs is highly variable between experiments (Figure 28A)**,** the frequency of iNOS expression, is significantly higher after co-incubation with liver-EVs from *S. mansoni*-infected mice, compared to Mϕs treated with liver-EVs from naïve mice. These data indicate that liver-EVs from *S. mansoni*-infected mice might target the nitric oxide pathway in BMDMs similarly to what has been observed when BMDMs were treated with aT-EVs in 2.3.7.

3 Discussion

The release of extracellular vesicles (EVs) is a potent tool for the cells of origin to deliver information to distant target cells and thereby influence the target cells' behaviour and function. When cells undergo apoptosis, they dissemble into apoptotic bodies and increased amounts of EVs are released into the environment. These vesicles were long thought to be non-functional cell junk packaged in smaller portions to be more easily phagocytosed by Mϕs. Conversely, in recent years, increasing evidence has arisen that the uptake of cargo-packed exosomes and apoptotic bodies released during apoptosis by Mϕs might actually contribute to their polarisation status. This study aimed to characterise the morphological differences and the cargo composition of EVs released by live or apoptotic thymocytes, and in turn their effects on the target Mϕs. To this end, Mϕs were analysed for alterations in their phagocytic capacity, transcriptomic signature, and function. In order to further validate, the functional impact of liveT- and aT-EVs, they were transferred into *S. mansoni*-infected mice and analysed for their effect on the disease pathology. Furthermore, EVs were isolated from the livers of *S. mansoni*-infected mice, where parasite eggs accumulate, hence inducing an exaggerated immune response, and triggering the accumulation of apoptotic cells. Liver-EVs from infected mice were also characterised for their cargo composition and for their capacity to regulate the nitric oxide production pathway in Mϕs in comparison to liver-EVs isolated from naïve mice.

The presented results demonstrate that there are differences in the morphology and cargo composition of liveT- and aT-EVs, and even though the impact of these differences on the phenotype, polarisation, and functionality of Mϕs is limited, they might be capable of targeting important cell signalling pathways and of influencing the disease pathology of schistosomiasis to different extents. EVs released during schistosomiasis in the livers of infected mice show a morphology and surface marker composition highly distinct from naïve Liver-EVs and might target similar pathways in the phagocytosing Mϕs as in the case of aT-EVs.

3.1 Characterisation of differences between EVs released from live or apoptotic thymocytes

3.1.1 Cleaved caspase-3 as a cargo of aT-EVs and its possible functions

When comparing EVs released from live and apoptotic cells, an important fact to consider is that their cells of origin consist of a heterogeneous population of live, early apoptotic, and late apoptotic cells. Indeed, the induction of apoptosis in the thymocyte culture increases the proportion of apoptotic cells from roughly 8 % to 47 % (Figure 4B). Therefore, none of the EV populations generated can be considered homogenous. Nevertheless, liveT- and aT-EVs show differences in their morphology and

cargo composition, as apoptotic thymocytes release higher amounts of small EVs compared to live thymocytes. These EVs seem to be generally larger in size, hinting towards the fact that EVs from apoptotic thymocytes might be enriched in apoptotic bodies (Figure 5).

Regarding their cargo composition, a striking finding is that especially smaller aT-EVs are enriched in cleaved caspase-3 content compared to their live counterpart. Previous studies already described that EVs containing caspase-3 are released by cells undergoing apoptosis previous to undergoing any other morphological changes such as the exposure of surface phosphatidylserine[53]. This suggests caspase-3-containing vesicles as an early biomarker for the detection of apoptosis. Transfection of a caspase-3-deficient cell line with caspase-3 shows that activation of ROCK1 via cleaved caspase-3 is crucial for membrane blebbing during apoptosis[144]. These data suggest that ROCK1 could serve as a better marker for EVs specifically released by apoptotic cells, compared to cleaved caspase-3. The membrane blebbing during apoptosis is dependent on caspase-3 and ROCK1, while the release of other membrane vesicles like exosomes is also caspase-3-dependent, but not dependent on ROCK1[144]. Therefore, the presence of ROCK1 in liveT- and aT-EVs should be analysed in future experiments, to better discriminate between apoptotic bodies and other EV subtypes, and potentially to selectively study the impact of apoptotic bodies on immune cell function.

Two key aspects that still remain to be investigated are: First, if cleaved caspase-3 contained in aT-EVs is functional and potentially interacts with signalling pathways via, for instance, induction of apoptosis of the target cells and second, if aT-EVs serve as a shield to protect the environment from caspase activity. Böing and colleagues described that active cleaved caspase-3 contained in the EVs even shows enriched catalytic activity compared to their cells of origin hinting towards the fact that dying cells might be actively sorting caspase-3 into vesicles. Even though small fractions of cells showed signs of early apoptosis such as phosphatidylserine exposure and detachment from the plate, caspase-3-containing EVs were not able to induce apoptosis in significant amounts in their recipient cells in this context[144]. Their data suggest that packaging of cleaved caspase-3 by dying cells might serve as a mechanism of protection of the releasing cells and their environment from active caspase-3.

Sorting of proteins that might have harmful properties into EVs has also been reported in other cases. For instance, astrocytes undergoing amyloid-induced apoptosis have been shown to release EVs containing PAR-4 and C18 ceramide. These EVs were, in turn, able to induce apoptosis via caspase-3 activation in recipient astrocytes independently of the presence of amyloid peptides[145]. The build-up of amyloid-β is known to contribute to Alzheimer's disease, as it is associated with neuronal malfunction and apoptosis[146]. These findings suggest that EVs containing PAR-4 and C18 ceramide contribute to the progression of neurodegeneration during Alzheimer's disease by inducing astrocyte apoptosis. These findings highlight that in-depth characterisation of the proteomic content of live-T

and aT-EV is required to understand the potential interaction between the EV cargo delivery, the functional outcome for the target cell and the potential consequences for disease settings.

Despite its role in apoptosis signalling, caspase-3 has also been found to contribute to non-apoptotic activities, such as auditory brainstem development[147]. Here caspase-3 cleaves extracellular vesicle proteins containing caspase-3 substrates, as EVs in the auditory brainstem. These EVs, by functioning in axon guidance, in turn, influence the formation of the auditory brainstem circuit[147]. Additionally, a large number of RBPs were identified amongst the caspase-3 substrate proteins. RBPs are thought to be involved in the RNA cargo selection process via the incorporation of specific RNAs into EVs as they bind particular RNA recognition motifs[22]. This process suggests the potential of caspase-3 to influence RNA cargo loading into EVs. Overall, caspase activity has been shown to expand beyond the function of apoptosis induction. It is involved in EV formation, release, cargo sorting, and processing, as well as EV uptake[54], hence highlighting the diverse effects that the same protein might exhibit depending on the environmental context and especially their target cells. Therefore, it remains to be clarified if cleaved caspase-3 in aT-EVs is simply a byproduct of the EV biogenesis, serves as a shield to protect the environment from caspase-3-induced apoptosis or interferes with signalling pathways of the recipient cells.

3.1.2 Surface marker composition of liveT- and aT-EVs

Another important factor for communication between EVs and their target cell is the protein expression on the surface of EVs. Therefore, various surface epitopes on liveT- and aT-EVs were detected via MACSPlex and flow cytometry (Figures 6 and 8). On the one hand, these may reflect the identity and polarisation status of the EV-cell of origin, and on the other hand, by being the first inducers of receptor-ligand interaction with target cells, they might be critical for target cell selection as well as important signalling mediators on the target cells. As EVs were isolated from a single cell suspension obtained from total thymus tissue, their originating cells are most probably not exclusively thymocytes, but also thymic epithelial cells and DCs[148]. This is in line with the surface markers, such as CD9, CD11c and the MHC class I and II molecules detected on the EVs.

In general, the surface epitope expression pattern appears to be quite similar between liveT-EVs and aT-EVs. None of the markers tested by MACSPlex or flow cytometry seem to be exclusively expressed on the surface of one or the other sample and might therefore serve as an identifier for EVs released by apoptotic or live thymocytes respectively. Firstly, phosphatidylserine, which is considered a bona fide marker for EVs, as it is required for their formation[149], is abundant on smaller and larger EVs from live and apoptotic thymocytes in fairly similar frequencies (Figure 6). The most striking difference appears in the detection of CD4 and CD8, as the MFI is double as high in the aT-EVs compared to the

liveT-EVs (Figure 8). CD4 and CD8 surely reflect the origin of the EVs from thymocytes and might mediate the interaction between the EVs and cells expressing MHC-II and MHC-I respectively, such as Mϕs or DCs.

Cell adhesion molecules such as CD2, CD41, CD61, and CD146 were found on liveT- and aT-EVs and might be important mediators of initial binding to the target cell surface. Interestingly MHC-I and to an even higher extent MHC-II are present on liveT- and aT-EVs. Both receptors play a crucial role in the selection and development processes of naïve T cells in the thymus, but also once T cells are released into the lymphatic system. Antigens presented on MHC molecules are recognised by the highly specific TCRs and simultaneous binding of the CD4 or CD8 coreceptor to the respective MHC-II or MHC-I molecules induces further maturation of the T cell to effector T cells, memory T cells or regulatory T cells[59]. Former studies suggest that EVs expressing MHC-I or MHC-II receptors on their surface might have the capability of presenting antigens and subsequently contribute to the activation of the immune system. EVs released by tumour peptide-pulsed DCs, for example, expressed MHC-I and MHC-II together with co-stimulatory molecules and were able to prime cytotoxic T-cells and suppress the growth of tumours[150]. MHC-II has been previously reported to be present on thymus-derived EVs before, and these EVs were shown to induce differentiation of regulatory T cells (T regs) in a TGF-β-dependent manner[149]. If and how MHC-II contributes to the T reg induction remains unclear, but data from MHC-II knockout mice suggest that MHC-II is essential for T reg development in the thymus, but not in the peripheral lymphoid organs[151].

3.1.2.1 Technical limitations of surface marker detection on EVs

It is important to highlight a technical limitation of the MACSPlex assay: While detecting a higher MFI in one sample compared to another suggests a higher frequency of EVs positive for a specific marker within that sample, it's essential to note that the total number of EVs may vary between samples. This variation occurs because the same protein concentration was analysed in each sample, which doesn't guarantee an equal number of EVs. Therefore, it remains uncertain whether a higher MFI observed in aT-EVs compared to liveT-EVs simply results from analysing a greater number of aT-EVs, or if the detected molecule is genuinely more abundant on aT-EVs compared to liveT-EVs.

Additionally, the MACSPlex is a bead-based assay, which implies that all EVs expressing a surface epitope bind to an epitope-specific population of beads, and the fluorescence intensity becomes higher the more EVs are bound to the beads, but not the more molecules are present on the surface of a single EV. Therefore, MACSPlex is a useful method to determine the presence of a broad variety of surface epitopes, but validation via flow cytometry is necessary to draw quantitative conclusions. However, flow cytometric analysis of EVs also brings some caveats, for example, the detection is

restricted to EVs larger than 160 nm in size because smaller EVs could not be distinguished from the background noise (Figure 9). Additionally, detection by flow cytometry requires a minimum signal of fluorescence intensity, hence if insufficient numbers of epitopes and in consequence, fluorochrome-labelled antibodies are present on an EV surface, that epitope might not be detected at all. This caveat can be overcome by using bead-based assays. Nevertheless, the MFI of CD4 and CD8 is also higher when measured by flow cytometry confirming that it is more abundant on aT-EVs compared to liveT-EVs. Other surface epitopes present on liveT- and aT-EVs that might reflect the identity of originating cells are, for example, the leukocyte marker CD45, the T cell activation marker CD44, and the cytotoxic T cell activation marker CD29. However, whether these surface markers are involved in target specificity and receptor-ligand interaction remains to be investigated.

3.2 Modulatory effects of liveT- and aT-EVs on Mϕs

3.2.1 Mϕs phagocyte EVs from live and apoptotic thymocytes

The uptake of liveT- and aT-EVs was shown to occur in two different types of Mϕs: Mϕs differentiated *in vitro* from the bone marrow and Mϕs isolated from the peritoneal cavity of mice undergoing peritonitis (Figures 10 and 12). Interestingly, inhibition of cytoskeleton rearrangement by Cytochalasin D blocks the uptake of EVs by BMDMs (Figure 10D), suggesting that the main route of uptake is not a passive fusion of membranes, but active uptake via, for instance, phagocytosis that requires actin polymerisation.

In order to characterise differences between Mϕs that would uptake or not uptake EVs, liveT- and aT-EVs were labelled with CFSE (Figure 9) to trace their uptake by Mϕs via flow cytometry. BMDMs incubated with liveT-EVs show an almost identical phenotypical profile compared to BMDMs incubated with aT-EVs (Figure 11C) suggesting that both, liveT- and aT-EVs, are taken up by the same population of phagocytically active Mϕs. Of note, *in vivo* liveT- as well as aT-EVs were exclusively taken up by a population of $TIM4^+$ large pMϕs in the peritoneal cavity (Figure 12D). $TIM4^+$ large pMϕs showed quite a distinct phenotypic profile compared to BMDMs, as almost no differences between $CFSE^-$ and $CFSE^+$ pMϕs in the expression of the markers analysed were detected (Figure 13B). $TIM4^+$ large pMϕs are considered the tissue-resident Mϕs in the peritoneum with the main function of maintaining tissue homeostasis by rapid and efficient clearance of apoptotic cells. Therefore, it seems rational that they are also more prone to take up aT-EVs than small pMϕs. Upon microbial stimulation, $TIM4^+$ large pMϕs can respond rapidly and induce the recruitment of other innate immune effector cells to the intestinal lamina propria to support local intestinal immunity[152]. So far, upon uptake of aT-EVs, no alterations in the phenotype of pMϕs could be detected, hence suggesting no impact of EVs on their immunological function. Eventually, further experiments should be conducted in other disease contexts, such as

colitis. Intriguingly, the transfer of aT-EVs has been described to contribute to the amelioration of colitis. Here, aT-EVs containing phosphatidylserine and FOXO3 promote TGF-β production by Mϕs, hence initiating their anti-inflammatory polarisation, which in turn inhibits Th1 differentiation and promotes the induction of regulatory T cells[106].

3.2.2 Impact of EV uptake on Mϕs phagocytic capacity

In other contexts, EVs have already been shown to influence the phagocytic capacity of Mϕs. EVs derived from colorectal cancer patients, for example, enhance the phagocytic capacity of Mϕs in the tumour environment by engagement of the scavenger receptor MARCO. Enhanced clearance of apoptotic cells in the tumour microenvironment, in turn, results in anti-inflammatory polarisation of the Mϕs and thereby creates a pro-tumour environment[153]. Because of the high phagocytic receptor expression in $CFSE^+$ Mϕs, the concluding hypothesis arose that liveT- and aT-EVs might be efficiently taken up by phagocytically active Mϕs and alter their capacity to further phagocytose additional apoptotic cells. However, no difference in the capacity of Mϕs to phagocyte apoptotic thymocytes was detected when BMDMs were previously treated with liveT- or aT-EVs compared to untreated BMDMs (Figure 14C).

Yet, $CFSE^+$ Mϕs showed significantly higher uptake of apoptotic thymocytes compared to $CFSE^-$ Mϕs *in vitro* and *in vivo* (Figure 14D and 15B). Additionally, significantly higher expression of the phagocytic receptor MERTK and of MHC-II was detected in the $CFSE^+$ large pMϕs compared to $CFSE^-$, when pMϕs were harvested 4 h after aT-EV injection (Figure 15C), but not 24 h after injection (Figure 13B). This again highlights the plasticity of Mϕs and their capacity to rapidly adapt to their environment, and that the chosen time point of analysis is a crucial factor to be considered when conclusions are drawn. The engagement of phagocytic receptors observed in $CFSE^+$ Mϕs might still be of interest as it has not only been described to enhance Mϕs phagocytosis but also to be linked to their proliferation[154]. Even though the EVs do not directly influence the phagocytic capacity in our context, they might be seen as a useful tool to specifically target phagocytically active Mϕs and selectively deliver cargo. Therefore, the surface epitopes that allow EVs to specifically interact with phagocytically active Mϕs should be identified. Phosphatidylserine might be a candidate, as it is present on both liveT- and aT-EVs and has the potential to interact with phosphatidylserine recognition receptors on Mϕs. The binding of phosphatidylserine to these receptors, such as TIM4 and MERTK, activates various signalling pathways, with the most prominent being associated with the induction of efferocytosis. The role of phosphatidylserine in target cell specificity could be investigated by adding Annexin V to the EVs before giving them to Mϕs. Annexin V will bind to phosphatidylserine and thereby block the interaction of the

EV with the respective receptors on the target cells. Additionally, the involvement of other EV surface markers in the targeting of phagocytically active Mϕs should be considered.

The development of new treatments for various infectious diseases is emerging mainly due to the rise of drug resistance. Engineering EVs as tools for drug delivery is a growing field of interest, as they hold the potential to overcome these challenges with a new form of targeted delivery[155,156]. The most advanced studies on engineering EVs are developed for cancer treatments with numerous preclinical studies and clinical trials already ongoing[157]. Hereby, EVs seem to be promising candidates for drug delivery as they improve efficacy by their enhanced capacity to penetrate through blood vessels and across biological barriers compared to free formulations of drugs. Packaging of anti-cancer drugs into EVs also reduces their systemic toxicity, as the compound is only released once the target site is reached. Indeed, EV surface molecules can be engineered to direct the cargo delivery towards specific targets and thus enhance efficiency[158]. Therefore, elucidating the characteristics of surface molecules on liveT- and aT-EVs that preferentially interact with phagocytically active Mϕs might be of interest for cargo delivery selection. Indeed, specifically targeting phagocytically active Mϕs for drug delivery or targeted polarisation using EVs might be feasible for novel therapeutic strategies. For instance, this approach might be applicable in anti-cancer treatment by directing cargo-loaded EVs towards cells expressing phagocyte receptors and costimulatory molecules. The cargo could be designed to either induce apoptosis in tumour associated Mϕs, known to create a pro-tumour environment and contribute to metastasis, or to polarise Mϕs towards effective phagocytosis and degradation of cancer cells[159].

In general, the therapeutical use of EVs is suggested to have the potential to overcome clinical difficulties as they harbour diverse biomolecule cargos that are bio-engineerable with the ability to elicit potent cellular responses and to cross biological barriers and their production is suggested to be applicable for large-scale[160]. For further development of engineered EVs, the basic understanding of EV cargo composition and the molecular mechanisms underlying target specificity and most importantly functional consequences of cargo delivery of naturally occurring EVs are fundamental.

3.2.3 Transcriptomic and functional alterations in Mϕs treated with liveT- or aT-EVs

To reveal insightful information on the effects of EV uptake on the transcriptomic level, bulk mRNA sequencing was performed on BMDMs treated with liveT- or aT-EVs for 24 h. EVs from live or apoptotic thymocytes induce differences in gene expression levels in the target BMDMs (Figure 16A). *Nos2*, the gene encoding for inducible nitric oxide synthase (iNOS), *Cish*, a member of the Suppressor of cytokine signalling (SOCS) family and *SerpinB2*, encoding for the plasminogen activator inhibitor type-2 were among the highest differentially expressed genes between the two conditions analysed (Figure 16A).

These genes also showed a tendency towards higher expression levels in aT-EV-treated BMDMs compared to liveT-EV-treated BMDMs when analysed via quantitative real-time PCR (Figure 17).

Genes that were higher expressed in aT-EV-treated BMDMs compared to liveT-EV-treated were linked to biological processes such as biosynthesis of nitric oxide, nitric oxide metabolic processes and arginine catabolic processes (Figure 16B) as detected via gene ontology (GO) term analysis. In line with the upregulation of nitric oxide-related pathways in aT-EV-treated BMDMs, Kyoto Encyclopedia of Genes and Genomes (KEGG) pathway analysis, shows that genes upregulated in liveT-EV-treated BMDMs are mainly involved in the competing arginine and proline biosynthesis pathway (Figure 16C). ARG1 and iNOS both compete for the substrate L-Arginine, which is needed for proline synthesis in ARG1-dependent pathways but is also required for the production of NO and other ROS species via iNOS activation[79,88].

3.2.3.1 Modulation of the nitric oxide pathway in Mϕs

Given the sequencing and the RT-qPCR results, protein expression of iNOS and subsequent NO production were analysed. Interestingly, BMDMs treated with aT-EVs show upregulation of iNOS compared to liveT-EV-treated BMDMs, but no difference in the concentration of nitrate released to the supernatant could be detected using the Nitric Oxide Assay Kit (ThermoFisher Scientific) (Figure 18). To be noted, gene expression, protein expression and nitrate concentration were all measured after 24 h of co-incubating BMDMs with the EVs. Hence, the time point of analysis might be a critical point to be adjusted in future experiments. Additionally, the tested supernatants showed high concentrations of nitrate exceeding the detection limit of the assay and plotted values were calculated from the mathematically extended standard curve. Even though the assay was chosen and performed according to the guidelines for measuring reactive oxygen species and oxidative damage in cells and *in vivo*[161], the results might require validation using alternative techniques such as a luminol-based assay. The molecular mechanism causing higher iNOS expression in aT-EV-treated BMDMs remains to be investigated. To define the specific cargo of aT-EVs that can interfere with the gene expression pathway of *Nos2*, bioinformatic analysis of the protein and miRNA content should be performed and subsequent pathway analysis of the aT-EV content might reveal candidate proteins or miRNAs.

It is tempting to speculate that specific miRNA exclusively contained by aT-EVs, might be driving the induction of iNOS in the target Mϕs, as miRNAs have been reported to promote pro-inflammatory polarisation of Mϕs in other settings. In a model of myocardial reperfusion, for instance, EVs, have been reported to deliver miRNA-155 to recipient Mϕs, which interferes with the JAK/STAT1 signalling pathway, thus promoting pro-inflammatory polarisation of Mϕs[162]. In fact, deficiency of miRNA-155 in a mouse model of acute myocardial infarction, improved cardiac function. This mechanism is

suggested to be mediated by EVs containing miRNA-155, derived from Mϕs. When taken up by fibroblasts, these Mϕ-derived EVs suppressed their proliferation and promoted inflammation by downregulating *Socs1* via miRNA-155[163]. In other contexts, miRNA-155 has also been reported to target *Socs1* and thereby interfere with important STAT signalling pathways, leading, for example, to increasing the inflammatory response of Th17 cells in acute pancreatitis[164]. Interestingly, *Cish*, a member of the SOCS family, was another highly expressed gene in aT-EV-treated Mϕs. SOCS proteins are suppressors of pro-inflammatory cytokine signalling and therefore associated with being expressed by anti-inflammatory Mϕs. This is also highlighted in the studies mentioned above that report *Socs1* downregulation in line with the pro-inflammatory polarisation of the Mϕs[163]. In contrast, our results show that *Nos2* and *Cish* are upregulated simultaneously. It is known that upon excessive inflammation, a negative feedback regulation of Mϕs is induced [165]. Thereby, excessive production of NO, via a negative feedback loop, limits the pro-inflammatory capacity of Mϕs. This process, in our experimental setting, might be accompanied by the expression of *Cish* to suppress pro-inflammatory cytokine signalling. Therefore, it would be highly intriguing to dissect whether miRNA-155 might also be abundant in aT-EVs and contribute to their modulating effect on Mϕs.

These findings highlight the importance of identifying the specific cargo and molecular mechanism by which the uptake of EVs alters the signalling of recipient cells. Packing the inducer of iNOS into EVs that specifically carry surface molecules to target Mϕs might prevent off-target effects in other cell types.

3.2.3.2 The influence of EVs on Mϕ cytokine signalling and tissue repair functions

As the upregulation of *Socs* genes is directly linked with the suppression of cytokine signalling, the concentration of selected cytokines released by live-T- or aT-EV-treated BMDMs was measured in the supernatant after 24 h of co-culture (Figure 19C). In general, most cytokines measured were only present in very low concentrations. Only TNF-α and IL-10 were secreted in higher amounts but no differences in their amount between liveT- and aT-EV-treated BMDMs were detected. To measure the effects of soluble factors released by BMDMs upon uptake of liveT- or aT-EVs on fibroblast migration, the supernatants secreted by liveT- and aT-EV-treated BMDMs were transferred to fibroblast cell cultures (Figure 19D). No difference in the capacity of fibroblasts to migrate towards a scratch was detected independently if the transferred supernatant was generated from untreated, liveT-EV- or aT-EV-treated Mϕs. Cytokines and growth factors released by Mϕs, such as TGF-β, and IL-6, but also TNF-α and IL-10 are sensed by fibroblasts and contribute to their activation[166,167]. In line with the fact that no differences in cytokine release were detected in liveT-EV and aT-EV-treated BMDMs, we could not expect any cytokine-mediated effect on fibroblast migration and activation. Yet, the function of Mϕs to initiate fibroblast activation and migration plays a crucial role in tissue regeneration and wound

healing. Therefore, investigating further if and how EVs might contribute to intercellular communication between Mϕs and fibroblasts might be of interest. Especially considering that in chronic diseases, for example, chronic schistosomiasis, this crosstalk can contribute to the development of fibrosis[124].

Other studies have described EVs derived from mesenchymal stem cells (MSCs) undergoing apoptosis as contributors to tissue regeneration by regulation of cell death processes in various models of tissue damage. In muscle injury, for example, MSCs-ApoEVs increased the apoptosis rate of myoblast causing increased ApoEV release of the myoblasts respectively. These EVs, in turn, promoted myoblast fusion and thereby wound healing[52]. In type 2 diabetes MSC-ApoEVs were shown to promote the healing of skin injury likely mediated by reducing oxidative stress levels and thereby inhibiting Mϕ cell death through pyroptosis[168]. MSC-Apo-EVs have been shown to express Fas-Ligand on their surface and can thereby induce apoptosis in multiple myeloma cells leading to an extended life span of multiple myeloma mice[169]. Importantly, whereas smaller Apo-EVs promoted cell proliferation, enhanced angiogenesis, and stimulated the polarisation of anti-inflammatory Mϕs, thereby facilitating tissue regeneration and wound healing in a model of skin damage, apoptotic bodies were inhibiting these functions. Proteomic and transcriptomic approaches have been performed to identify differentially expressed proteins and genes between apoptotic bodies and smaller Apo-EVs. GO term and KEGG pathway analysis revealed that highly expressed proteins and genes in smaller ApoEVs are associated with cell adhesion and cell migration, most likely via regulation of TGF-β, *Wnt* and MAPK pathways[170]. As all functional experiments in this thesis were carried out with a pool of smaller and larger EVs containing apoptotic bodies, their effect might be underestimated due to their heterogeneity. Therefore, to dissect their impact on target cells more deeply, fraction separation should be performed. Clarification, if aT-EVs might share some of the identified cargos and functional properties, involved in tissue repair discovered in MSC-ApoEVs, requires further investigation of their RNA and protein content. Interesting to note is that none of the studies mentioned above compared the effect of ApoEVs to EVs isolated from live cells. As we aim to compare the changes occurring in the EV composition upon apoptosis induction, EVs released from the live cell counterpart were always used as controls.

3.2.3.3 *SerpinB2* expression and its consequences in schistosomiasis

Another gene that was highly expressed by BMDMs treated with aT-EVs, but not liveT-EVs, is *SerpinB2* (Figure 16). SerpinB2 is an inhibitor of the urokinase plasminogen activator, which is involved in various immunological processes including migration, adhesion, differentiation, proliferation, and apoptosis. SerpinB2 is often upregulated in inflammatory disease and abundantly expressed by activated Mϕs. Polymorphisms or dysregulated expression of SerpinB2 is associated with several human inflammatory

diseases all linked to imbalanced type 1 and/or type 2 responses such as myocardial infarction, peritonitis, and Alzheimer's disease[171]. In large pMϕs *SerpinB2* expression promotes their conversion toward a resolution phase signature[172]. Large pMϕs expressing *SerpinB2* showed inhibited migration capacity compared to *SerpinB2*-deficient cells and adoption of a resolution phase signature, in line with their contribution to tissue repair. SerpinB2 expression was found to be drastically higher in the granulomatous livers of *Schistosoma japonicum*-infected mice compared to uninfected controls[173]. Further investigation in mice with *SerpinB2* deficiency revealed that egg burden and granuloma number in infected mice were unaffected. Yet, granulomas showed reduced signs of fibrosis assessed by Sirius red staining and increased iNOS, IL-6, IL-10 and TNF-α and decreased Arg1 and IL-13 mRNA expression compared to wildtype mice. When immunized with SEA, *SerpinB2*-deficient naïve mice showed reduced capacity to produce SEA-specific IgG1 antibodies. Taken together, this study conducted in *SerpinB2*-deficient mice suggests SerpinB2 as a promotor of certain type 2 responses, while it might inhibit type 1 responses in the context of *Schistosoma* infection. These data however have not been reconducted to Mϕs directly. Nevertheless, deficiency of *SerpinB2* results in enhanced CD40 signalling, which is associated with promoting TNF-α, iNOS and IL-6 expression and type 1 responses[172,174]. Taken together, *SerbinB2* was differentially expressed between liveT- and aT-EV-treated BMDMs and the data discussed above suggest *SerpinB2* as a regulator of the immune response and contributor to schistosomiasis pathology. The impact of liveT- and aT-EVs during *S. mansoni* infection has been investigated and will be discussed in the following chapter.

Altogether the data from transcriptomic analysis of liveT-EV- and aT-EV-treated BMDMs suggest that the uptake of aT-EVs modulates the expression of genes, involved in the development of a more pro-inflammatory signature by interfering with nitric oxide production, cytokine signalling and possibly modulation of the type 1/type 2 immune response. Yet, only targeting of the nitric oxide pathway could be proven on protein level, whereas the other suggested pathways could not be proven to have consequences on the Mϕ function in cytokine signalling or tissue repair experimentally.

3.3 Impact of liveT- and aT-EV transfer on schistosomiasis pathology

Even though a functional link between aT-EV-treated Mϕs and their tissue-remodelling capacity could not yet be drawn *in vitro*, our findings suggest that aT-EVs promote signalling pathways in Mϕs that might be relevant for the disease outcome of schistosomiasis. Granuloma formation around trapped eggs in the liver, immune cell infiltration and activation, high occurrence of cell death and the polarisation of Mϕs in response to the phagocytosis of dying cells are critical factors for the disease pathology.

Infiltration of immune cells to the liver triggered by the immunogenic eggs is crucial for the formation of granuloma and for disease progression in *S. mansoni* infection. Upon adoptive transfer of liveT-EVs, aT-EVs or PBS, as control, analysis of the immune cell composition reveals no significant difference in the frequency of the immune cells, but only a tendency towards higher frequency of $CD11b^{+}F4/80^{+}$ Mϕs in the liver of aT-EV-treated mice, compared to liveT-EV-treated or control mice (Figure 20). Deeper phenotypic analysis revealed that in mice treated with liveT-EVs, significantly lower frequencies of hepatic Mϕs expressing iNOS are present, compared to controls (Figure 21). Studies conducted in rats, show that iNOS is critical for the initiation of an efficient Th2 response. In the absence of iNOS, their type 2 response is impaired leading to slower clearance of parasites and the development of granuloma formation and fibrosis, suggesting iNOS as a potent anti-inflammatory and antifibrotic mediator in the context of schistosomiasis[175,176]. In line with these data, higher iNOS expression is associated with improvement in liver pathology, as suggested by lower serum ALT levels in infected mice that received aT-EVs transfer compared to PBS controls (Figure 22B).

No significant differences but a tendency towards lower frequencies of $ARG1^{+}$, $YM1^{+}$ and higher frequency of $TIM4^{+}$ of hepatic Mϕs was detected when infected mice received aT-EV transfer compared to PBS or liveT-EVs (Figure 21). Surely, more samples would be needed to validate these tendencies but these data would suggest that the transfer of aT-EVs might influence the abundance of anti-inflammatory and phagocytically active Mϕs in the livers of infected mice. Anti-inflammatory Mϕs have been shown to have a dual role during schistosomiasis. Anti-inflammatory Mϕs, characterised by the expression of ARG1 and YM1, are critical for the host survival by preventing an excessive and lethal type 1 response but simultaneously contribute to collagen synthesis and fibrogenesis and in consequence disease pathology[127,128]. The role of ARG1 in schistosomiasis pathogenesis is fairly well understood, as it is involved in the metabolic process of converting the substrate L-Arginine to proline which is needed for collagen synthesis[128], whereas the contribution of YM1 remains less clear. $Ym1^{+}$ Mϕs are found in close proximity to parasite eggs[177] and YM1 released by neutrophils has been shown to digest glycosaminoglycans, which are highly abundant in hepatic granulomas, supporting the hypothesis that it might contribute to the killing of parasite eggs[178,179]. Nevertheless, these mild alterations in the Mϕ composition did not lead to alterations in the egg burden in the livers of infected mice, which is one of the main indicators for the disease severity (Figure 22A). Yet, slightly reduced expression of ARG1 and YM1 in the hepatic Mϕs might contribute to lower liver damage, as ALT levels detected in the serum of mice were significantly lower when mice were treated with aT-EVs compared to mice treated with PBS as control (Figure 22B). ALT is normally found inside hepatocytes but is released into circulation upon hepatocyte damage[180]. Hence, lower ALT levels suggest that the transfer of aT-EVs reduces liver pathogenesis compared to the transfer of liveT-EVs or PBS.

These data indicate that granuloma formation around trapped eggs in the liver might, to some extent, be disentangled from hepatocyte damage. Data from patients with chronic liver disease show that ALT levels need to be evaluated critically, as ALT levels don't necessarily match the disease severity and collagen deposition[181]. Hence, lower ALT levels detected in aT-EV-treated compared to PBS-treated mice might indicate lower acute hepatocyte damage, but not necessarily lower fibrosis severity. Therefore, additional readouts should be considered to validate the influence of aT-EV transfer on the development of fibrosis.

In the histological staining of representative liver sections with Picrosirius Red, sections from liveT-EV-treated mice seem to have more collagen accumulation in the granuloma, as indicated by the deeper red colour, compared to sections from aT-EV- or PBS-treated mice (Figure 23A). To confirm these observations with a more quantifiable method, the expression of selected genes associated with fibrosis development has been measured in the liver tissue. Collagenase 1 encoded by *Col1*, is an enzyme involved in the degradation of collagen. Fibronectin (*Fn1*) is an extracellular matrix protein required for collagen matrix assembly and therefore its abundance is linked to fibrotic progression[182]. Tissue inhibitor of matrix-metalloprotease-1 (*Timp1*) inhibits the degradation of ECM and thereby contributes to fibrosis development[183]. No significant difference in the expression of the selected genes was detected in aT-EV-treated mice, compared to liveT-EV- and PBS-treated mice, indicating that fibrosis is not linked to the reduced liver damage as detected by decreased ALT levels observed upon aT-EV transfer (Figure 23B). As livers and blood were only analysed at 8 weeks p.i. where the onset of chronic disease with the first signs of collagen deposition is just emerging, later time points should be analysed as well to reveal the effects of EV transfer on chronic fibrosis development.

Taken together, the transfer of aT-EVs might contribute to the reduction of hepatocyte damage, even though no significant alterations in the egg count, granuloma composition or collagen deposition were found. Multiple publications have already described molecular mechanisms of how EVs might influence hepatocytes and thereby fibrogenesis. During liver fibrosis development, EVs released by host cells have been shown to be more prone to contribute to the disease progression, but in contrast, treatment with EVs has been shown to have anti-fibrotic properties[184]. EVs released by hepatocytes containing MSP1, activate HSCs, increasing the production of collagen, desmin, and α-SMA and thereby contributing to fibrogenesis[185]. Highlighting the therapeutic potential of EVs in fibrosis treatment, researchers succeeded in identifying miRNAs that harbour promising therapeutic potential when delivered via extracellular vesicle transfer. MSC-EVs derived from adipose tissue were engineered to overexpress miRNA-181-5p, which targets the STAT3/Bcl-2/Beclin 1 pathway in HSCs and, in turn, attenuated liver injury and significantly down-regulated production of collagen, vimentin, α-SMA and

fibronectin in the liver[186]. If aT-EVs might carry MSP1 or miRNA-181-5p as potential cargos to directly target hepatocytes and thereby reduce liver damage is planned to be investigated in the near future.

The therapeutic potential of EVs specifically derived from apoptotic cells has been less extensively studied than the potential of EVs derived from live cells but still suggests promising protective and regenerative effects. In the context of liver disease, MSC-derived ApoEVs have been shown to reach the liver upon i.v. transfer. Here they are internalised by hepatocytes and functionally assemble with the recipient cell's Golgi apparatus. Thereby they have been shown to promote liver regeneration after partial hepatectomy and mediate protection against acute liver failure[187]. Even though their mode of action remains to be elucidated, these findings highlight that Apo-EVs harbour great therapeutic potential in liver disease by targeting hepatocytes.

Hepatocytes are not the only target cells of Apo-EVs, as HSCs have been shown to take up apoptotic bodies derived from hepatocytes. The uptake improved HSC survival by inducing JAK/STAT-mediated activation of the PI3K/Akt/NF-κB cascade mediating survival signalling[188]. Survival of activated HSCs producing ECM components and TGF-β is an important factor in the propagation of liver fibrosis and thereby, specific targeting of HSC apoptosis might allow the development of therapeutic strategies in the reversal of fibrosis.

Apoptotic bodies specifically, are a promising tool to envelope specific cargo and deliver it to Mϕs, as they are rapidly taken up by phagocytes and act as a messenger between damaged cells and the immune system during homeostasis and disease[189]. Thereby the therapeutic use of apoptotic bodies may cause less off-target effects compared to healthy cell-derived EVs and other immunotherapy approaches[190]. Yet, there are only a few approaches published that highlight the potential of apoptotic bodies for clinical use so far. For example, APCs that have phagocytosed apoptotic bodies derived from colorectal cancer cells exhibited anti-tumour functions when injected into tumour-bearing rats. In parallel APCs that have phagocytosed EVs from non-apoptotic cells did not affect the disease outcome[191].

Taken together, our findings highlight that aT-EVs harbour the potential to reduce liver damage, potentially via modulation of signalling pathways upon uptake by hepatic Mϕs or hepatocytes. Yet, deeper analysis is required to fully elucidate the therapeutic potential of EVs derived from apoptotic as well as live cells and that the understanding of their cargo composition and the molecular mechanisms of communication between EVs and their target cells are crucial for the development of new therapeutic approaches as described in chapter 4.

3.4 Characterisation of liver-EVs isolated from naïve or *S. mansoni*-infected mice

During schistosomiasis, host- and parasite-derived EVs are released, which are both suggested to play a crucial role in intercellular communication during disease progression, thereby influencing the disease pathology[192]. Granuloma formation occurs in response to immunogenic parasite egg deposition in the liver triggering a strong type 2 immune response which peaks around 8 weeks p.i., and in turn results in the accumulation of apoptotic cells (Annexin V^+) in the livers of infected mice (Figure 24B). Morphological analysis of EVs isolated from the livers of *S. mansoni*-infected mice confirms that they are a very heterogeneous population, enriched in smaller EVs as well as apoptotic bodies, compared to EVs isolated from the livers of naïve mice (Figure 25). Interestingly, liver-EVs derived from *S. mansoni*-infected mice show a very high abundance of various surface epitopes, suggesting that they originate from a great variety of cell types (Figure 26). Similarly to liveT-EVs and aT-EVs, liver-EVs are taken up by Mϕs and co-incubation of liver-EVs from infected mice causes an increase in the frequency of $iNOS^+$ Mϕs compared to liver-EVs from naïve mice (Figure 27 and 28). *Nos2* gene expression in Mϕs can be induced via multiple pathways, for example, via IFN-γ-R and STAT1, TLR4 and NF-κB, TLR4 and AP1 or cytokine receptors and AP1[193] (Figure 2). If one of the cargos contained by aT-EVs or infected liver-EVs interferes with one of these pathways and thereby causes upregulation of iNOS expression remains to be investigated. As well as examination, if liver-EVs also mediate the upregulation of iNOS in Mϕs during schistosomiasis *in vivo* and how this might influence the disease progression. Transfer of iNOS-expressing pMϕs in *S. japonicum*-infected rats deficient for iNOS leads to the blocking of parasite growth, reproductive organ development, and egg production during the acute phase of the disease[175,194]. Hence, specific cargos contained in aT-EVs or liver-EVs might be iNOS inducers and using them as triggers of a targeted increase in iNOS expression might be beneficial for the host.

Polarisation of anti-inflammatory Mϕs to a certain extent is crucial to counteract an excessive Th1 immune response that might be lethal for the host. At the same time, anti-inflammatory Mϕs might contribute to the development of fibrosis in the long run. Considering this, finding tools to specifically commit Mϕs towards the acquisition of the different polarisation states might allow to alter the disease progression[195]. Once liver fibrosis has developed, there is potential for reversibility if the source of the initial liver injury is completely removed[196]. In schistosomiasis, treatment with praziquantel administered 7 weeks p.i. to clear the host from adult worms, has been shown to be an effective inducer of liver recovery[197]. Even if treatment was initiated 10 or 20 weeks p.i., mice recovered from liver fibrosis 2 – 3 months later with only residues of scar tissue remaining[198]. This is especially relevant in the endemic areas, where the disease is often only recognised at the chronic stage when the onset of fibrosis has already begun[199]. Preventive chemotherapy, where at-risk populations especially

children receive a regular single dose of praziquantel, regardless of their infection status, has been implemented by the WHO to counteract the high schistosomiasis morbidity[200]. Mass application of praziquantel helped to reduce schistosomiasis prevalence, especially amongst school children but surely contributes to the risk of increased resistance development[201]. Given this, the development of new treatment options for schistosomiasis and for a variety of additional diseases is crucial. EVs seem to be a promising alternative for more specified and targeted drug delivery, but also as bioactive components themselves, whether in their native state or engineered to the specific needs[32].

An alternative approach to reducing the prevalence of schistosomiasis is the development of vaccination strategies. Immunisation of mice with irradiated cercariae, or inactivated schistosomula, has already been shown early in the beginnings of schistosomiasis research to be highly effective in mediating protection against infection. Also here, the risk of adverse events would potentially be too high to be applied clinically[202,203]. However, these preliminary studies opened the path for the investigation of specific antigens that might be capable of mediating protective immunity. In the following years, several vaccinations have been developed consisting of antigens, for example, the *S. mansoni* fatty acid binding protein (Sm14) or *S. mansoni* tetraspanin (Sm-TSP-2) are currently undergoing safety, immunogenicity and efficacy testing in clinical trials[204,205]. EVs derived from *S. mansoni* eggs have also been reported to carry protective properties and might be of importance for vaccination development[206]. Vaccination with the egg-derived EVs resulted in reduced worm counts and, in turn, egg burden and granuloma formation in the liver and was accompanied by elevated IFN-γ and IgG titres. These data suggest that *S. mansoni* egg-derived EVs contain immunogenic properties that target the immune response and mediate protection from subsequent infection. The EV contents mediating the protective response are not yet known but might be of use for the development of new vaccination candidates in the future. Taken together these data highlight that the investigation of EVs released during schistosomiasis infection and their interplay with the immune response is necessary and harbours the potential to contribute to the development of new therapeutic strategies.

4 Future perspective

This study aimed to characterise EVs released by apoptotic thymocytes and elucidate their immunological effects. Therefore, the cargo content of EVs released by apoptotic versus live thymocytes, their delivery to Mϕs and their subsequent impact on Mϕ behaviour were investigated. Even though EVs from live or apoptotic thymocytes differ in the composition of surface and intravesicular proteins and induced differences in the Mϕ gene expression profile, their functional impact on Mϕs was limited. EVs from apoptotic thymocytes, but not live thymocytes, target the nitric oxide pathway by upregulation of iNOS. However, differences in the amount of nitric oxide produced in the different experimental conditions have not been detected so far. To further elucidate the potential of liveT- and aT-EVs to interfere with target cell signalling, miRNA sequencing and proteomics are planned to be performed. A deeper analysis of these data will allow a more precise prediction of possible target cells and effects. If a specific miRNA or protein with a function associated with the regulation of the immune response, is identified to be selectively contained in aT-EVs or liveT-EVs, its function should be further investigated via additional experimental approaches. Selective blocking of the miRNA or protein of interest can be achieved via the use of neutralising antibodies, followed by the analysis of the target cell signalling and function. This allows for comparing the effects of the blocked EV signalling to those of the untreated EVs.

In this study, cleaved caspase-3 has been shown to be significantly more abundant in aT-EVs compared to liveT-EVs. Therefore, its functionality should be evaluated by performing an *in vitro* cleaved caspase-activity assay. In this context, liveT-EVs and aT-EVs should be analysed for their potential to cleave a cleaved caspase-3 substrate in the presence or absence of a caspase-3 inhibitor. Once the enzymatic activity has been proven, functional consequences of cleaved caspase-3 delivery to target cells via aT-EV uptake should be further investigated.

The influence of the transfer of liveT- and aT-EVs on the pathogenesis of schistosomiasis at week 8 p.i. was found to be only minor in this study. Transfer of aT-EVs could significantly reduce liver damage as detected by reduced ALT levels, whereby transfer of liveT-EVs reduced the expression of iNOS in hepatic Mϕs compared to PBS control mice. Yet, the cargo and mechanisms by which liveT- and aT-EVs might influence liver pathology remain to be investigated. Furthermore, the disease pathology should be analysed in later phases of the infection to investigate the influence of EV transfer on the development of fibrosis. Additionally, differentiating between the effects of smaller EVs and apoptotic bodies might be crucial to produce reliable results as they might have distinct or even opposite effects as described in 3.2.3.

Analysis of the EVs released in the livers of *S. mansoni*-infected mice appears to be very distinct from EVs released in the livers of naïve mice. In line with the detection of high amounts of larger EVs suggested to be apoptotic bodies, their functional impact on Mϕs seems to be comparable to aT-EVs. Revealing the individual components of liver- as well as aT-EVs via transcriptome and proteome analysis and examining the signalling transduction they induce in target cells, is crucial for further elucidating not only their role in schistosomiasis pathogenesis but also their potential therapeutic effects. Depending on their specific cargo, EVs can alter the behaviour of target cells, which can critically impact disease outcomes. In the long term, elucidating the molecular mechanisms of intercellular communication between EVs and their target cells will advance the comprehension of the potential of EVs for the development of novel treatment and vaccination strategies.

References

1. Johnstone, R. M., Adam, M., Hammond, J. R., Orr, L. & Turbide, C. Vesicle formation during reticulocyte maturation. Association of plasma membrane activities with released vesicles (exosomes). *Journal of Biological Chemistry* **262**, 9412–9420 (1987).

2. Lötvall, J. *et al.* Minimal experimental requirements for definition of extracellular vesicles and their functions: A position statement from the International Society for Extracellular Vesicles. *Journal of Extracellular Vesicles*. **3** (2014).

3. Théry, C. *et al.* Minimal information for studies of extracellular vesicles 2018 (MISEV2018): a position statement of the International Society for Extracellular Vesicles and update of the MISEV2014 guidelines. *J Extracell Vesicles* **7**, (2018).

4. Welsh, J. A. *et al.* Minimal information for studies of extracellular vesicles (MISEV2023): From basic to advanced approaches. *J Extracell Vesicles* **13**, (2024).

5. van Niel, G., D'Angelo, G. & Raposo, G. Shedding light on the cell biology of extracellular vesicles. *Nat Rev Mol Cell Biol* **19**, 213–228 (2018).

6. Colombo, M., Raposo, G. & Théry, C. Biogenesis, secretion, and intercellular interactions of exosomes and other extracellular vesicles. *Annual review of cell and developmental biology*. **30**, 255–289 (2014).

7. Andreu, Z. & Yáñez-Mó, M. Tetraspanins in extracellular vesicle formation and function. *Front Immunol* **5**, 442 (2014).

8. Hurley, J. H. ESCRT Complexes and the Biogenesis of Multivesicular Bodies. *Current opinion in cell biology*, **20**(1), 4–11 (2008).

9. Stuffers, S., Sem Wegner, C., Stenmark, H. & Brech, A. Multivesicular endosome biogenesis in the absence of ESCRTs. *Traffic* **10**, 925–937 (2009).

10. Harding, C., Heuser, J. & Stahl, P. *Receptor-Mediated Endocytosis of Transferrin and of the Transferrin Receptor in Rat Reticulocytes Recycling*. *The journal of cell biology* **97**(2), 329–339 (1983).

11. Krylova, S. V. & Feng, D. The Machinery of Exosomes: Biogenesis, Release, and Uptake. *International Journal of Molecular Sciences* **24**(2), 1337 (2023).

12. Frey, B. & Gaipl, U. S. The immune functions of phosphatidylserine in membranes of dying cells and microvesicles. *Seminars in Immunopathology* **33**, 497–516 (2011).

13. Coleman, M. L. *et al.* Membrane blebbing during apoptosis results from caspase-mediated activation of ROCK I. *Nat Cell Biol* **3**, 339–345 (2001).

14. Phan, T. K. *et al.* Pannexin-1 channel regulates nuclear content packaging into apoptotic bodies and their size. *Proteomics* **21**, 13-14 (2021).

15. Dixson, A. C., Dawson, T. R., Di Vizio, D. & Weaver, A. M. Context-specific regulation of extracellular vesicle biogenesis and cargo selection. *Nature Reviews Molecular Cell Biology* vol. **24**, 454–476 (2023).

16. Raiborg, C. & Stenmark, H. The ESCRT machinery in endosomal sorting of ubiquitylated membrane proteins. *Nature* **458**, 445–452 (2009).

17. Lu, P. *et al.* MEX3C interacts with adaptor-related protein complex 2 and involves in miR-451a exosomal sorting. *PLoS One* **12**, (2017).

18. Lee, H. *et al.* Caveolin-1 selectively regulates microRNA sorting into microvesicles after noxious stimuli. *Journal of Experimental Medicine* **216**, 2202–2220 (2019).

19. Lin, F. *et al.* YBX-1 mediated sorting of miR-133 into hypoxia/reoxygenation-induced EPC-derived exosomes to increase fibroblast angiogenesis and MEndoT. *Stem Cell Res Ther* **10**, 263 (2019).

20. Wozniak, A. L. *et al.* The RNA binding protein FMR1 controls selective exosomal miRNA cargo loading during inflammation. *Journal of Cell Biology* **219**, (2020).

21. Villarroya-Beltri, C. *et al.* Sumoylated hnRNPA2B1 controls the sorting of miRNAs into exosomes through binding to specific motifs. *Nat Commun* **4**, (2013).

22. Wei, Z. *et al.* Coding and noncoding landscape of extracellular RNA released by human glioma stem cells. *Nat Commun* **8**, 1145 (2017).

23. Morelli, A. E. *et al.* Endocytosis, intracellular sorting, and processing of exosomes by dendritic cells. *Blood* **104**, 3257–3266 (2004).

24. Purushothaman, A. *et al.* Fibronectin on the surface of myeloma cell-derived exosomes mediates exosome-cell interactions. *Journal of Biological Chemistry* **291**, 1652–1663 (2016).

25. Mulcahy, L. A., Pink, R. C. & Carter, D. R. F. Routes and mechanisms of extracellular vesicle uptake. *Journal of Extracellular Vesicles* **3** (2014).

26. Raposo, G. & Stoorvogel, W. Extracellular vesicles: Exosomes, microvesicles, and friends. *Journal of Cell Biology* **200**, 373–383 (2013).

27. Feng, D. *et al.* Cellular internalization of exosomes occurs through phagocytosis. *Traffic* **11**, 675–687 (2010).

28. Mathieu, M., Martin-Jaular, L., Lavieu, G. & Théry, C. Specificities of secretion and uptake of exosomes and other extracellular vesicles for cell-to-cell communication. *Nature Cell Biology* **21**, 9–17 (2019).

29. Buzas, E. I. The roles of extracellular vesicles in the immune system. *Nature Reviews Immunology* **23**, 236–250 (2023).

30. Simeone, P. *et al.* Extracellular vesicles as signaling mediators and disease biomarkers across biological barriers. *International Journal of Molecular Sciences* **21**, 2514 (2020).

31. Urabe, F. *et al.* Extracellular vesicles as biomarkers and therapeutic targets for cancer. *Extracellular Vesicles in Cell Physiology Am J Physiol Cell Physiol* **318**, 29–39 (2020).

32. Wang, S., Gao, J. & Wang, Z. Outer membrane vesicles for vaccination and targeted drug delivery. *Wiley Interdisciplinary Reviews: Nanomedicine and Nanobiotechnology* **11**, (2019).

33. Kerr, J. F. R., Wyllie, A. H. & Currie, A. R. Apoptosis: a basic biological phenomenon with wide-ranging implications in tissue kinetics. *Br. J. Cancer* **26** (1972).

34. Nössing, C. & Ryan, K. M. 50 years on and still very much alive: 'Apoptosis: a basic biological phenomenon with wide-ranging implications in tissue kinetics'. *Br J Cancer* **128**, 426–431 (2023).

35. Norbury, C. J. & Hickson, I. D. Cellular responses to dna damage. *Curr Opin Cell Biol.* **10** (2) 240-7 (1998).

36. Creagh, E. M., Conroy, H. & Martin, S. J. Caspase-Activation Pathways in Apoptosis and Immunity. *Immunol Rev*. **193**, 10-21 (2003).

37. Jan, R. & Chaudhry, G. e. S. Understanding apoptosis and apoptotic pathways targeted cancer therapeutics. *Advanced Pharmaceutical Bulletin* **9**, 205–218 Preprint at (2019).

38. Igney, F. H. & Krammer, P. H. Death and anti-death: Tumour resistance to apoptosis. *Nature Reviews Cancer* **2**, 277–288 (2002).

39. Cohen, G. M. Caspases: The Executioners of Apoptosis. *Biochem. J* **326** (1997).

40. Enari, M. *et al.* A caspase-activated DNase that degrades DNA during apoptosis, and its inhibitor ICAD. *Nature* **391**, 43–50 (1998).

41. Häcker, G. The morphology of apoptosis. *Cell and Tissue Research* **301**, 5–17 (2000).

42. Santavanond, J. P., Rutter, S. F., Atkin-Smith, G. K. & Poon, I. K. H. Apoptotic Bodies: Mechanism of Formation, Isolation and Functional Relevance. *Subcell Biochem.* **97***,* 61–88 (2021).

43. Bratton, D. L. *et al.* Appearance of phosphatidylserine on apoptotic cells requires calcium-mediated nonspecific flip-flop and is enhanced by loss of the aminophospholipid translocase. *Journal of Biological Chemistry* **272**, 26159–26165 (1997).

44. Mandal, D., Mazumder, A., Das, P., Kundu, M. & Basu, J. Fas-, caspase 8-, and caspase 3-dependent signaling regulates the activity of the aminophospholipid translocase and phosphatidylserine externalization in human erythrocytes. *Journal of Biological Chemistry* **280**, 39460–39467 (2005).

45. Segawa, K. *et al.* Caspase-mediated cleavage of phospholipid flippase for apoptotic phosphatidylserine exposure. *Science (1979)* **344**, 1164–1168 (2014).

46. Tixeira, R. *et al.* ROCK1 but not LIMK1 or PAK2 is a key regulator of apoptotic membrane blebbing and cell disassembly. *Cell Death Differ* **27**, 102–116 (2020).

47. Orlando, K. A., Stone, N. L. & Pittman, R. N. Rho kinase regulates fragmentation and phagocytosis of apoptotic cells. *Exp Cell Res* **312**, 5–15 (2006).

48. Takahashi, A. *et al.* Exosomes maintain cellular homeostasis by excreting harmful DNA from cells. *Nat Commun* **8**, (2017).

49. Bilyy, R. O. *et al.* Macrophages discriminate glycosylation patterns of apoptotic cell-derived microparticles. *Journal of Biological Chemistry* **287**, 496–503 (2012).

50. Sui, B. *et al.* Apoptotic Extracellular Vesicles (ApoEVs) Safeguard Liver Homeostasis and Regeneration vis Assembling an ApoEV-Golgi Organelle. *bioRxiv* 02.24.432630 (2021).

51. Poon, I. K. H. *et al.* Moving beyond size and phosphatidylserine exposure: evidence for a diversity of apoptotic cell-derived extracellular vesicles in vitro. *J Extracell Vesicles* **8**, (2019).

52. Ye, Q. *et al.* MSCs-derived apoptotic extracellular vesicles promote muscle regeneration by inducing Pannexin 1 channel-dependent creatine release by myoblasts. *Int J Oral Sci* **15**, (2023).

53. Abid Hussein, M. N., Böing, A. N., Sturk, A., Hau, C. M. & Nieuwland, R. Inhibition of microparticle release triggers endothelial cell apoptosis and detachment. *Thromb Haemost* **98**, 1096–1107 (2007).

54. Hill, C., Dellar, E. R. & Baena-Lopez, L. A. Caspases help to spread the message via extracellular vesicles. *FEBS Journal* **290**, 1954–1972 (2023).

55. Cocca, B. A., Cline, A. M. & Radic, M. Z. Blebs and Apoptotic Bodies Are B Cell Autoantigens *The Journal of Immunology* **169,** 155-166(2002).

56. Schiller, M. *et al.* Autoantigens are translocated into small apoptotic bodies during early stages of apoptosis. *Cell Death Differ* **15**, 183–191 (2008).

57. Pontejo, S. M. & Murphy, P. M. Chemokines act as phosphatidylserine-bound 'find-me' signals in apoptotic cell clearance. *PLoS Biol* **19**, (2021).

58. Takeuchi, O. & Akira, S. Pattern Recognition Receptors and Inflammation. *Cell* **140**, 805–820 (2010).

59. Murphy, K. & Weaver, C. Janeway Immunologie. Springer Berlin Heidelberg, (2018).

60. Ryter, A. Relationship between ultrastructure and specific functions of macrophages. *Comp Immunol Microbiol Infect Dis* **8**, 119–133 (1985).

61. Langermans, J. A. M., Hazenbos, W. L. W. & van Furth, R. Antimicrobial functions of mononuclear phagocytes. *J Immunol Methods* **174**, 185–194 (1994).

62. Sallusto, F. & Lanzavecchia, A. Heterogeneity of CD4+ memory T cells: Functional modules for tailored immunity. *European Journal of Immunology* **39**, 2076–2082 (2009).

63. Hoeffel, G. *et al.* C-Myb+ Erythro-Myeloid Progenitor-Derived Fetal Monocytes Give Rise to Adult Tissue-Resident Macrophages. *Immunity* **42**, 665–678 (2015).

64. Sheng, J., Ruedl, C. & Karjalainen, K. Most Tissue-Resident Macrophages Except Microglia Are Derived from Fetal Hematopoietic Stem Cells. *Immunity* **43**, 382–393 (2015).

65. Okabe, Y. & Medzhitov, R. Tissue-Specific Signals Control Reversible Program of Localization and Functional Polarization of Macrophages. *Cell* **157**, 832–844 (2014).

66. Gomez Perdiguero, E. *et al.* Tissue-resident macrophages originate from yolk-sac-derived erythro-myeloid progenitors. *Nature* **518**, 547–551 (2015).

67. Bou Ghosn, E. E. *et al.* Two physically, functionally, and developmentally distinct peritoneal macrophage subsets. *Proc Natl Acad Sci U S A* **107**, 2568–2573 (2010).

68. Bilzer, M., Roggel, F. & Gerbes, A. L. Role of Kupffer cells in host defense and liver disease. *Liver International* **26**, 1175–1186 (2006).

69. Medina, C. B. *et al.* Metabolites released from apoptotic cells act as tissue messengers. *Nature* **580**, 130–135 (2020).

70. Chaintreuil, P. *et al.* The generation, activation, and polarization of monocyte-derived macrophages in human malignancies. *Frontiers in Immunology* **14**, (2023).

71. Guilliams, M. & Scott, C. L. Does niche competition determine the origin of tissue-resident macrophages? *Nat Rev Immunol* **17**, 451–460 (2017).

72. Murray, P. J. *et al.* Macrophage Activation and Polarization: Nomenclature and Experimental Guidelines. *Immunity* **41**, 14–20 (2014).

73. Liu, Z., Gu, Y., Shin, A., Zhang, S. & Ginhoux, F. Analysis of Myeloid Cells in Mouse Tissues with Flow Cytometry. *STAR Protoc* **1**, 100029 (2020).

74. Sakai, M. *et al.* Liver-Derived Signals Sequentially Reprogram Myeloid Enhancers to Initiate and Maintain Kupffer Cell Identity. *Immunity* **51**, 655-670.e8 (2019).

75. Lavin, Y. *et al.* Tissue-Resident Macrophage Enhancer Landscapes Are Shaped by the Local Microenvironment. *Cell* **159**, 1312–1326 (2014).

76. van de Laar, L. *et al.* Yolk Sac Macrophages, Fetal Liver, and Adult Monocytes Can Colonize an Empty Niche and Develop into Functional Tissue-Resident Macrophages. *Immunity* **44**, 755–768 (2016).

77. Mantovani, A. *et al.* The chemokine system in diverse forms of macrophage activation and polarization. *Trends in Immunology* **25**, 677–686 (2004).

78. Kawasaki, T. & Kawai, T. Toll-like receptor signaling pathways. *Frontiers in Immunology* **5** (2014).

79. Murphy, M. P. Nitric oxide and cell death. *Biochimica et Biophysica Acta (BBA) - Bioenergetics* **1411**, 401–414 (1999).

80. Xue, Q., Yan, Y., Zhang, R. & Xiong, H. Regulation of iNOS on immune cells and its role in diseases. *International Journal of Molecular Sciences* **19** (2018).

81. Lu, G. *et al.* Myeloid cell-derived inducible nitric oxide synthase suppresses M1 macrophage polarization. *Nat Commun* **6**, 6676 (2015).

82. Bosurgi, L. *et al.* Macrophage function in tissue repair and remodeling requires IL-4 or IL-13 with apoptotic cells. *Science (1979)* **356**, 1072–1076 (2017).

83. Hamley, M. *et al.* Nmes1 is a novel regulator of mucosal response influencing intestinal healing potential. *Eur J Immunol* **54**, (2024).

84. Gordon, S. & Martinez, F. O. Alternative activation of macrophages: Mechanism and functions. *Immunity* **32**, 593–604 (2010).

85. Novak, M. L. & Koh, T. J. Macrophage phenotypes during tissue repair. *J Leukoc Biol* **93**, 875–881 (2013).

86. Mantovani, A., Biswas, S. K., Galdiero, M. R., Sica, A. & Locati, M. Macrophage plasticity and polarization in tissue repair and remodelling. *Journal of Pathology* **229**, 176–185 (2013).

87. Mills, C. D., Kincaid, K., Alt, J. M., Heilman, M. J. & Hill, A. M. M-1/M-2 Macrophages and the Th1/Th2 Paradigm. *The Journal of Immunology* **164**, 6166–6173 (2000).

88. Modolell, M., Corraliza, I. M., Link, F., Soler, G. & Eichmann, K. Reciprocal regulation of the nitric oxide synthase/arginase balance in mouse bone marrow-derived macrophages by TH 1 and TH 2 cytokines. *Eur J Immunol* **25**, 1101–1104 (1995).

89. Okabe, Y. Molecular control of the identity of tissue-resident macrophages. *International Immunology* **30**, 485–491 (2018).

90. Elliott, M. R. *et al.* Nucleotides released by apoptotic cells act as a find-me signal to promote phagocytic clearance. *Nature* **461**, 282–286 (2009).

91. Grimsley, C. & Ravichandran, K. S. Cues for apoptotic cell engulfment: Eat-me, don't eat-me and come-get-me signals. *Trends in Cell Biology* **13**, 648–656 4 (2003).

92. Min, C. *et al.* Tim-4 functions as a scavenger receptor for phagocytosis of exogenous particles. *Cell Death Dis* **11**, 561 (2020).

93. Savill, J., Hogg, N., Ren, Y. & Haslett, C. Thrombospondin cooperates with CD36 and the vitronectin receptor in macrophage recognition of neutrophils undergoing apoptosis. *J Clin Invest* **90**, 1513–1522 (1992).

94. Rothlin, C. V., Carrera-Silva, E. A., Bosurgi, L. & Ghosh, S. TAM receptor signaling in immune homeostasis. *Annu Rev Immunol* **33**, 355–391 (2015).

95. Rothlin, C. V., Ghosh, S., Zuniga, E. I., Oldstone, M. B. A. & Lemke, G. TAM Receptors Are Pleiotropic Inhibitors of the Innate Immune Response. *Cell* **131**, 1124–1136 (2007).

96. Sen, P. *et al.* Apoptotic cells induce Mer tyrosine kinase–dependent blockade of NF-κB activation in dendritic cells. *Blood* **109**, 653–660 (2006).

97. Liebold, I. *et al.* Apoptotic cell identity induces distinct functional responses to IL-4 in efferocytic macrophages. *Science* **384**, 6691 (2024).

98. Miyanishi, M. *et al.* Identification of Tim4 as a phosphatidylserine receptor. *Nature* **450**, 435–439 (2007).

99. Gregory, C. D. & Rimmer, M. P. Extracellular vesicles arising from apoptosis: forms, functions, and applications. *Journal of Pathology* **260**, 592–608 (2023).

100. Tsai, W. H., Chang, S. C., Lin, Y. C. & Hsu, H. C. CX3CL1(+) microparticles-induced MFG-E8 enhances apoptotic cell clearance by alveolar macrophages. *Cells* **10**, (2021).

101. Patil, M. *et al.* Novel Mechanisms of Exosome-Mediated Phagocytosis of Dead Cells in Injured Heart. *Circ Res* **129**, 1006–1020 (2021).

102. Ayala-Cuellar, A. P., Kang, J. H., Jeung, E. B. & Choi, K. C. Roles of mesenchymal stem cells in tissue regeneration and immunomodulation. *Biomolecules and Therapeutics* **27**, 25–33 (2019).

103. Distler, J. H. W. *et al. The Release of Microparticles by Apoptotic Cells and Their Effects on Macrophages*. *Apoptosis* vol. 10 (2005).

104. Torr, E. E. *et al.* Apoptotic cell-derived ICAM-3 promotes both macrophage chemoattraction to and tethering of apoptotic cells. *Cell Death Differ* **19**, 671–679 (2012).

105. Niessen, A. *et al.* Apoptotic-cell-derived membrane microparticles and IFN-α induce an inflammatory immune response. *J Cell Sci* **128**, 2443–2453 (2015).

106. Chen, H. *et al.* Extracellular Vesicles from Apoptotic Cells Promote TGFβ Production in Macrophages and Suppress Experimental Colitis. *Sci Rep* **9**, (2019).

107. Zheng, C. *et al.* Apoptotic vesicles restore liver macrophage homeostasis to counteract type 2 diabetes. *J Extracell Vesicles* **10**, (2021).

108. Muhsin-Sharafaldine, M.-R. *et al.* Procoagulant and Immunogenic Properties of Melanoma Exosomes, Microvesicles and Apoptotic Vesicles. *Oncotarget* **7**, 56279–56294 (2016).

109. Fehr, E.-M. *et al.* Apoptotic-cell-derived membrane vesicles induce an alternative maturation of human dendritic cells which is disturbed in SLE. *J Autoimmun* **40**, 86–95 (2013).

110. Berda-Haddad, Y. *et al.* Sterile inflammation of endothelial cell-derived apoptotic bodies is mediated by interleukin-1α. *Proc Natl Acad Sci U S A* **108**, 20684–20689 (2011).

111. Schiller, M. *et al.* Induction of Type I IFN Is a Physiological Immune Reaction to Apoptotic Cell-Derived Membrane Microparticles. *The Journal of Immunology* **189**, 1747–1756 (2012).

112. Eken, C. *et al.* Ectosomes released by polymorphonuclear neutrophils induce a MerTK-dependent anti-inflammatory pathway in macrophages. *Journal of Biological Chemistry* **285**, 39914–39921 (2010).

113. Kamerkar, S. *et al.* Exosomes facilitate therapeutic targeting of oncogenic KRAS in pancreatic cancer. *Nature* **546**, 498–503 (2017).

114. WHO. Schistosomiasis - WHO report (2023). https://www.who.int/news-room/fact-sheets/detail/schistosomiasis (accessed 14.04.2024).

115. Vale, N. *et al.* Praziquantel for schistosomiasis: Single-drug metabolism revisited, mode of action, and resistance. *Antimicrobial Agents and Chemotherapy* **61** (2017).

116. Nelwan, M. L. Schistosomiasis: Life Cycle, Diagnosis, and Control. *Current Therapeutic Research - Clinical and Experimental* **91**, 5–9 (2019).

117. Cheever, A. W., Macedonia, J. G., Mosimann, J. E., Mosimann, ; J E & Allen, E. Kinetics Of Egg Production And Egg Excretion By Schistosoma Mansoni And S. Japonicum In Mice Infected With A Single Pair Of Worms. *American Journal Of Tropical Medicine And Hygiene* **50** (1994).

118. Schwartz, C. & Fallon, P. G. Schistosoma “Eggs-iting” the host: Granuloma formation and egg excretion. *Frontiers in Immunology* **9** (2018).

119. Ribeiro De Jesus, A. *et al.* Clinical and Immunologic Evaluation of 31 Patients with Acute *Schistosomiasis Mansoni*. *The Journal of infectious diseases*, **185**, 98–105 (2001).

120. Molehin, A. J. Current Understanding of Immunity Against Schistosomiasis: Impact on Vaccine and Drug Development. *Res Rep Trop Med* **11**, 119–128 (2020).

121. Knuhr, K. *et al. Schistosoma mansoni* egg-released IPSE/alpha-1 dampens inflammatory cytokine responses viabasophil interleukin (IL)-4 and IL-13. *Front Immunol* **9**, (2018).

122. Schramm, G. *et al.* Molecular characterization of an interleukin-4-inducing factor from *Schistosoma mansoni* eggs. *Journal of Biological Chemistry* **278**, 18384–18392 (2003).

123. Burke, M. L. *et al.* Immunopathogenesis of human schistosomiasis. *Parasite Immunology* **31**, 163–176 (2009).

124. Singh, K. P., Gerard, H. C., Hudson, A. P. & Boros, D. L. Dynamics of collagen, MMP and TIMP gene expression during the granulomatous, fibrotic process induced by *Schistosoma mansoni* eggs. *Ann Trop Med Parasitol* **98**, 581–593 (2004).

125. An, P. *et al.* Hepatocyte mitochondria-derived danger signals directly activate hepatic stellate cells and drive progression of liver fibrosis. *Nat Commun* **11**, (2020).

126. Estaquier, J. ., Marguerite, M., Sahuc, F., Bessis, N. & Ameisen, C. A. and J. C. Interleukin-10 – mediated T cell apoptosis during the T helpertype 2 cytokine response in murine Schistosoma man-soni parasite infection. *Eur Cytokine Netw* **8**, 153–160 (1997).

127. Liu, T. *et al. FIZZ1 Stimulation of Myofibroblast Differentiation*. *Am J Pathol* **164** (2004).

128. Hesse, M. *et al.* Differential Regulation of Nitric Oxide Synthase-2 and Arginase-1 by Type 1/Type 2 Cytokines In Vivo: Granulomatous Pathology Is Shaped by the Pattern of L-Arginine Metabolism. *The Journal of Immunology* **167** (2001).

129. Nascimento, M. *et al.* Ly6Chi Monocyte Recruitment Is Responsible for Th2 Associated Host-Protective Macrophage Accumulation in Liver Inflammation due to Schistosomiasis. *PLoS Pathog* **10**, (2014).

130. Girgis, N. M. *et al.* Ly6Chigh Monocytes Become Alternatively Activated Macrophages in Schistosome Granulomas with Help from CD4+ Cells. *PLoS Pathog* **10**, (2014).

131. Coakley, G., Wright, M. D. & Borger, J. G. *Schistosoma mansoni*-derived lipids in extracellular vesicles: Potential agonists for eosinophillic tissue repair. *Front Immunol* **10**, (2019).

132. Meningher, T. *et al.* Schistosomal extracellular vesicle-enclosed miRNAs modulate host T helper cell differentiation. *EMBO Rep* **21**, (2020).

133. Zhu, L., Liu, J. & Cheng, G. Role of microRNAs in schistosomes and schistosomiasis. *Frontiers in Cellular and Infection Microbiology* **4**, (2014).

134. Arora, N. *et al.* Micromanagement of immune system: Role of miRNAs in helminthic infections. *Frontiers in Microbiology* **8,** (2017).

135. Wang, L. *et al.* Exosome-like vesicles derived by *Schistosoma japonicum* adult worms mediates M1 type immune- activity of macrophage. *Parasitol Res* **114**, 1865–1873 (2015).

136. Liu, J. *et al.* Schistosoma japonicum extracellular vesicle miRNA cargo regulates host macrophage functions facilitating parasitism. *PLoS Pathog* **15**, (2019).

137. Wang, Y. *et al.* A Novel miRNA From Egg-Derived Exosomes of Schistosoma japonicum Promotes Liver Fibrosis in Murine Schistosomiasis. *Front Immunol* **13**, (2022).

138. Zhu, S. *et al.* Release of extracellular vesicles containing small RNAs from the eggs of Schistosoma japonicum. *Parasit Vectors* **9**, 1–9 (2016).

139. Wang, L. *et al.* Sja-miR-71a in Schistosome egg-derived extracellular vesicles suppresses liver fibrosis caused by schistosomiasis via targeting semaphorin 4D. *J Extracell Vesicles* **9**, (2020).

140. Qi, X. *et al.* Schistosome egg antigen stimulates the secretion of miR-33-carrying extracellular vesicles from macrophages to promote hepatic stellate cell activation and liver fibrosis in schistosomiasis. *PLoS Negl Trop Dis* **17**, (2023).

141. Wang, L. *et al.* Host liver-derived extracellular vesicles deliver miR-142a-3p induces neutrophil extracellular traps via targeting WASL to block the development of Schistosoma japonicum. *Molecular Therapy* **30**, 2092–2107 (2022).

142. Donoso-Quezada, J., Ayala-Mar, S. & González-Valdez, J. The role of lipids in exosome biology and intercellular communication: Function, analytics and applications. *Traffic* **22**, 204–220 (2021).

143. Watanabe, S., Alexander, M., Misharin, A. V. & Budinger, G. R. S. The role of macrophages in the resolution of inflammation. *Journal of Clinical Investigation* **129** 2619–2628 (2019).

144. Böing, A. N. *et al.* Active caspase-3 is removed from cells by release of caspase-3-enriched vesicles. *Biochimica et Biophysica Acta (BBA) - Molecular Cell Research* **1833**, 1844–1852 (2013).

145. Wang, G. *et al.* Astrocytes secrete exosomes enriched with proapoptotic ceramide and Prostate Apoptosis Response 4 (PAR-4): Potential mechanism of apoptosis induction in Alzheimer Disease (AD). *Journal of Biological Chemistry* **287**, 21384–21395 (2012).

146. Ittner, L. M. & Götz, J. Amyloid-β and tau — a toxic pas de deux in Alzheimer's disease. *Nat Rev Neurosci* **12**, 67–72 (2011).

147. Weghorst, F. *et al.* Caspase-3 Cleaves Extracellular Vesicle Proteins During Auditory Brainstem Development. *Front Cell Neurosci* **14**, (2020).

148. Skogberg, G., Telemo, E. & Ekwall, O. Exosomes in the thymus: Antigen transfer and vesicles. *Frontiers in Immunology* **6** (2015).

149. Wang, G.-J. *et al.* Thymus Exosomes-Like Particles Induce Regulatory T Cells. *The Journal of Immunology* **181**, 5242–5248 (2008).

150. Zitvogel, L. *et al.* Eradication of established murine tumors using a novel cell-free vaccine: dendritic cell derived exosomes. *Nat Med* **4**, 594–600 (1998).

151. Bensinger, S. J., Bandeira, A., Jordan, M. S., Caton, A. J. & Laufer, T. M. Major Histocompatibility Complex Class II–Positive Cortical Epithelium Mediates the Selection of Cd4+25+ Immunoregulatory T Cells. *Journal of Experimental Medicine* **194**, 427–438 (2001).

152. Bain, C. C. & Jenkins, S. J. The biology of serous cavity macrophages. *Cellular Immunology*. **330**, 126–135 (2018).

153. Sun, Y. *et al.* Colorectal cancer-derived extracellular vesicles containing HSP70 enhance macrophage phagocytosis by up-regulating MARCO expression. *Exp Cell Res* **426**, 113565 (2023).

154. Nishi, C., Yanagihashi, Y., Segawa, K. & Nagata, S. MERTK tyrosine kinase receptor together with TIM4 phosphatidylserine receptor mediates distinct signal transduction pathways for efferocytosis and cell proliferation. *Journal of Biological Chemistry* **294**, 7221–7230 (2019).

155. Liao, W. *et al.* Exosomes: The next generation of endogenous nanomaterials for advanced drug delivery and therapy. *Acta Biomater* **86**, 1–14 (2019).

156. Barile, L. & Vassalli, G. Exosomes: Therapy delivery tools and biomarkers of diseases. *Pharmacol Ther* **174**, 63–78 (2017).

157. Zhang, X. *et al.* Engineered Extracellular Vesicles for Cancer Therapy. *Advanced Materials* **33** (2021).

158. Han, Y. *et al.* Overview and update on methods for cargo loading into extracellular vesicles. *Processes* **9**, 1–19 (2021).

159. Gordon, S. Phagocytosis: An Immunobiologic Process. *Immunity* **44**, 463–475 (2016).

160. Wiklander, O. P. B., Brennan, M. Á., Lötvall, J., Breakefield, X. O. & EL Andaloussi, S. Advances in therapeutic applications of extracellular vesicles. *Sci Transl Med* **11**, (2019).

161. Murphy, M. P. *et al.* Guidelines for measuring reactive oxygen species and oxidative damage in cells and in vivo. *Nat Metab* **4**, 651–662 (2022).

162. Ge, X. *et al.* Myocardial ischemia-reperfusion induced cardiac extracellular vesicles harbour proinflammatory features and aggravate heart injury. *J Extracell Vesicles* **10**, (2021).

163. Wang, C. *et al.* Macrophage-Derived mir-155-Containing Exosomes Suppress Fibroblast Proliferation and Promote Fibroblast Inflammation during Cardiac Injury. *Molecular Therapy* **25**, 192–204 (2017).

164. Wang, D. *et al.* MiRNA-155 regulates the Th17/Treg ratio by targeting SOCS1 in severe acute pancreatitis. *Front Physiol* **9**, (2018).

165. Zhou, D. *et al.* SOCS Molecules: The Growing Players in Macrophage Polarization and Function. *Oncotarget* **8**(36), 60710–60722 (2017).

166. Jung, M. *et al.* IL-10 improves cardiac remodeling after myocardial infarction by stimulating M2 macrophage polarization and fibroblast activation. *Basic Res Cardiol* **112**, (2017).

167. Ritsu, M. *et al.* Critical role of tumor necrosis factor-α in the early process of wound healing in skin. *Journal of Dermatology & Dermatologic Surgery* **21**, 14–19 (2017).

168. Wang, Y. *et al.* Umbilical cord mesenchymal stem cell-derived apoptotic extracellular vesicles ameliorate cutaneous wound healing in type 2 diabetic mice via macrophage pyroptosis inhibition. *Stem Cell Res Ther* **14**, (2023).

169. Wang, J. *et al.* Apoptotic Extracellular Vesicles Ameliorate Multiple Myeloma by Restoring Fas-Mediated Apoptosis. *ACS Nano* **15**, 14360–14372 (2021).

170. Zhang, X. *et al.* Functional diversity of apoptotic vesicle subpopulations from bone marrow mesenchymal stem cells in tissue regeneration. *J Extracell Vesicles* **13**, (2024).

171. Schroder, W. A., Major, L. & Suhrbier, A. *The Role of SerpinB2 in Immunity*. *Critical Reviews™ in Immunology* **31** (2011).

172. Schroder, W. A. *et al.* SerpinB2 inhibits migration and promotes a resolution phase signature in large peritoneal macrophages. *Sci Rep* **9**, (2019).

173. Schroder, W. A. *et al.* SerpinB2 deficiency modulates Th1/Th2 responses after schistosome infection. *Parasite Immunol* **32**, 764–768 (2010).

174. Suttles, J. & Stout, R. D. Macrophage CD40 signaling: A pivotal regulator of disease protection and pathogenesis. *Semin Immunol* **21**, 257–264 (2009).

175. Shen, J. *et al.* iNOS is essential to maintain a protective Th1/ Th2 response and the production of cytokines/chemokines against Schistosoma japonicum infection in rats. *PLoS Negl Trop Dis* **16**, (2022).

176. Hesse, M., Cheever, A. W., Jankovic, D. & Wynn, T. A. NOS-2 Mediates the Protective Anti-Inflammatory and Antifibrotic Effects of the Th1-Inducing Adjuvant, IL-12, in a Th2 Model of Granulomatous Disease. *The American journal of pathology*, **157**(3), 945–955 (2000).

177. Dewals, B. G. *et al.* IL-4Rα-independent expression of mannose receptor and Ym1 by macrophages depends on their IL-10 responsiveness. *PLoS Negl Trop Dis* **4**, (2010).

178. Harbord, M. *et al.* Ym1 is a neutrophil granule protein that crystallizes in p47phox-deficient mice. *Journal of Biological Chemistry* **277**, 5468–5475 (2002).

179. Praillet, C., Lortat-Jacob, H., H., B. F. & Grimaud, J. A. Distribution of hepatic glycosaminoglycans during acute schistosomiasis: modulation by IFN gamma treatment. *Cell Mol Biol* **42**, 169–177 (1996).

180. Thong, V. D. & Quynh, B. T. H. Correlation of serum transaminase levels with liver fibrosis assessed by transient elastography in vietnamese patients with nonalcoholic fatty liver disease. *Int J Gen Med* **14**, 1349–1355 (2021).

181. Su, T. Risk of liver fibrosis beyond a normal alanine aminotransferase level. *Advances in Digestive Medicine* **6**, 1–2 (2019).

182. Liu, X. Y. *et al.* Fibronectin expression is critical for liver fibrogenesis in vivo and in vitro. *Mol Med Rep* **14**, 3669–3675 (2016).

183. Fabre, V. *et al.* Tissue inhibitor of matrix-metalloprotease-1 predicts risk of hepatic fibrosis in human Schistosoma japonicum infection. *Journal of Infectious Diseases* **203**, 707–714 (2011).

184. Brigstock, D. R. Extracellular vesicles in organ fibrosis: Mechanisms, therapies, and diagnostics. *Cells* **10,** (2021).

185. Liu, X. *et al.* Hepatocyte-derived MASP1-enriched small extracellular vesicles activate HSCs to promote liver fibrosis. *Hepatology* **77**, (2023).

186. Qu, Y. *et al.* Exosomes derived from miR-181-5p-modified adipose-derived mesenchymal stem cells prevent liver fibrosis via autophagy activation. *J Cell Mol Med* **21**, 2491–2502 (2017).

187. Sui, B. *et al.* Apoptotic Extracellular Vesicles (ApoEVs) Safeguard Liver Homeostasis and 2 Regeneration via Assembling an ApoEV-Golgi Organelle. *bioRxiv* (2021).

188. Jiang, J. X., Mikami, K., Venugopal, S., Li, Y. & Török, N. J. Apoptotic body engulfment by hepatic stellate cells promotes their survival by the JAK/STAT and Akt/NF-κB-dependent pathways. *J Hepatol* **51**, 139–148 (2009).

189. Phan, T. K., Ozkocak, D. C. & Poon, I. K. H. Unleashing the therapeutic potential of apoptotic bodies. *Biochemical Society Transactions* **48**, 2079–2088 (2020).

190. Poon, I. K. H., Lucas, C. D., Rossi, A. G. & Ravichandran, K. S. Apoptotic cell clearance: basic biology and therapeutic potential. *Nat Rev Immunol* **14**, 166–180 (2014).

191. Henry, F. *et al. Antigen-Presenting Cells That Phagocytose Apoptotic Tumor-Derived Cells Are Potent Tumor Vaccines 1*. *CANCER RESEARCH* **59** (1999).

192. Bischofsberger, M., Winkelmann, F., Rabes, A., Reisinger, E. C. & Sombetzki, M. Pathogen-host interaction mediated by vesicle-based secretion in schistosomes. *Protoplasma* **257**, 1277–1287 (2020).

193. Lawrence, T. & Natoli, G. Transcriptional regulation of macrophage polarization: Enabling diversity with identity. *Nature Reviews Immunology* **11**, 750–761 (2011).

194. Shen, J. *et al.* Nitric oxide blocks the development of the human parasite Schistosoma japonicum. *Proc Natl Acad Sci U S A* **114**, 10214–10219 (2017).

195. Lu, H. *et al.* Quercetin ameliorates kidney injury and fibrosis by modulating M1/M2 macrophage polarization. *Biochem Pharmacol* **154**, 203–212 (2018).

196. Kisseleva, T. & Brenner, D. Molecular and cellular mechanisms of liver fibrosis and its regression. *Nature Reviews Gastroenterology and Hepatology* **18,** 151–166 (2021).

197. Chuah, C. *et al.* Characterising granuloma regression and liver recovery in a murine model of schistosomiasis japonica. *Int J Parasitol* **46**, 239–252 (2016).

198. Andrade, Z. A. & Grimaudt, J.-A. Morphology Of Chronic Collagen Resorption A Study on the Late Stages Of Schistosomal Granuloma Involution. *American Joumal of Pathology* **132** (1988).

199. Wang, T., Hua, H., Zhang, J., Li, W. & Yang, K. Noninvasive diagnosis of liver fibrosis in schistosomiasis japonica: Opportunities and challenges. *Portal Hypertension & Cirrhosis* **2**, 43–45 (2023).

200. World Health Organization (WHO). Preventive Chemotherapy in Human Helminthiasis: Coordinated Use of Anthelminthic Drugs in Control Interventions: A Manual for Health Professionals and Programme Managers. *World Health Organization* (2006).

201. Kokaliaris, C. *et al.* Effect of preventive chemotherapy with praziquantel on schistosomiasis among school-aged children in sub-Saharan Africa: a spatiotemporal modelling study. *Lancet Infect Dis* **22**, 136–149 (2022).

202. Mangold, B. L. & Dean, D. A. The migration and survival of gamma-irradiated *Schistosoma mansoni* larvae and the duration of host-parasite contact in relation to the induction of resistance in mice. *Parasitology* **88 (2)**, 249–265 (1984).

203. Bergquist, R. *et al.* Triggering of high-level resistance against *Schistosoma mansoni* reinfection by artemether in the mouse model. *Am J Trop Med Hyg* **71**, 774–777 (2004).

204. Santini-Oliveira, M. *et al.* Development of the Sm14/GLA-SE Schistosomiasis Vaccine Candidate: An Open, Non-Placebo-Controlled, Standardized-Dose Immunization Phase Ib Clinical Trial Targeting Healthy Young Women. *Vaccines (Basel)* **10**, (2022).

205. Molehin, A. J., McManus, D. P. & You, H. Vaccines for Human Schistosomiasis: Recent Progress, New Developments and Future Prospects. *International Journal of Molecular Sciences* **23**, (2022).

206. Mossallam, S. F., Abou-El-naga, I. F., Bary, A. A., Elmorsy, E. A. & Diab, R. G. *Schistosoma mansoni* egg-derived extracellular vesicles: A promising vaccine candidate against murine schistosomiasis. *PLoS Negl Trop Dis* **15**, (2021).

Figures presenting schematic overviews were created with BioRender.com

List of Publications

Within the time course of this doctoral thesis, the author has contributed to the following publications:

Liebold I, Al Jawazneh A, Casar C, Lanzloth C, Leyk S, Hamley M, Wong MN, Kylies D, Gräfe SK, Edenhofer I, Aranda-Pardos I, Kriwet M, Haas H, Krause J, Hadjilaou A, Schromm AB, Richardt U, Eggert P, Tappe D, Weidemann SA, Ghosh S, Krebs CF, A-Gonzalez N, Worthmann A, Lohse AW, Huber S, Rothlin CV, Puelles VG, Jacobs T, Gagliani N, Bosurgi L. Apoptotic cell identity induces distinct functional responses to IL-4 in efferocytic macrophages. *Science*. **384,** 6691 (2024)

Hamley M*, Leyk S*, Casar C, Liebold I, Jawazneh AA, Lanzloth C, Böttcher M, Haas H, Richardt U, Rothlin CV, Jacobs T, Huber S, Adlung L, Pelczar P, Henao-Mejia J, Bosurgi L. Nmes1 is a novel regulator of mucosal response influencing intestinal healing potential. *Eur J Immunol*. **54**(2) (2024).

Wu Y, Leyk S, Torabi H, Höhn K, Honecker B, Tauler MDPM, Cadar D, Jacobs T, Bruchhaus I, Metwally NG. Plasmodium falciparum infection reshapes the human microRNA profiles of red blood cells and their extracellular vesicles. *iScience*. **26**(7), 107119 (2023).

Acknowledgements

Thank you, Lidia Bosurgi, for the opportunity to join your lab, your supervision and support during this project, for every fruitful discussion, and for not only sharing your precious expertise and experience with me but also your incredibly fascinating and never-ending drive and motivation to achieve scientific advances.

I thank Prof. Dr. Iris Bruchhaus and Prof. Dr. Julia Kehr for your effort and engagement in taking over the examination of this thesis.

Thanks to PD Dr. Thomas Jacobs not only for being my co-supervisor and sharing your laboratory with us but especially for the colleagues, the enjoyable working atmosphere, and the team cohesion that came alongside. Herin, a special thank goes to Ulricke Richardt for being the warm-hearted soul of the lab, bringing a good mood into the room every day, and keeping our cell cultures alive.

I want to thank our scientific collaborators from the UKE and BNITM for their flourishing cooperation. Especially highlighting Johannes Brandi for spreading his knowledge and passion for flow cytometry, Christoph Kilian for kindly analysing the sequencing data, Katharina Höhn for the transmission electron microscopy pictures and uplifting meetings, and Mohsin Shafiq for the instructions to the Nanosight. Thank you, Nahla Metwally, for supporting me in my scientific career since my master's thesis and for always having an open door to discuss the latest data and progress. Thanks to the EV community, especially Barbara Honecker and Pilar Martinez for being so collaborative and mastering technical, as well as mental challenges together. I also highly appreciated the teamwork with the animal facility at the BNITM, where everyone is sympathetically taking the best care of the experimental animals.

A special thanks to my wonderful colleagues Imke Liebold and Clarissa Lanzloth for your constant team effort, for being the best laboratory and moral support, for making every day and every experiment enjoyable and especially for your friendship. This working group, including our former lab members Madeleine Hamley and Amirah Al Jawazneh, has taught me how precious it is to be part of such a supportive working environment, where helping and promoting each other are always in the first place.

No scientific project is possible without financial funding. Therefore, I would like to thank the Landesforschungsförderung for providing financial support and a community to exchange ideas. Additionally, I want to thank Pro Exzellenzia Plus, not only for funding the last period of this project, but especially for their constant effort in encouraging women, both in their personal growth and professional careers.

I am especially grateful for all my colleagues who became such close friends. Imke, Clarissa, Cari, Jessi, Jana, and Lenny thank you for all the good memories and your emotional support in and outside the lab.

Zu guter Letzt bedanke ich mich bei meiner Familie und meinen Freunden. Besonders danke ich meinen Eltern, meinem Bruder und meinen Großeltern für euren Rückhalt, eure Unterstützung, ohne die ich nie so weit gekommen wäre. Danke an meine engsten und längsten Freunde, Anna und Lisi, dass ihr mich in jeder Lebenslage begleitet und unterstützt. Von Herzen Danke an Finn, dass du jeden einzelnen Tag die Höhen und Tiefen dieser Doktorarbeit mit mir durchlebt hast und mich jegliche Herausforderungen des Tages vergessen lässt, sobald ich nach Hause komme.